IPICYT

INSTITUTO POTOSINO DE INVESTIGACIÓN CIENTÍFICA Y TECNOLÓGICA, A.C.

ADVANCED MATERIALS DEPARTMENT

"Synthesis and evaluation of graphene-supported catalysts for its potential use in aquaprocessing of heavy crude oil"

Thesis by

Valeria Alvarado González

To obtain the Degree of

Doctor of Philosophy

Graduate Program in Nanosciences and Materials

Supervisor:

Dr. Vladimir Alonso Escobar Barrios

San Luis Potosí, S.L.P., September 2023

Constancia de aprobación de la tesis

La tesis **"Synthesis and evaluation of graphene-supported catalysts for its potential use in aquaprocessing of heavy crude oil"** presentada para obtener el Grado de Doctor(a) en Nanociencias y Materiales fue elaborada por **Valeria Alvarado González** y aprobada el **día 04 de septiembre de 2023** por los suscritos, designados por el Colegio de Profesores de la División de Materiales Avanzados del Instituto Potosino de Investigación Científica y Tecnológica, A.C.

_____
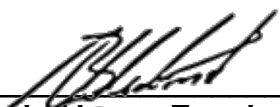
Dr. Vladimir Alonso Escobar Barrios
Director de la tesis

_____

Dra. Mariana Gutiérrez Sánchez
Miembro del Comité Tutoral

_____
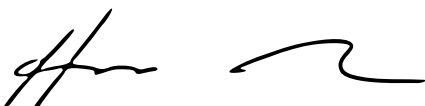
Dr. Horacio Flores Zúñiga
Miembro del Comité Tutoral

_____

Dr. Vicente Rodríguez González
Miembro del Comité Tutoral

Créditos institucionales

Esta tesis fue elaborada en los Laboratorios de Hidrocarburos y Polímeros de la División de Materiales Avanzados del Instituto Potosino de Investigación Científica y Tecnológica, A.C., bajo la dirección del Dr. Vladimir Alonso Escobar Barrios.

Institutional acknowledgment

Página en Blanco que se va a utilizar para colocar la copia del acta de examen.

DEDICATION

This dissertation is specially dedicated to Dania. Thank you for being beside me during this trip, you are my inspiration source. Never forget nothing can stop us.

"So, what is the solution? Do as the duckling does. Go ahead, struggle through it. Pick up the pen already and put it to the page and stop whining. Write. Pick up the brush and be mean to yourself for a change, paint. Dancers, put on the loose chemise, tie the ribbons in your hair, at your waist, or on your ankles and tell the body to take it from there. Dance. Actress, playwright, poet, musician, or any other. Generally, just stop talking. Don't say one more word unless you're a singer. Shut yourself in a room with a ceiling or in a clearing under the sky. Do your art. Generally, a thing cannot freeze if it is moving. So move. Keep moving."

Women Who Run With the Wolves
Clarissa Pinkola Estés

ACKNOWLEDGEMENTS

.

TABLE OF CONTENTS

LIST OF TABLES

LIST OF FIGURES

ABSTRACT

"Synthesis and evaluation of graphene-supported catalysts for its potential use in aquaprocessing of heavy crude oil"

The development of stable, effective, recoverable, and affordable catalysts has been promoted and studied in the petroleum industry for different processes. For instance, the catalytic aquaprocessing (AQP) process, is intended to upgrade oil by reducing permanently its viscosity and improving its API gravity. This process considers an important intermediate step, the water shift reaction (WGSR), to generate hydrogen *in situ* that allows its further reaction with complex molecules.

In this thesis, as a first step, a graphene-supported catalyst based on ceria was synthesized and characterized. The obtained CeO_2/graphene Materials showed good dispersion and interactions between the phases, favoring the ceria reduction.

Then, NiO-CeO_2-graphene composite materials were obtained with different concentrations of metal oxides using the polyol synthesis method in a single step. Here, the surface area of the materials increased. Furthermore, due to the hydrogen spillover phenomenon, ceria reduction is favored at lower temperatures due to interactions between the nickel nanoparticles and the graphene support. The catalysts exhibited catalytic activity in the range of 300-400 °C, the CO conversion increases by 20 % with adding 1 % of Ni, and lower selectivity towards methane was observed, which is attributed to the formation of an interface with a higher electronic density that increases the adsorption strength of CO.

KEYWORDS: Graphene-supported catalyst, hydrogen production, water gas shift, ceria-based catalyst, oil upgrading.

RESUMEN

"Síntesis y evaluación de catalizadores soportados en grafeno para su uso potencial en el acuaprocesamiento de aceites pesados"

Se ha promovido el desarrollo de catalizadores estables, efectivos, recuperables y asequibles, que a través de procesos catalíticos como el acuaprocesamiento (AQP), actualizan permanentemente el aceite, reduciendo su viscosidad y mejorando su gravedad API. Este proceso contempla un paso intermedio para generar hidrógeno in situ altamente activo a través de la reacción de desplazamiento de agua-gas (WGSR).

En esta tesis, como primer paso, se sintetizó y caracterizó un catalizador soportado en grafeno basado en ceria. Los materiales obtenidos de CeO_2/grafeno muestran buena dispersión e interacciones entre las fases, favoreciendo la reducción de la ceria.

Posteriormente, se obtuvieron materiales de NiO-CeO_2-grafeno, con diferentes concentraciones de los óxidos metálicos. Además, con la deposición de nanopartículas se incrementó el área superficial de los materiales. Además, la reducción de la ceria se favorece a temperaturas más bajas, debido a interacciones entre las nanopartículas de níquel y el soporte de grafeno, debido al fenómeno de *Spillover* de hidrogeno. Los catalizadores presentaron actividad catalítica en el intervalo de 300-400 °C, la conversión de CO aumentó 20 % con la adición de 1 % de Ni, y se observó menor selectividad hacia CH_4, atribuido a la formación de una interfase con mayor densidad electrónica lo que aumentó la fuerza de adsorción del CO.

PALABRAS CLAVE: ceria, grafeno, producción de hidrógeno, water gas shift, mejoramiento de aceites.

GRAPHICAL ABSTRACT
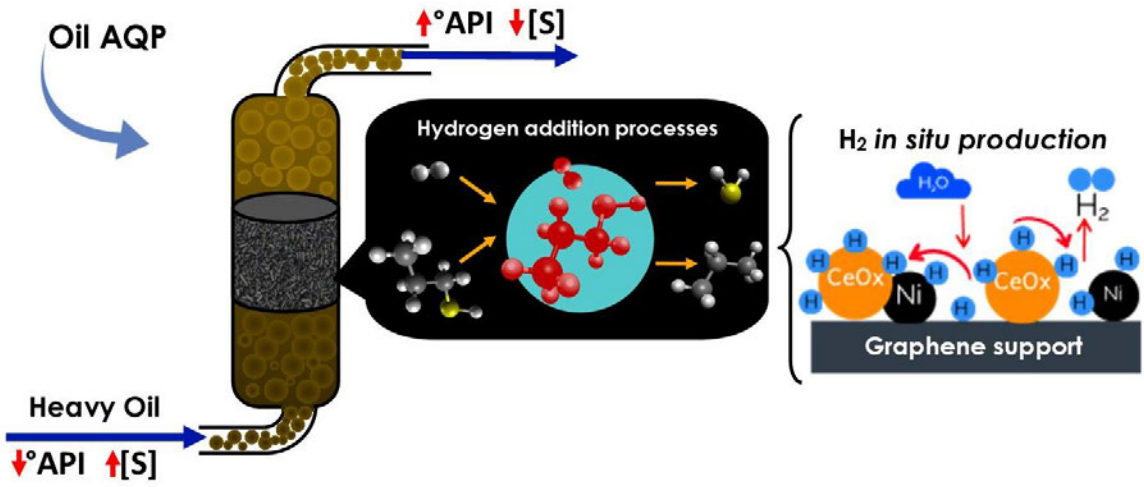
1. INTRODUCTION

Currently, in Mexico, the most abundant hydrocarbons are the heavy oils, which have a high viscosity (100000-1000000 cP [1]), high sulfur content (around 5.0% [1]), metals and asphaltenes, thus complicating their extraction, transportation, and refining operations.

One of the oldest and most preferred methods for reducing the viscosity of heavy oils is their dilution. It consists of adding lighter liquid hydrocarbons (typically the condensed products of natural gas production) to such heavy oils. Thus, it is possible to reduce the viscosity and facilitate the mobility in the ducts, adding 20-30% of the solvent, to avoid high-pressure drops or the need for high temperatures. However, it may require a greater investment in pumping infrastructure and pipelines due to the increased transport volume [2].

In addition, there is uncertainty regarding the availability of light oils, as the oils available in refineries today become heavier than those available 50 years ago, demanding an increased quantity of such light oils. This tendency to have heavier oil also causes the processes in extraction and refining operations to become more and more expensive [1].

Under this context, oil upgrading processes have been developed as a previous step for refinement, seeking to increase oil quality by generating a product with lower viscosity and higher API density with a greater added value in the market.

For instance, aquaconversion, aquathermolysis, and aquaprocessing (AQP) processes are visbreaking (viscosity reduction) technologies that use hydrogen transfer from water by a catalyst. These processes do not produce solid by-products such as coke and do not require an external source of hydrogen since steam is the hydrogen donor that carries out the reactions of hydrogenation, hydrodesulfurization (HDS), hydrodenitrogenation (HDN), and hydrodemetalization (HDM) [3].

The use of a catalyst in AQP promotes the breakdown of larger molecules and other synergistic reactions such as hydrogenation (which increases the H/C ratio) and ring-opening, giving a permanent viscosity reduction of the oils, benefiting exploitation, transport, and oil reforming [4,5].

The oil upgrading, by adding hydrogen, has been reported in the literature using a wide variety of catalysts, such as the case of nano-nickel in microemulsion reported by Li et al. [6], reaching a viscosity reduction of more than 98% in the aquathermolysis of extra-heavy oils at 280°C and 6.4 MPa for 24 hours. Dejhosseini et al. [7] investigated the catalytic cracking of bitumen with cerium oxide nanoparticles in supercritical water (374°C and 22.1 MPa), obtaining a 15.5% reduction of asphaltenes content.

In a previous work [8], the effect of graphene in improving the catalytic properties of ceria was demonstrated since this support can decrease the reduction temperatures of ceria and increase its catalytic activity in the WGSR through a spillover transport mechanism. Likewise, it was proposed that the presence of oxygen vacancies in the ceria interacted with π bonds in graphene, which makes up an electronic cloud, in

2

addition to the fact that the electrons located on the surface of the ceria (generated by vacancies of oxygen), could also interact with functional groups in graphene oxide (GO) [9].

Among the challenges that arose from the previous work, to improve the catalytic properties of the CeO_2/graphene material was obtaining a material with a high surface area and homogeneous dispersion of particles. Another suggestion was to increase the reducibility of ceria, which could be obtained by adding metallic nanoparticles deposited on the surface.

Due to the above, this thesis work aims to get a deeper understanding and optimize the previously studied material [8], by the addition of metallic oxide nanoparticles (CeO_2 and NiO) in different proportions, and to compare the effect of the type of carbon-based support (graphene and graphene oxide).

One of the main objectives of this work is to propose interactions between supports and metal oxides and to correlate these interactions and structural properties (crystallinity, porosity, surface area) that can influence the catalytic activity. In addition, it was proposed to use different characterization techniques to obtain the structural information of the materials and evaluate their potential use in AQP via WGSR, which would allow correlating the structure with its catalytic performance.

1.1. Motivation and problems to be solved

There is a worldwide trend towards the development of technologies that allow maximizing the recovery and increasing the quality of oil through catalytic processes, therefore there is interest in the development of stable, effective, and affordable catalysts, focused on relatively simple preparation methods.

The graph shown in **Figure 1** presents the number of scholarly articles over time by country, for the search "catalyst, oil Upgrading". A notable fact is that in the last decade, there has been a significant increase in these publications, which indicates the growing interest in the research and development of new catalyst materials for heavy oil Upgrading in several countries.

These catalysts can be unsupported or typically supported on metal oxides such as silica, alumina, or zeolites. However, there has been more research on carbon materials and their use as catalyst supports in recent years. The last is due to the carbonaceous material characteristics that provide greater structural, and chemical stability, which are appropriate for the reaction conditions. Furthermore, they are stable at high temperatures (above 1023 K under an inert atmosphere). Finally, the cost/benefit ratio of carbon supports is usually lower than that of conventional supports.
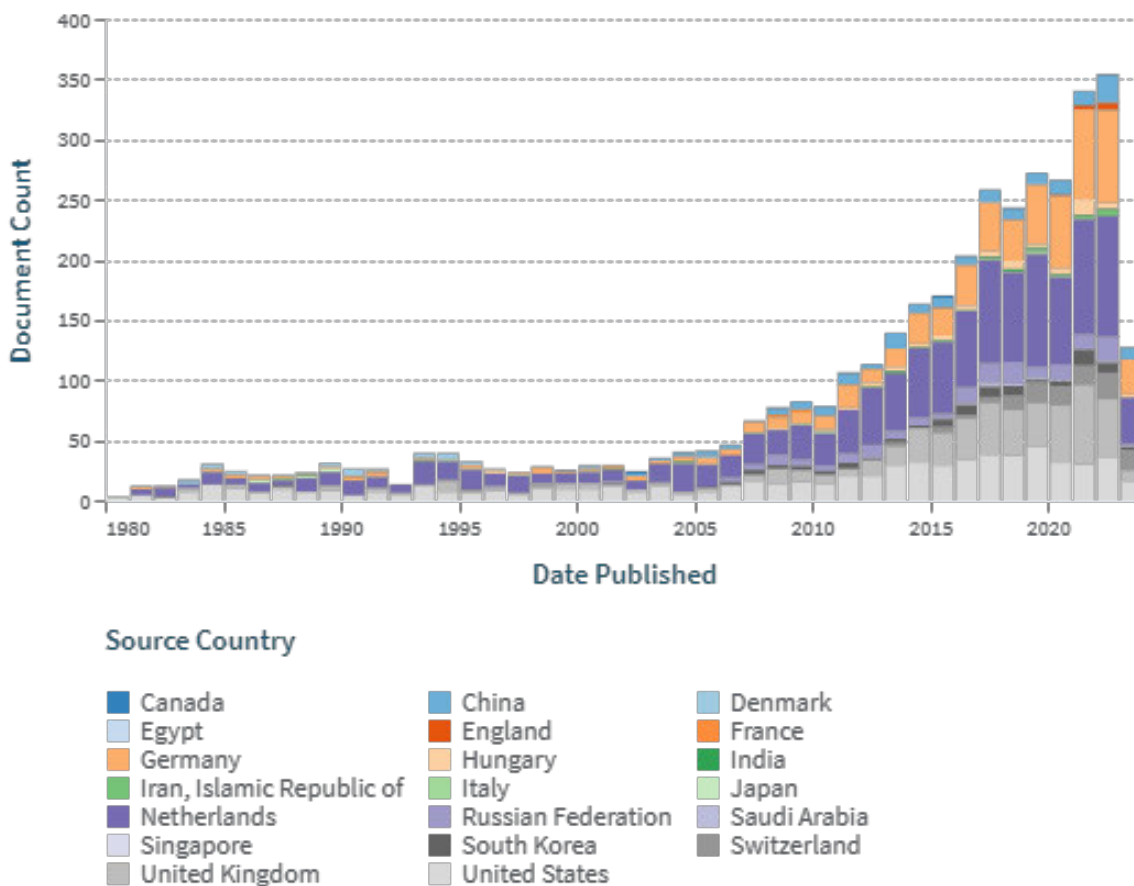
Figure 1. Number of scientific publications by year. Query: catalysts & Oil upgrading. Lens.org, June 2023.

Nevertheless, there are still some fundamental aspects that need to be studied to get a deeper understanding of them, for the right design of catalyst. This is very important, in general, for the oil producers and, in particular, for our country whose oil reserves are still significative although more than 50 % of them correspond to heavy and extra heavy oils. Then, in this thesis, the study of alternative catalyst with novel carbonaceous supports to generate hydrogen with high selectivity is a key for the aquaprocessing of heavy and extra-heavy oils.

1.2. Hypothesis

The electronic properties of graphene modify the mobility of ions, accelerating them, promoting the reduction of CeO_2 and, therefore, its catalytic activity.

The electronic structure of graphene is such that it would adsorb hydrogen atoms, which would be interacting with metal oxides (spillover), promoting their reduction/activation.

The strong interaction between Ni-CeO_2-graphene is given by the dispersion and anchoring of the nanoparticles, mobility of charges between the phases, and redox activity; and lately it is such that it increases its catalytic activity for reactions such as dissociation of water vapor to produce hydrogen.

1.3. General objective

Study the synthesis, properties, and catalytic performance of Ni/CeO_2-graphene materials for the water-gas shift reaction (WGS) as an intermediate step for the Upgrading (permanent reduction of viscosity and increase of API gravity) of heavy oils.

1.4. Specific objectives

1. Synthesize and deposit Ni nanoparticles (Ni NPs) and CeO_2 in graphene or graphene oxide supports, during the same process, with different concentrations of Ni and ceria, to compare the dispersion and anchoring of the Ni nanoparticles.

2. Structural-crystalline, elemental, thermal, and reactive characterization of the selected materials.

3. Design, build, and commission a fixed bed reaction system to evaluate the ability of materials to produce hydrogen from water vapor by the water gas shift reaction (WGSR). This step is considered a sweep for the selection of materials to be evaluated.

4. Correlate the structural, chemical, and textural properties of materials with their ability to produce hydrogen from water.

1.5. Structure of the thesis

The thesis has been structured beginning from establishing the reference frame (context) by a literature review to give the essential concepts for the developed work regarding the oil upgrading, importance and methodologies, the catalyst used for such porpoise, and the spillover phenomena (**Chapter 2**).

In **Chapter 3**, the characterization of the graphene-based support was carried out in terms of their structural, chemical, morphological, and thermal properties, which will allow us to understand the potential interaction between such supports and the metal oxides deposited on them. This is considered an important step to correlate the structure-properties-performance of the developed catalyst.

Then, **Chapter 4** describes the obtained results when ceria was deposited on the graphene-based supports. Thus, an interaction mechanism between ceria and graphene support was proposed. It is important to mention that this chapter gave the

data for the paper "Thermal-structural characterization and H_2 generation capability of novel CeO_2/graphene catalyst" by Gonzalez-Alvarado et al. published in *Journal of Environmental Chemical Engineering*, Vol. 10, 3 (2022) 107680, doi: 10.1016/j.jece.2022.107680. (See **Annex I**).

Once the ceria-based catalyst was characterized and evaluated in terms of its catalytic performance, the next step was to study its doping with nickel entity. The results about the synthesis, characterization and obtained results are presented and discussed in **Chapter 5**.

Chapter 6 deals with the synthesis and characterization of Ni/CeO_2/graphene composites that were carried out and discussed to get a deeper understanding of the interaction between nickel, ceria, and graphene.

Then, the catalytic performance of the Ni/CeO_2/graphene in terms of their reducibility, hydrogen production, and selectivity towards hydrogen, methane, CO_2, and CO was established and discussed in **Chapter 7**.

General conclusions and perspectives are presented in **Chapter 8.**

It is important to mention that it is important to give a brief section on materials and methods for each chapter since not all the same analytical techniques or experimental conditions were used in every step of the work.

2. LITERATURE REVIEW

2.1. Crude oil classification and catalytic upgrading

As mentioned, heavy oil is different from conventional oil. Heavy oils are characterized by a high specific weight, high viscosity (100000-1000000 cP), low API gravity (<20 °API), and low H/C ratio, as well as high asphaltenes, resins, heavy metals, sulfur, and nitrogen [1,11] content. Due to its high viscosity, it is very difficult to extract it from the reservoir's surface, transportation through pipelines becomes more expensive, and refining operations are complicated.

Because of this, heavy oil requires additional processing to convert it into a suitable feed for a refinery [12] or to transport it through a pipeline without adding solvent [13]. This is the heavy oil Upgrading.

Technologies for heavy oil upgrading can be divided into carbon rejection and hydrogen addition processes. Rejection of carbon redistributes hydrogen among the various components, resulting in fractions with increased hydrogen/carbon (H/C) atomic ratios and fractions with decreased H/C atomic ratios. On the other hand, hydrogen addition processes involve the reaction of heavy crudes with an external source of hydrogen and result in an overall increase in the H/C ratio [12].

Generally, hydrogen addition processes exhibit higher performance towards products of higher commercial value than carbon rejection processes, although the

former requires a greater investment and availability of natural gas to produce hydrogen and steam necessary for these processes [12].

2.1.1. Hydrogen addition processes

Adding hydrogen (hydroprocessing) improves the quality of heavy oil and bitumen since it increases the H/C ratio and eliminates high concentrations of heteroatoms and metals.

In the literature it has been mentioned that a series of reactions occur in hydroprocessing, which can be grouped as follows [14]:

- **Hydrocracking**. In these reactions, the larger molecules are cracked (they break into smaller molecules), and the free radicals formed are capped by hydrogen, which prevents the polymerization reaction that forms coke.

- **Hydrotreatment**. In these reactions, heteroatoms and metals are removed. Therefore, Hydrodesulfurization (HDS), Hydrodenitrogenation (HDN), Hydrodeoxygenation (HDO), and Hydrodemetallization (HDM) reactions are included.

- **Hydrogenation**. They involve the saturation of aromatics simultaneously with Hydrotreatment.

2.1.1.1 Hydrotreatment and Hydrogen Donors

The concentration and partial pressure of hydrogen in the hydroprocessing of heavy oil are very important. By increasing the amount of hydrogen, the quality of the final product increases, the temperature of the reactor necessary for the same reaction

decreases, and the speed of catalyst deactivation decreases. Therefore, for economic reasons, it is essential that hydrogen is recycled as much as possible and that the highest partial pressure of hydrogen is maintained. Furthermore, the recycled hydrogen inside the reactor must be kept as pure as possible [14].

2.1.1.2 Hydroprocessing Catalysts

Generally, commercial catalysts for hydroprocessing are made from support containing crystalline acid zeolites and amorphous silica-alumina compounds that also provide acid groups. That support is impregnated with active metals, such as palladium, molybdenum, nickel, or tungsten that carry out the hydrogenation. It should be noted that basic nitrogen in the feed (pyridine or ammonia) as a product reduces the acidity of the catalyst and deactivates it over time [14].

2.1.2. Catalytic Steam Cracking (CSC)

One of the most effective methods for upgrading heavy oil is catalytic reforming with steam, where the hydrogen atoms from water are used as a hydrogen source [15].

When the oil Upgrading occurs at 350–550 °C, in the presence of superheated steam, it is generally called "Steam Cracking" [16]. Steam Cracking can be carried out with or without catalysts, although using these allows to increase the efficiency and quality of the oil, with the suppression of coke formation in the products. Steam cracking is carried out in different modes (steady state, semi-flow, and flow) with fixed and slurry beds [16].

Eletskii et al. [17] point out among the advantages of this process that an additional hydrogen source is not necessary, due to its formation during the interaction

between water and the raw material (oil), it is also an economically more efficient process of reduction of the viscosity before the refining of crude oil.

2.1.3. Catalytic Aquaprocessing (AQP)

The Aquaprocessing was patented by Pereira et al. [18]. It is defined as a CSC process in the presence of an ultra-disperse (UD) catalyst, which is a water-in-oil emulsion containing an alkali metal and a Group VIII non-noble metal.

According to Fathi and Pereira [4], this process involves a reaction mechanism in which it is believed that the alkali metal promotes the dissociation of water into hydrogen and oxygen radicals. The presence of highly reactive free radicals enhances hydrocarbon cracking reactions. The non-noble transition metal promotes the dissociation of water and minimizes condensation reactions by promoting the enhancement of hydrogen to hydrocarbon free radicals. The authors present the following reactions as only a small part of the complex reaction system that occurs simultaneously during Aquaprocessing:

$$2H_2O \rightarrow 2H^\bullet + 2OH^\bullet \tag{1}$$
$$R\text{-}CH_2\text{-}R_n \rightarrow R^\bullet + {}^\bullet CH_2\text{-}R_n \tag{2}$$
$$R^\bullet + H^\bullet \rightarrow RH \tag{3}$$
$$2OH^\bullet + {}^\bullet CH_2\text{-}R_n \rightarrow CO_2 + 2H_2 + R_nH \tag{4}$$
$$R\text{-}CH_2\text{-}R_n + 2H_2O \rightarrow RH + CO_2 + R_nH + 2H_2 \tag{5}$$
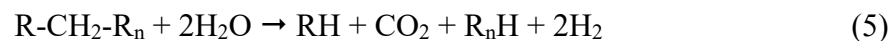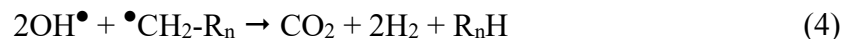
Equations 1-4 are considered general reaction steps of the breeding mechanism. Equation 1 presents the catalytic dissociation of water into hydrogen and hydroxyl

radicals. Simultaneously, the division of molecular bonds between heavy oil molecules and alkyl radicals occurs because of thermal energy, which produces hydrocarbon free radicals, as represented in equation 2. The UD catalyst promotes the addition of hydrogen and oxygen radicals to olefins and free radicals, which are typical products of thermal cracking. This results in hydrocarbons with lower molecular weights in addition to the production of CO_2, as represented in equations 3 and 4. The overall reaction is given by equation 5 [4].

Later, in 2015, in the work of García-Hubner [5] supported catalysts were developed to be used in Steam Catalytic Cracking in fixed-bed reactors. According to this author, the advantage of using a catalytic bed is that it allows its relatively easy replacement and even in situ catalyst regeneration.

2.1.3.1. *Water Gas Shift Reaction (WGSR)*

Numerous authors [5,15,16,19,20] agree that the hydrogen required in Upgrading processes of heavy oils with water, such as Catalytic Steam Cracking, Aquaprocessing, or Aquathermolysis; is produced by the Water Gas Shift (WGS) reaction.

In 1972, Phillips Petroleum Co [21], patented a method and catalyst for the upgrading of hydrocarbons, which contemplates a multi-component catalyst system to generate hydrogen in situ in the presence of water, through the reaction of WGS, and produce hydrocarbons of low molecular weight and reduced carbon residue and sulfur content.

The authors [15,20] state that active hydrogen can be obtained through WGS, which exhibits greater activity for hydrogenation than molecular hydrogen. Due to this, it is estimated that the catalytic activity of the material towards WGS can be directly correlated with its catalytic efficiency in the improvement of oils in the presence of water. Sato [15] describes a heavy oil upgrading process with supercritical water. First, partial oxidation of oil occurs to form CO. Subsequently, active hydrogen is produced by WGS, and the intermediate reagents from the oil decomposition are hydrogenated by it, thus lightening the oil.

According to authors [22,23], the WGS reaction is claimed to play an important role in the catalytic upgrading of heavy crude in the presence of steam, as it produces the hydrogen required for active chain termination, reducing free radical recombination or active chains formed from cleavage. of C-C, C-S, C-N, and C-O bonds that can form larger molecules. The same authors mention the effect of water as follows:

$$\text{heavy oil } + \text{ H}_2\text{O}$$
$$\rightarrow \text{ light hydrocarbon } + \text{ gases } (\text{C}_1 - \text{ C}_5, \text{H}_2, \text{CO}, \text{etc.}) \quad\quad (6)$$
$$+ \text{ active chains}$$

$$\text{active chain} + \text{active H}_2 \ \rightarrow \ \text{low molecular weight compound} \quad\quad (7)$$

$$\text{activehain} + \text{active chains} \rightarrow \ \text{high molecular weight compound} \quad\quad (8)$$
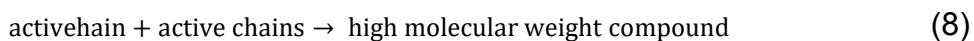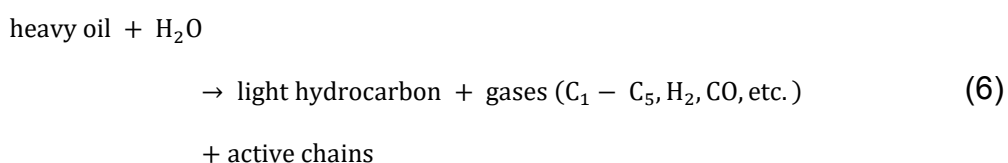
The synthesis gas (water gas or syngas) contains carbon monoxide and hydrogen. Usually, the WGSR is an intermediate step used for CO reduction and H_2 enrichment in the synthesis gas [23].

Steam reforming processes produce a gaseous mixture that mainly contains hydrogen and large amounts of CO. Through the WGSR this CO is converted to produce additional hydrogen [24]. The WGS reaction is expressed as follows:

$$CO + H_2O \leftrightarrow H_2 + CO_2$$

$$\Delta H^{\circ}_{298} = -41.09 \, KJ/mol$$

(9)
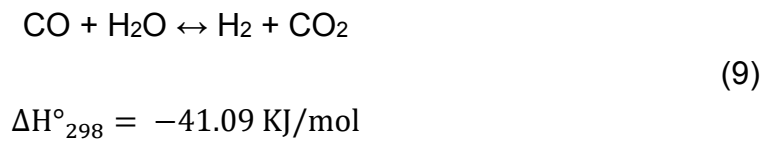
Under certain conditions, methanation reactions can occur, that is, hydrogenation of CO and CO_2 to produce methane, these secondary reactions consume H_2, therefore, the higher the CH_4 yield, the lower the H_2 yield. Some of the routes are the following:

$$CO + 3H_2 \leftrightarrow CH_4 + H_2O \qquad (10)$$

$$CO_2 + 4H_2 \leftrightarrow CH_4 + 2H_2O \qquad (11)$$

According to the literature [25,26], two mechanisms for WGS using ceria have been proposed. The redox (regenerative) mechanism suggests that the ceria redox process assists in the oxidation of CO to CO_2 and the reduction of H_2O to H_2. The associative mechanism proposes that water dissociates generating hydroxyls in ceria vacancies, and they react with CO to produce intermediate species (carbonate,

15

formate, or carboxyl) that decompose to produce CO_2 and H_2. According to both mechanisms, the presence of highly dispersed ceria, with a large available surface, would improve the catalytic behavior [26].

The different reaction pathways (**Figure 2**) are dependent on the nature of the catalyst surface (deposited metal, support, particle size, etc.) and reaction conditions (feed composition, temperature) [27,28].
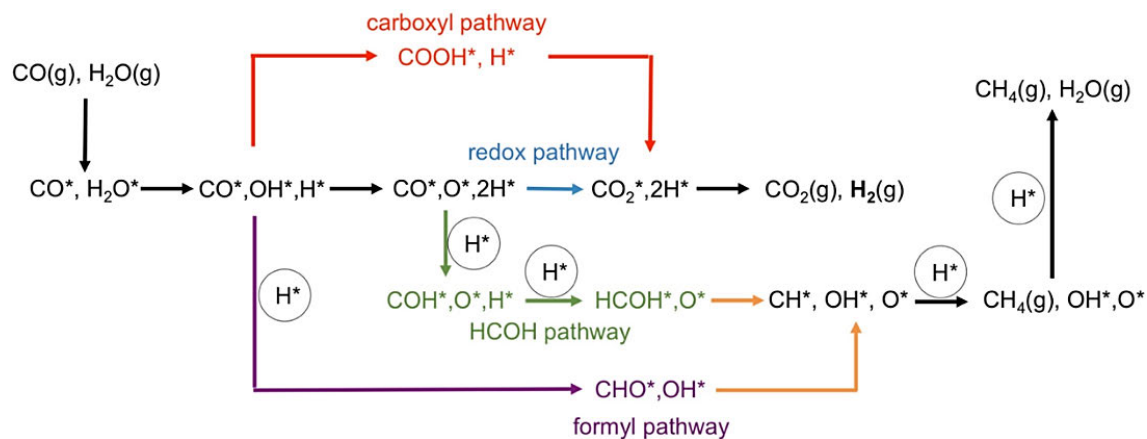
Figure 2. Schematic representation of the carboxyl (red), redox (blue), formyl (purple), and HCOH (green) pathways for hydrogen production. The orange arrows represent C-O bond scission steps. H* in the circle represents hydrogen consumed due to methanation. The asterisks (*) represent surface intermediates. Reproduced from Zhou et al. [28]

As can be distinguished in **Figure 2**, the redox and carboxyl pathways are favorable for WGS, while the formate and HCOH pathways favor methanation. Results from the microkinetic model in the work of Idrobo and Zhou [29] indicated that temperature, catalyst structure, particle size, and feed composition can affect WGSR

16

and methanation. They state that H_2O dissociation is beneficial for WGS but improving C-O bond cleavage will also increase selectivity to methanation.

According to Vovchok [30], both associative and redox mechanisms are possible on Ni and CeO_2 catalyst surfaces. Through in situ DRIFTS it was observed that, at 200 °C, bidentate formate may be playing an active role in the WGSR, potentially as an intermediate species in an associative pathway. However, a different mechanism (probably redox) may prevail at higher temperatures where the catalyst is more active.

Due to the controversy in the WGSR mechanisms regarding the dominant reaction pathway, the actual active sites, and the reaction active intermediate species, another work [25] explored the influence of nanometric ceria as active support in Ni-Cu/CeO_2 catalysts for WGS from 300 to 500 °C. The results revealed the presence of carboxylates as intermediate species on Ni-Cu/CeO_2 (CeO_2 with a large crystallite size of 17.2 nm), while only bidentate carbonate species were found on the Ni-Cu/CeO_2 (CeO_2 with size small crystallite, 12.7 nm). The authors attributed the low activity of the CeO_2 catalyst with the largest crystallite size to the presence of carboxylate species (inhibitor or slow decomposition rate to form CO_2 and H_2).

2.2. Selection of catalytic materials: properties and synthesis methods

2.2.1. General properties of supported catalysts

By definition, a heterogeneous catalyst is in a different phase than the reactants and products, hence it is a solid catalyst. The catalytic reaction occurs at the interface between the two phases and, consequently, the catalyst and the reactants and/or products can be separated very easily [31].

Supported catalysts are generally described as particles of an active component highly dispersed in a porous support (usually inert). The catalytic activity of these materials is said to occur at metal (oxide, sulfide) surface sites [31,32]. Starting from the premise that a smaller amount of metal is required because it is dispersed [33,34].

In addition to requiring high catalytic activity and selectivity towards the desired products, a catalyst must have stability and prevent particle growth processes that block the active sites or poison the active sites. The performance and stability of a catalyst are determined as a function of the density, nature, and accessibility of the active sites, with accessibility largely determined by the architecture of the support pore [32,35].

According to Neimark et al. [36], catalytic activity is the most important characteristic of a catalyst, and this depends on the composition of the catalyst phase, the concentration and dispersion of an active component, and the catalyst's efficiency (nature). In addition, the same authors point out that, although the composition of

the phases is the most important characteristic since it will determine the interaction between the support and the active phase, it is necessary to optimize the efficiency and dispersion of the active component.

The nature of a catalyst is determined by the composition, size, and shape of the nanoparticles. For example, some reactions are structure sensitive and are favored by specific surface sites such as low coordination sites found in defects, corners, steps, or edges. It is said that obtaining smaller nanoparticles causes an increase in the number of surface-active sites, and therefore in the catalytic activity [32].

2.2.2. Preparation Methods for Supported Catalysts

The synthesis method plays an important role in the catalyst, since the distribution and average size of the particles, the oxidation state, and the morphology, among other properties that define the nature of the catalyst, will depend on it. The most traditional methods are precipitation and impregnation, however, in the search to obtain catalysts with smaller and more uniform particle sizes, a better dispersion in the catalytic support, as well as the optimization of the synthesis processes, new synthesis methods emerge.

According to Campanati et al. [33], the most common methods to prepare supported catalysts include impregnation, ion exchange, adsorption and deposition, and precipitation. These are described below according to the authors.

- Impregnation: a certain volume of solution containing the precursor of the active phase is placed in contact with the solid support, which, in a subsequent step, is dried to eliminate the embedded solvent. There are two

methods of contact: wet impregnation, where there is an excess of solution and the solid separates and the solvent is removed by drying; and incipient wetness impregnation, in which the volume of the solution is equal to or less than the pore volume of the support.

- Ion exchange: occurs by the replacement of an ion in an electrostatic interaction with the support surface of a support by other ionic species.

- Adsorption: ionic species in an aqueous solution can be electrostatically attracted to charged sites on the surface of a solid. The charge on the surface of an oxide, and therefore the method of preparation of the supported catalyst, is influenced by the isoelectric point of the oxide and the pH and ionic strength of the solution.

- Deposition-precipitation: there is first the precipitation of bulk solutions or interstitial fluids and later there is interaction with the surface of the support. Precipitation in the bulk solution should be avoided, as it leads to deposition outside the pores of the support. The nucleation rate must be higher at the surface than in the bulk solution and the homogeneity of the solution must be preserved.

2.2.2.1. Synthesis of nanoparticles by the polyol method

The polyol method or polyol synthesis includes the use of high-boiling multivalent alcohols. **Table 1** shows some of these polyols, the simplest of which is ethylene glycol. Within these polyols, ethylene glycol (EG), diethylene glycol (DEG), glycerol

(GLY), and butanediol (BD) are generally most often used for the preparation of nanoparticles [37].

Table 1. Polyols and their boiling point [37].

Polyol	Name and Acronym	Boiling point (°C)
HO-CH$_2$-CH$_2$-OH	Ethylene glycol (EG)	197
HO-CH$_2$-CH$_2$-O-CH$_2$-CH$_2$-OH	Diethylene glycol (DEG)	244
HO-(CH$_2$-CH$_2$-O)$_2$-CH$_2$-CH$_2$-OH	Triethylene glycol (TrEG)	291
HO-(CH$_2$-CH$_2$-O)$_3$-CH$_2$-CH$_2$-OH	Tetraethylene glycol (TEG)	314
HO-(CH$_2$-CH$_2$-O)$_n$-CH$_2$-CH$_2$-OH	Polyethylene glycol (PEG)	>350 (decomposition)
HO-CH$_2$-CH$_2$- CH$_2$-OH	Propanediol (PDO)	213
HO-CH$_2$-CH$_2$-CH$_2$-CH$_2$-OH	Butanediol (BD)	235
HO-CH$_2$-CH$_2$-CH$_2$-CH$_2$-CH$_2$-OH	Pentanediol (PD)	242
HO-CH$_2$-CH$_2$-(OH)-CH$_2$-OH	Glycerol (GLY)	290
C(CH$_2$OH)$_4$	Pentaerythritol (PE)	276 (10^2 Pa)

The biggest advantage of polyols is that they show solubilities of compounds (precursor salts) near water, making these substances equivalent to water, but with a high boiling point. To obtain nanoparticles it is required that the products (nanoparticles) are insoluble in the polyol, promoting the precipitation of the nanoparticles. The solubility of polar compounds and salts in water occurs because

of the enormous polarity. Despite their lower polarity than that of water (see **Table 2**, relative permittivity has a direct relationship with fluid polarity [38]), polyols turn out to have a solubility close to that of water due to their chelating properties. Additionally, the chelating effect of polyols is favorable in the synthesis of nanoparticles since it favors the addition of polyols to the surface of particles. Due to their high viscosity (1.3 and 0.9 mPa*s for SDRs and EG at 150 °C [39]) in comparison to water, they serve as colloidal stabilizers. This is beneficial for controlling nanoparticle nucleation, growth, and agglomeration [37].

Table 2. Relative permittivity of water and common polyols [37].

Material	Relative Permittivity at 20 °C (ε_r)
Water	80
Glycerol	43
Ethylene glycol	37
Diethylene glycol	32

As for the boiling point of polyols (see **Table 2**), it allows to reach synthesis temperatures of 200-320 °C, without the need to use high pressures or autoclaves. In this way, it is possible to obtain crystalline nanomaterials. Another important advantage is that polyols become reducing agents at high temperatures. Consequently, the polyol can instantly reduce dissolved metal cations to easily form metal nanoparticles with sufficient surface functionalization and stabilization in excess polyol solvent. Furthermore, polyol synthesis can be thought of as a one-pot reaction [37].

Komarneni et al. [40] point out that polyols, specifically EG, act as reducing agents by the general reaction mechanism, represented by the following equations, where *M* is the metal reduced by this method.

$$2CH_2OH - CH_2OH \rightarrow 2CH_3CHO + 2H_2O \qquad (12)$$
$$2CH_3CHO + M(OH)_2 \rightarrow CH_3 - CO - CO - CH_3 + 2H_2O + M \qquad (13)$$
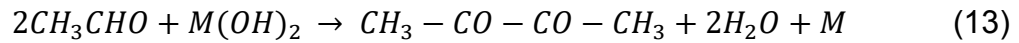
The authors [40] describe the mechanism as follows. First, the metal hydroxide crystallizes, followed by the precipitation of the intermediate phase by progressive dissolution of the starting hydroxide and detachment of water. In the second stage, the dissolution of the intermediate phase occurs leading to the reduction of the solution and the shedding of the volatile products of the reaction, followed by homogeneous nucleation and growth of metal particles.

2.2.3. Catalysts for WGSR

According to Pal et al. [24], it is necessary to choose an appropriate catalyst to achieve large-scale hydrogen production from synthesis gas. This author classified these materials into 5 categories: high-temperature catalysts, low-temperature catalysts, ceria- and noble-metal-based catalysts, carbon-based catalysts, and nanostructured catalysts. In addition, he says that some of the important characteristics of the catalysts for WGSR are the availability of oxygen vacancies, activity for water dissociation, and low CO adsorption strength.

Regarding the selectivity of the catalysts towards the production of hydrogen by WGS, according to Ashok [27], some of the strategies that can be applied to suppress methanation include; a) optimization of the CO adsorption force on the

metal active, b) increase in the density of hydroxyl groups, and c) improvement of the metal-support interaction.

As mentioned in several articles [24,25,41,42], ceria and ceria-based materials have excellent catalytic activity, due to their redox activity (ability to change oxidation state Ce^{4+}/Ce^{3+}), which is closely related to the formation of oxygen vacancies.

It is accepted in the literature [43] that modifying ceria with metals provides a higher oxygen storage capacity and an improved reduction capacity in contrast to pure ceria. Furthermore, it is said that the addition of doping metals to ceria can have two consequences: increasing the number of oxygen vacancies in the ceria structure and improving the thermal stability of the catalysts by preventing the aggregation of supported metals and ceria [44].

It has been mentioned that the nickel-ceria system is very active compared to catalysts containing other noble metals [10]. It is generally agreed that the reaction mechanism for this system is that reduced nickel interacts with CO, while partially reduced ceria (CeO_x) species dissociate water [10,45,46].

Although nickel-based catalysts have high catalytic activity, their use has been limited because they are also highly active towards the hydrogenation of CO and CO_2 to produce methane (methanation reaction) [27].

Table 3 shows some of the works published with catalysts based on nickel and ceria for the WGS reaction. As can be seen, in general, the $Ni-CeO_2$ system has provided good results in terms of catalytic activity and selectivity towards H_2, it is worth

mentioning that the operating conditions of the catalytic reaction are also determinant for the conversion. Likewise, also it is worth emphasizing that the preparation of most of the obtained materials used synthesis methods involving high temperature, pressure, and/or preparation time. In addition, the catalytic supports used are often expensive.

Table 3. Comparison of Ni and CeO$_2$-based catalyst materials used for WGS.

Catalyst	Synthesis Method	WGSR conditions	Results	Ref.
Ni/CeO$_2$-Al$_2$O$_3$	Incipient wetness impregnation, 75 °C, 12 h.	At 450 °C, CO/steam 1:3, GHSV = 207 L h^{-1} gcat^{-1}.	Activity of 95%,52% (V/V) H$_2$ yield, 73% selectivity towards H$_2$.	[43
Ni$_x$CeO$_2$/C	wet impregnation, 353 K for 12 h.	413K to 633K. Feed (molar %) 1.75 CO, 35.92 H$_2$O, 34.45 H$_2$, y 1.12 CO$_2$ en He. Contact time 0.09 g s/ml.	97% CO conversion.	[44]
1%Ce3%Ni/MFI	Hydrothermal at 463 K for 40 h	504 K and WHSV = 0.099 h-1.	18.6% CO conversion and 50% selectivity towards H$_2$	[45]

2.2.4. Graphene-based materials as catalytic supports

Graphene is a 2D material consisting of a single layer of carbon with sp2 hybridization, it can be considered a basic structural element of different carbon allotropes (3D bulk graphite, 1D carbon nanotubes, and 0D fullerenes) [50]. Their

unique structural characteristics are said to provide graphene-based catalysts with the following advantages [51]:

1. They have a high specific surface area, allowing a high density of active surface sites.

2. Due to their excellent mechanical properties, high stability and durability, graphene materials can be used as a catalyst or as a catalytic support.

3. It has high thermal and electrical conductivity; it is beneficial for the conduction and diffusion of heat generated during catalytic reactions, especially for exothermic reactions; Its high electrical conductivity makes it a good candidate for electrocatalysis.

4. Offer a setup in which to combine theoretical research, model research and realistic applications in catalysis.

Graphene nanoplatelets (GNPs) consist of graphitic materials with two-dimensional (2D) shapes, i.e., graphene multilayers. They have an ABA or ABCA stack and have dimensions less than 100 nm [52]. The multilayer nature of GNPs is said to make them uncompetitive with single-layer graphene in terms of physical properties, however, the trade-off between performance and economic viability makes GNPs a promising candidate for real applications [53].

2.2.5. Hydrogen Spillover

The Spillover phenomenon was first observed in the 1960s by several groups. This phenomenon was defined at the 2nd International Spillover Symposium as the

migration of adsorbed species from a solid phase where it is easily adsorbed, to another solid phase, which is in contact with the first, where it is not adsorbed directly [54,55].

Conner and Falconer [56] represented the spillover as shown in **Figure 3**. In addition, the authors note that spillover can take place from one metal to an oxide, from one metal to another, from one oxide to another, or from one metal oxide to another metal. In the hydrogen spillover from a metal to an oxide, hydrogen (H_2) usually dissociates into the metal as atomic hydrogen (H), which is then spilled onto the oxide support.
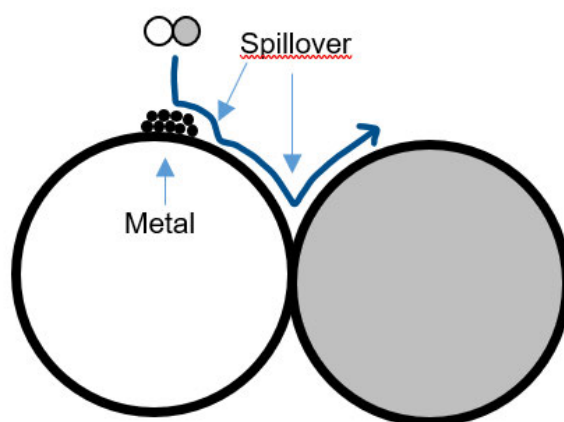
Figure 3. Schematic representation of the Spillover: from the surface of an adsorbent metal to a support, and then to another surface in contact with the support. Adapted from the literature [56].
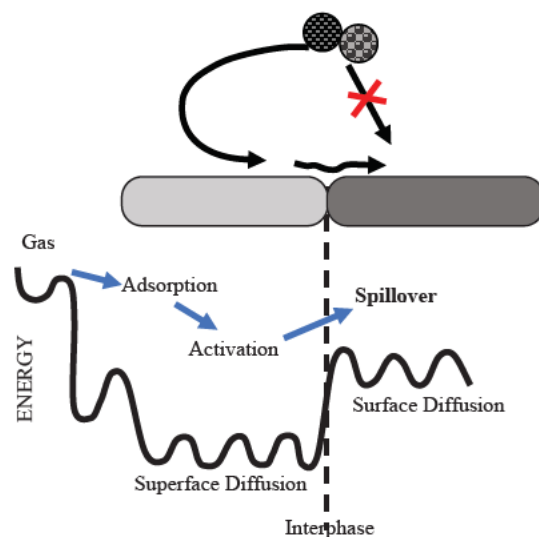
Figure 4. Schematic representation of the spillover of a diatomic gaseous molecule from an adsorbent surface to a non-adsorbent surface. A diagram of the energy level for the processes is shown [56].

Regarding the Ni/CeO$_2$ system, the work of Herrmann et al. [57] states that the increase in the partial pressure of hydrogen at the methanation temperature (573 K) causes an increase in electrical conductivity. Therefore, nickel dissociates hydrogen into atoms capable of spillover on the surface of the ceria as protons. A permanent and reversible electron transfer between ceria and nickel depends on the partial pressure of hydrogen.

The same authors represent with equations 14 and 15 the dissociative adsorption of hydrogen on the surface of nickel atoms and the migration (or spillage) of hydrogen atoms in the support, where they are adsorbed at anionic sites, thus producing hydroxyl groups and releasing free electrons to the support. They obtained a high catalytic activity and inferred that the active sites are formed by a surface nickel atom at the metal-support interface in the vicinity of an anionic vacancy in the support.

$$H_{2\,(g)} + 2Ni_s \rightleftharpoons 2Ni_s - H \tag{14}$$

$$2Ni_s - H + O^{2-} \rightleftharpoons Ni_s + OH^- + e^- \tag{15}$$
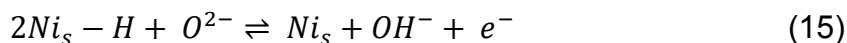
Prins [58] states that hydrogen spillover must lead to a net transport of hydrogen atoms to be effective in catalysis. The first requirement for this to happen is a thermodynamic driving force between the point of creation of the hydrogen atom, by hydrogen dissociation, in the metal particle and the site where hydrogen is used for hydrogenation. The second prerequisite is a means of transport of the hydrogen atoms on the support surface.

Therefore, in the literature [55,59] it is proposed that a test to verify that the spillover is carried out can be performed by FTIR spectroscopy, looking for evidence of hydrogen-deuterium isotopic exchange (H-D exchange). It is assumed that deuterium atoms, generated on the surface of the metal (assuming a metal catalyst) by dissociative chemisorption of deuterium, migrate over the support (reducible support), where they are exchanged with the hydrogen atoms of the OH groups of the support [60].

According to Schimming [61], the contribution of carriers to hydrogen dissociative adsorption is relevant to a variety of catalytic reactions, such as hydrogenation, hydrodeoxygenation, and WGS, and must be considered to truly understand the catalytic performance of these materials.

3. CHARACTERIZATION OF GRAPHENE-BASED SUPPORTS

3.1. Materials and methods

3.1.1. Materials

The support materials were commercially sourced from Graphene Supermarket. In the case of graphene, it is in the form of nanoplatelets (GNPs) with an average thickness of less than 3 nm (between 3-8 graphene monolayers) and 2-8 μm of lateral dimensions. The other catalytic support (OGNPs) is also in the form of nanoplatelets but functionalized with oxygen. The functionalization was performed with a plasma treatment, which exfoliates the graphene sheets, typically obtaining a thickness of less than 50 nm and 0.3 to 5 μm of lateral dimensions.

3.1.2. Raman Spectroscopy

Raman Spectroscopy was conducted on the graphene supports using the inVia Basis Renishaw system with a laser radiation source with a wavelength of 532 nm. The sample was attached to a glass slide on double-sided tape for the analysis.

3.1.3. Fourier Transform Infrared Spectroscopy (FTIR)

The Nicolet iS10 equipment was used in the transmission mode to characterize the pristine supports with the FTIR technique. To do this, less than 1mg of sample was diluted in 100 mg of KBr previously dried at 100 °C, the materials were ground to obtain a fine and homogeneous powder, which was pressed at 30 kN to obtain a pellet.

3.1.4. X-ray Diffraction (XRD)

XRD was used to characterize untreated materials, identify and quantify crystalline phases, and estimate crystallite sizes. The SmartLab RIGAKU equipment was used in a 2θ interval from 10° to 90° and steps of 0.01°.

3.1.5. Scanning Electron Microscopy (SEM)

The support materials were observed by SEM in the FEI Helios NanoLab 600i equipment with a double beam and a secondary electron detector operated at 5 kV. The same equipment and conditions were applied for semi-quantitative elemental analysis (SEM-EDS). The samples were attached to aluminum pins on a layer of silver paint.

3.2. RESULTS AND DISCUSSION

3.2.1. Structural-Chemical properties

The Raman spectra of the GNP and OGNP supports, shown in **Figure 5**, present the characteristic bands of graphitic materials. The D-band (1350 cm^{-1}) is a double-resonant Raman mode, which can be understood as a measure of the structural disorder that comes from amorphous carbon and any defects. Like the D-band, the D' band is a Raman double resonance feature induced by disorder, defects, or ionic intercalation between graphitic walls [62].

The G-band (1500-1600 cm^{-1}) originates from the tangential vibrations of the carbon-carbon bonds within the graphene sheets.
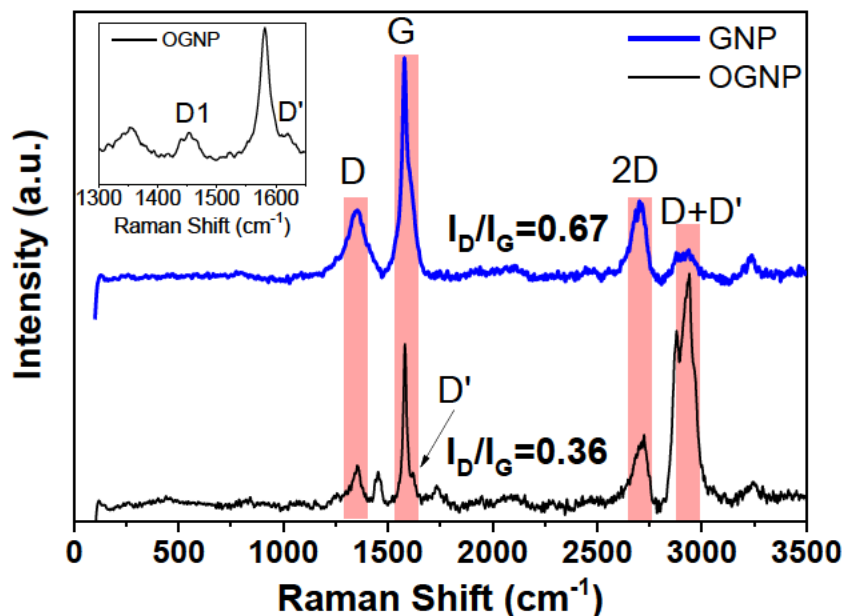
Figure 5. Raman spectra of GNP and OGNPs

The ratio of intensities of the D and G bands, $R = I_D/I_G$, can be used to evaluate the density of the disorder of the material, a higher value of R, indicates greater disorder of the material [63]. The I_D/I_G ratio is lower in the OGNP sample ($I_D/I_G = 0.36$), corresponding to a material with a higher graphitization degree than GNP ($I_D/I_G = 0.67$). In addition, in the OGNPs sample, other characteristic bands are attributed to defects or ionic intercalation, such as D + D'. The band called D1, in the OGNP spectrum (~ 1450 cm^{-1}), is attributed to the functional groups COOH/C-OH and C=O/C-O [64].
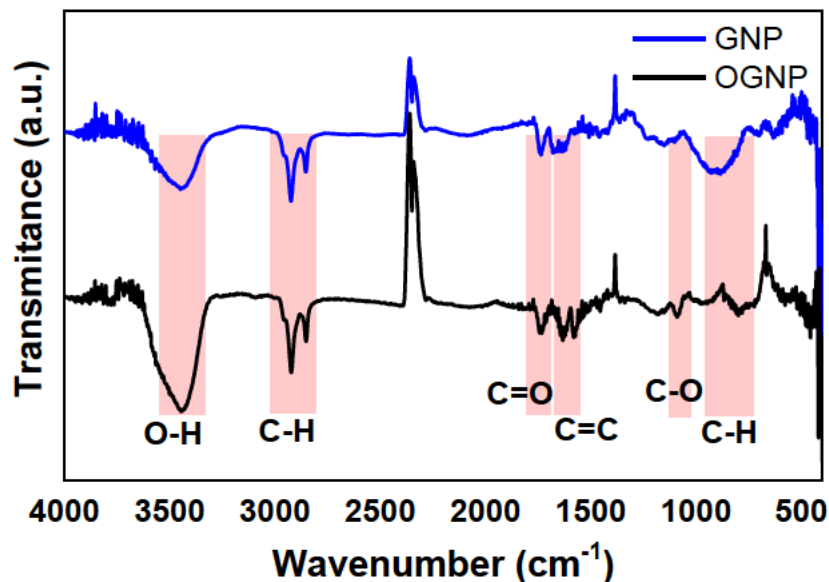
Figure 6. FTIR spectra of GNPs and OGNPs

Figure 6 shows the infrared spectra obtained from the GNPs and OGNPs samples. The broad band in the range of 3600 to 3200 cm^{-1} is assigned to the O-H stretching vibrations of hydroxyl groups, this signal can be observed in both spectrums, however, in the OGNP spectrum it has greater intensity, in addition to being accompanied by a peak at 1086 cm^{-1} attributed to the C-O stretching of primary alcohols. In addition, oxygen-functionalized nanoplatelets have a peak around 1730 cm^{-1} due to the C=O stretching of unsaturated esters or formats. Peaks around 2800 and 2900 cm^{-1} are assigned to C-H stretching of alkanes and alkenes, just as peaks at 800 cm^{-1} are due to C-H bending. Finally, the 1650-1600 cm-1 peaks are caused by the stretching vibrations C=C of conjugated alkenes.

3.2.2. Morphology and Structural-Crystalline Properties

The XRD analysis of pristine supports (GNP and OGNPs) displays other structural differences between them (see **Figure 7**). Both materials were identified with the graphite phase (ICSD code 98-007-6767), which has a hexagonal structure (parameters a and b=0.246nm, c=0.671 nm). For both materials, the peak with greater intensity is centered around $2\theta = 26.5°$ and corresponds to the diffraction of the plane (200), with a space between sheets, d, which corresponds to the interplanar distance calculated by the equation representing Bragg's law.
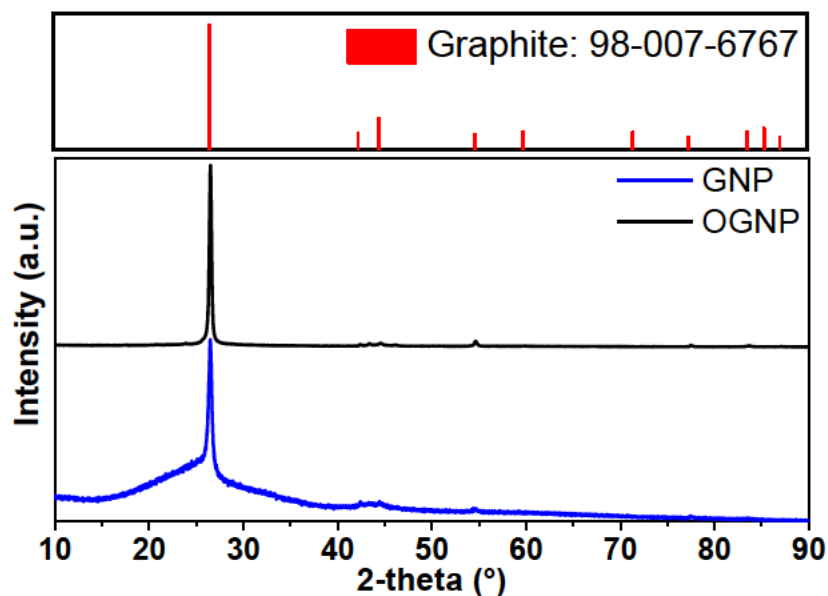
Figure 7. Diffractograms of supports, GNPs and OGNPs

The crystallite size, β, corresponds to the estimated thickness of the nanoplatelets, which in turn are composed of n number of layers, which can be estimated by the β/d ratio [65]. The results obtained with these dimensions are summarized in **Table 4**.

Table 4. Results obtained by XRD of the graphene-based supports.

Sample	2θ $_{(200)}$	d$_{(002)}$	β (nm)	n
GNPs	26.45	0.34	20.3	59
OGNPs	26.48	0.34	36.3	106.7
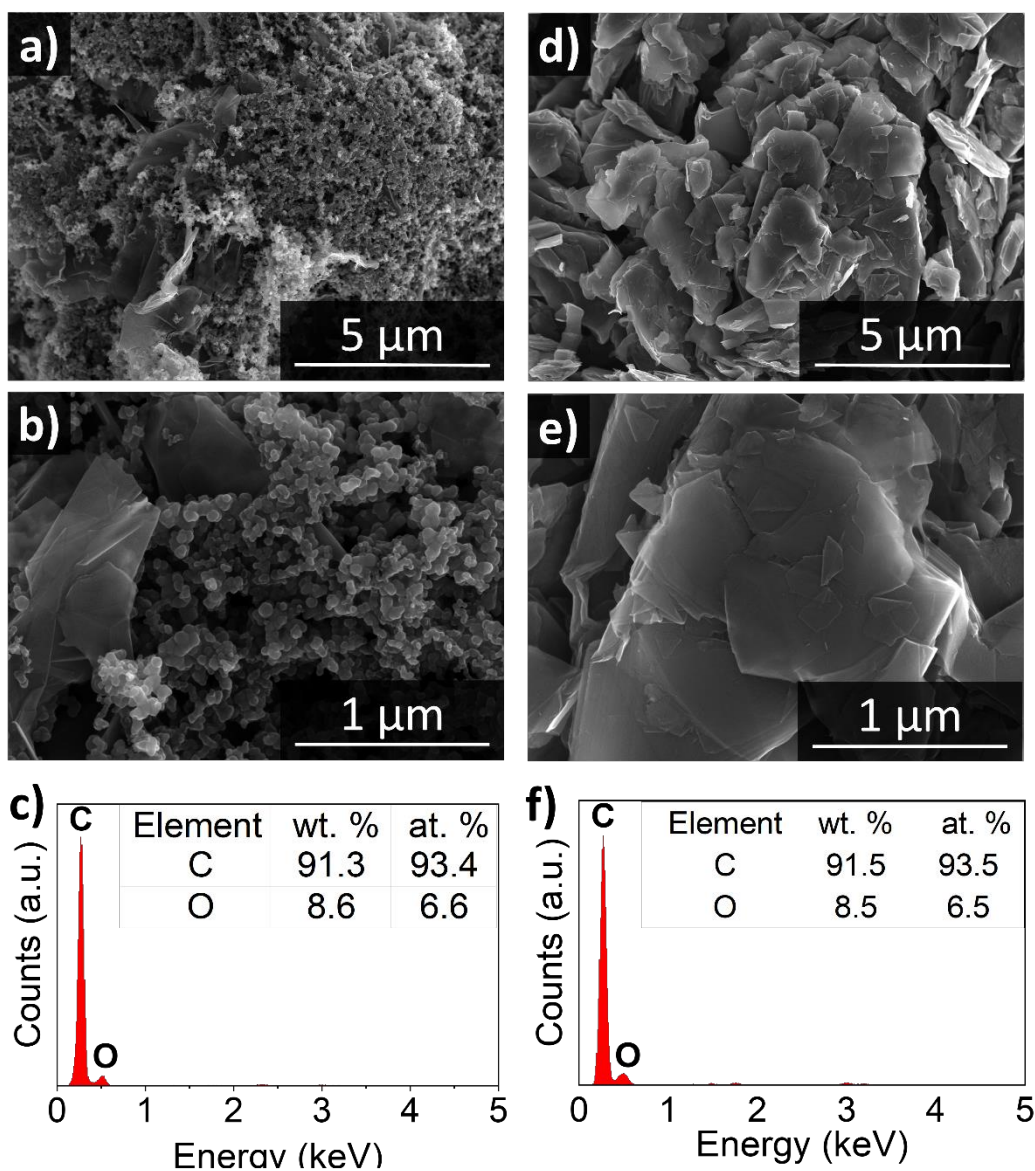
Figure 8. Scanning micrographs at 25000X and 50000X, and EDS of (a, b, c): graphene nanoplatelets, and (d, e, f): oxygen-functionalized graphene nanoplatelets.

In the scanning micrographs of the supports, presented in **Figure 8**, morphological differences between them can be seen. In the case of GNPs, thin and folded sheets are observed, with particles agglomerated between them. In the case of the OGNP sample, very defined platelets are observed and formed by several smooth sheets, without agglomerations. EDS elemental analysis of both materials provided similar results, with percentages by weight of about 91% carbon and 8.5% oxygen. The oxygen content in GNP is explained by functional groups present at the edges of the particles, including ether, hydroxyl and carboxyl groups [66].

3.3. Remarks

Although both supports comprise graphene nanoplatelets, FTIR and Raman spectroscopies showed the presence of functional groups mainly in OGNPs. There are also functional groups in the GNP support, but in lower quantities. In addition, XRD and SEM distinguished structural differences of materials, especially in terms of the size (thickness) of the platelets, this could influence the surface area of the graphene-supported catalysts.

4. SYNTHESIS AND CHARACTERIZATION OF GRAPHENE SUPPORTED CeO$_2$

4.1. Materials and methods

4.1.1. Synthesis Method

The synthesis of cerium dioxide nanoparticles was performed by the microwave polyol method (ETHOS UP MILESTONE), reported by Soren, at 200 °C for 10 min using ammonium nitrate and cerium (IV) (Ce(NH$_4$)$_2$(NO$_3$)$_6$) as a precursor (purity ≥98.5%, Sigma Aldrich) in 1,4-butanediol (99%, Sigma Aldrich) as solvent [67]. The modification of the synthesis method consists of adding graphene at the beginning of the reaction, to obtain ceria nanoparticles deposited in GNP and OGNP in a single step. Precursor/support weight ratios of 1:1, 1:2 and 1:3 were used, expecting to obtain CeO$_2$ percentages of 23.9, 13.6 and 9.5% by weight, respectively. CeO$_2$ samples deposited on GNP were labeled as 1Ce1G, 1Ce2G, and 1Ce3G; according to the relationships mentioned above, while the materials deposited on OGNP were called: 1Ce1GO, 1Ce2GO and 1Ce3GO.

4.1.2. X-ray Diffraction (XRD)

XRD was used to characterize untreated materials to identify and quantify crystalline phases and estimate crystallite sizes. The SmartLab RIGAKU equipment was used in a 2θ interval from 10° to 90° and steps of 0.01°.

4.1.3. Scanning Electron Microscopy (SEM)

The morphology and NPs dispersion regarding the CeO$_2$/GNPs and CeO$_2$/OGNPs materials were determined by SEM in the FEI Helios NanoLab 600i equipment with

a double beam and a secondary electron detector operated at 5 kV. The same equipment and conditions were applied for semi-quantitative elemental analysis (SEM-EDS). The samples were attached to aluminum pins on a layer of silver paint.

The FEI-QUANTA FEG-250 microscope with an operating voltage of 30kV was used to obtain images with the backscattered electron detector (BSE) and compare them with those of the secondary electron detector (SE) and thus attribute the morphology of the particles to different elemental compositions.

An elementary mapping was carried out in the FEI-QUANTA FEG-250 equipment operating at 25kV as an alternative to observing the dispersion.

4.1.4.   Coupled Plasma Atomic Emission Spectroscopy (ICP)

ICP was used to determine the elemental metal contents of Ce. Prior to the analysis, the sample was subjected to an acid digestion process, in which, 40 mg of sample and 20 mL of an acid solution (HNO_3:H_2SO_4, 5:1) were deposited in a Teflon container and heated to 10 °C/min from room temperature to 150 °C for 40 min, the solution obtained was measured to 50 mL.

4.1.5.   Boehm Titration Method

Boehm's method was implemented by potentiometric titrations. The standard operating procedure suggested by Schönherr was followed to obtain results with high precision during titration by the Boehm method [68].

The acid oxygen groups of the graphene supports (GNP and OGNP) were quantified, as well as each type of support with 9% CeO_2, that is, the samples 1Ce3G and 1Ce3GO. From each carbon material 3 samples of 0.15 g were taken and

subjected to a treatment by adding an alkali to the reaction ($NaHCO_3$, Na_2CO_3, and NaOH) and stirring for 4 days, in this way the acid groups on the surface of the carbon neutralize the base.

After the above, the unconsumed amount of the base was quantified by simple acid-base titration. Titrations were performed indirectly by adding a known excess of acid (HCl) to the alkali of the reaction (taking 2 aliquots per sample) and then titrating the acid solution of the analyte with the titrator base (Na_2CO_3). It is assumed that by using Na_2CO_3, CO_2 does not influence titration, so there is no need to degas or heat the aliquots to remove the dissolved CO_2. The measurements were made by alternating the samples for each carbon material, without changing the bases between them to reduce contamination of the instruments. The references were treated exactly as the samples.

4.1.6. Energy loss electron spectroscopy (EELS)

The EELS technique was used to collect information about oxidation states and structural modifications. It was applied only to a sample of ceria (CeO_2) sintered under similar conditions, the samples of ceria supported in GNPs and OGNPs (1Ce3G and 1Ce3GO) and graphene supports (GNPs and OGNPs). These samples were treated in an ultrasonic bath with isopropyl alcohol to disperse them. They were then mounted on charcoal-coated copper grids. The EEL spectra were acquired with the FEI Tecnai F30 TEM equipment operated at 300 kV. Using a power law adjustment model, the background was subtracted from all EEL spectra with Gatan Digital Micrograph software.

4.2. Results and discussion

4.2.1. Structural-crystalline properties

It was possible to identify the phases of cerianite and graphite in the diffractograms obtained for the samples of ceria supported in GNP and OGNP (**Figure 9**), whose contents by weight were estimated by refinement of Rietveld.
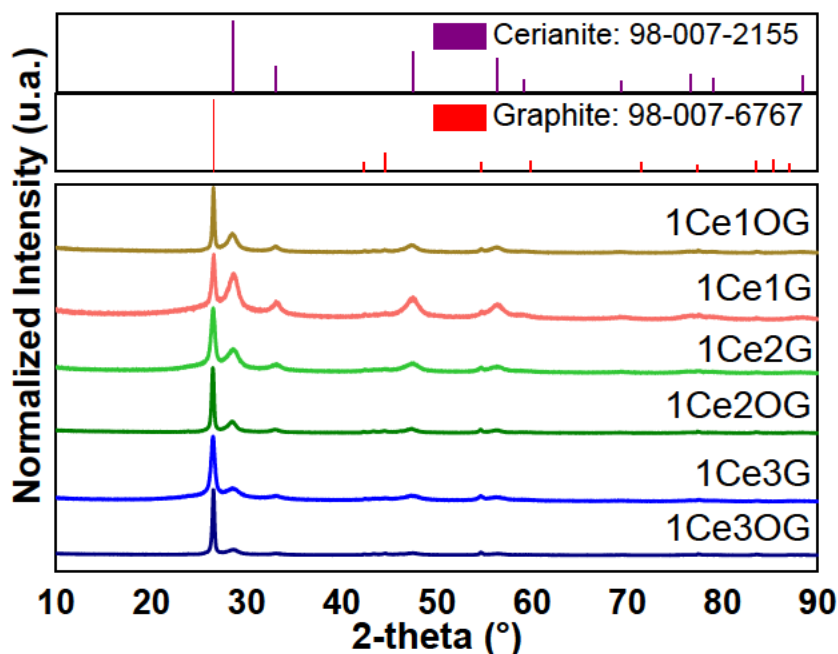
Figure 9. Diffractograms of CeO$_2$ samples supported in GNP and OGNPs.

The content by weight of cerianite, as well as its crystallite size, and the crystallographic parameters of the phase corresponding to graphene, are presented in **Table 5**.

It can be observed that there is a slight decrease in crystallite size, and the number of graphene sheets, with the addition of CeO$_2$ in materials with GNPs, which could be due to the separation of some sheets by interaction with metal oxide. This

happens oppositely in materials with OGNPs, possibly due to the presence of functional groups of oxygen that when interacting with the ceria induce an ordering of the sheets.

Table 5. Crystallographic parameters of CeO$_2$ samples supported in GNPs and OGNPs

Sample	$2\theta_{(200)}$ Graphite	$d_{(002)}$ (nm)	β Graphite (nm)	n Graphene	Wt. % Cerianite	β Cerianite (nm)
1Ce1G	26.5	0.34	12.2	35	21.6	5.6
1Ce2G	26.4	0.34	13.0	38	12.6	10.6
1Ce3G	26.4	0.34	14.0	41	9.6	6.8
1Ce1GO	26.5	0.34	37.7	108	24.4	4.5
1Ce2GO	26.4	0.34	37.7	108	14.4	5.7
1Ce3GO	26.5	0.34	35.2	103	11.2	4.3

Regarding ceria content in these materials, 9.5% CeO$_2$ was expected for those preparations with the precursor/solvent ratio of 1:3, 11%, and 23.9% for preparations with the 1:2 and 1:1 ratio, respectively. **Figure 10** shows the deviation between the actual and theoretical concentrations of CeO$_2$ in the materials. Concerning this graph, it can be said in a general way, that the synthesis method used allowed the obtaining of the materials in the proportions sought.
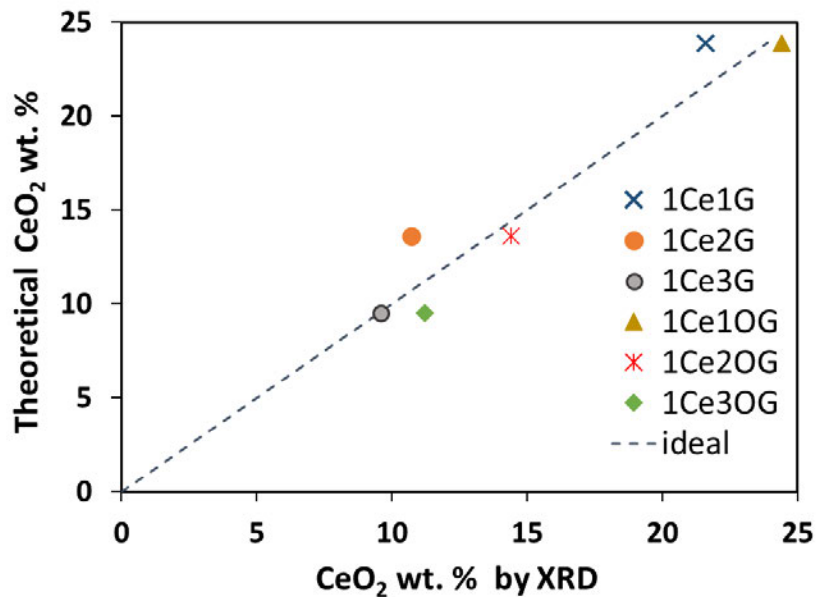
Figure 10. Deviation of CeO₂ concentration in the CeO₂/graphene materials.

4.2.2. Morphology and chemical composition

Figure 11 shows the scanning microscopy images at different magnifications obtained from CeO₂/GNP samples with different precursor/solvent ratios: 1Ce1G, 1Ce2G and 1Ce3G. The deposition of ceria particles on graphene sheets can be seen in these images. Likewise, the presence of agglomerations of particles similar to those of the GNPs material is observed, however, with the magnification to 100000X of the 1Ce3G sample (**Figure 12**), two types of particles were distinguished in these materials: smooth agglomerated particles, attributed to the carbon support; and spherical granulated particles, which are attributed to CeO₂ deposited on graphene.
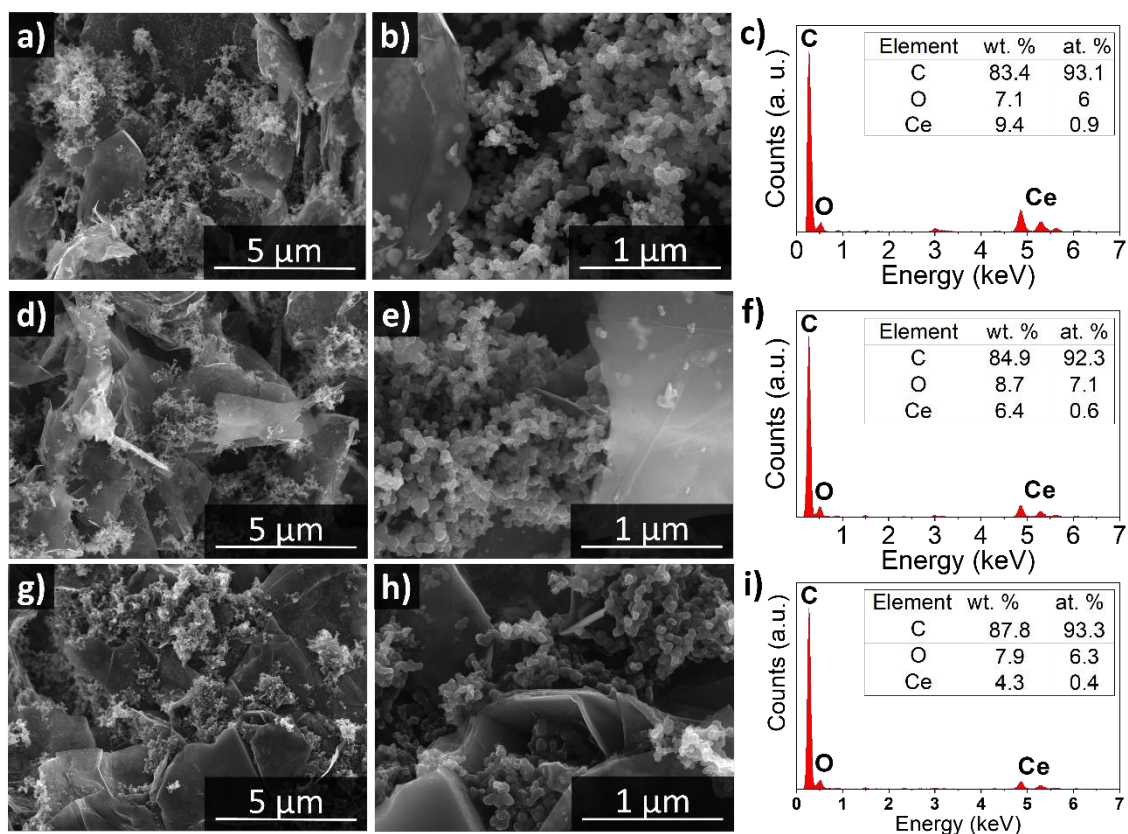
Figure 11. Scanning micrographs (SE) at 25000X and 50000X, and EDS of CeO₂/GNP samples with different ratios (a, b, c): sample 1Ce1G; (d, e, f): 1Ce2G sample; and (g, h, i): 1Ce3G sample.

Additionally, with the Quanta 250 electron microscope, images of the 1Ce1G sample were obtained at different magnifications (**Figure 13**), in which, although there is a lower resolution than the previous ones (acquired in Helios equipment), there is a backscattered electron detector (BSE), with which the contrast of the images can be attributed to the difference in atomic number of the elements present. In this case, it was confirmed that the smooth agglomerated particles observed in the SE detector can be attributed to the carbonaceous support since they do not present a contrast

in the BSE detector. On the other hand, it is observed with BSE that the sample presents small particles that glow, attributed to CeO_2 dispersed in the support.
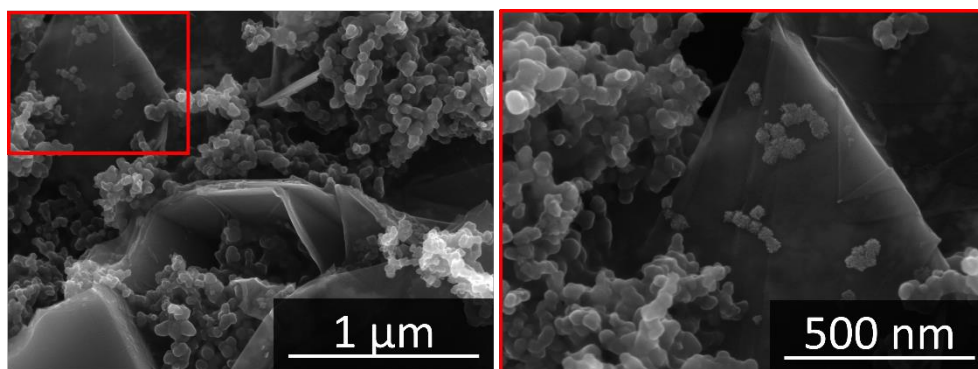
Figure 12. Scanning micrographs (SE) at 50000X and 100000X of 1Ce3G.
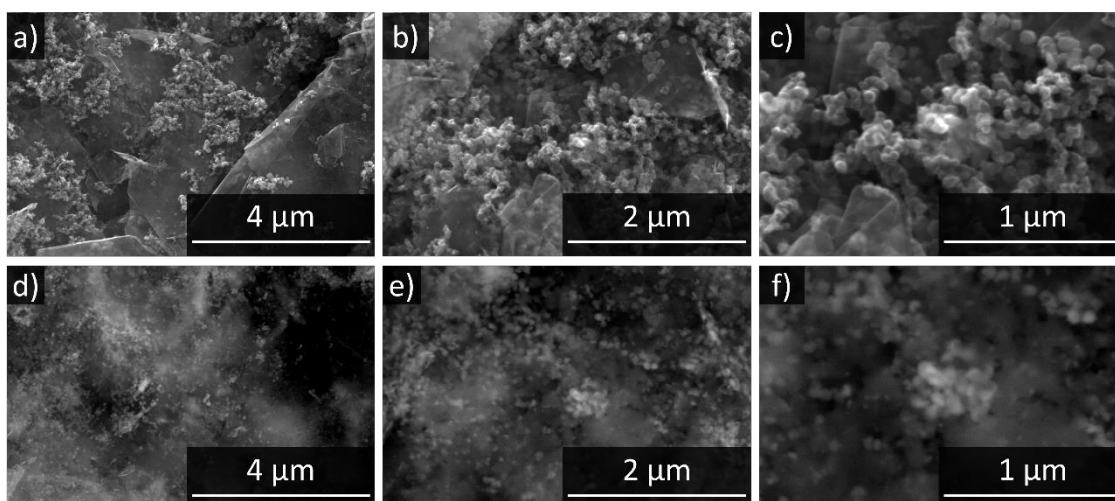
Figure 13. scanning micrographs of 1Ce1G 25000X, 50000X and 100000X with different types of detectors (a, b, c): secondary electron detector and (d, e, f): backscattered electron detector.

Figure 14 shows the scanning micrographs at different magnifications obtained from the CeO_2/OGNPs samples: 1Ce1GO, 1Ce2GO and 1Ce3GO. In them, the deposition of granulated and spherical ceria particles on graphene platelets is most remarkable. With the magnification of 350000X of the sample 1Ce3GO (**Figure 15**),

it is observed that these particles attributed to CeO_2 are made up of very small grains, apparently spherical, however, the resolution of the equipment was not enough to distinguish them clearly. It is worth mentioning that the size and shape of the ceria nanoparticles could favor the catalytic activity of composite materials by an effect of surface area and greater accessibility to the active sites of the catalyst.
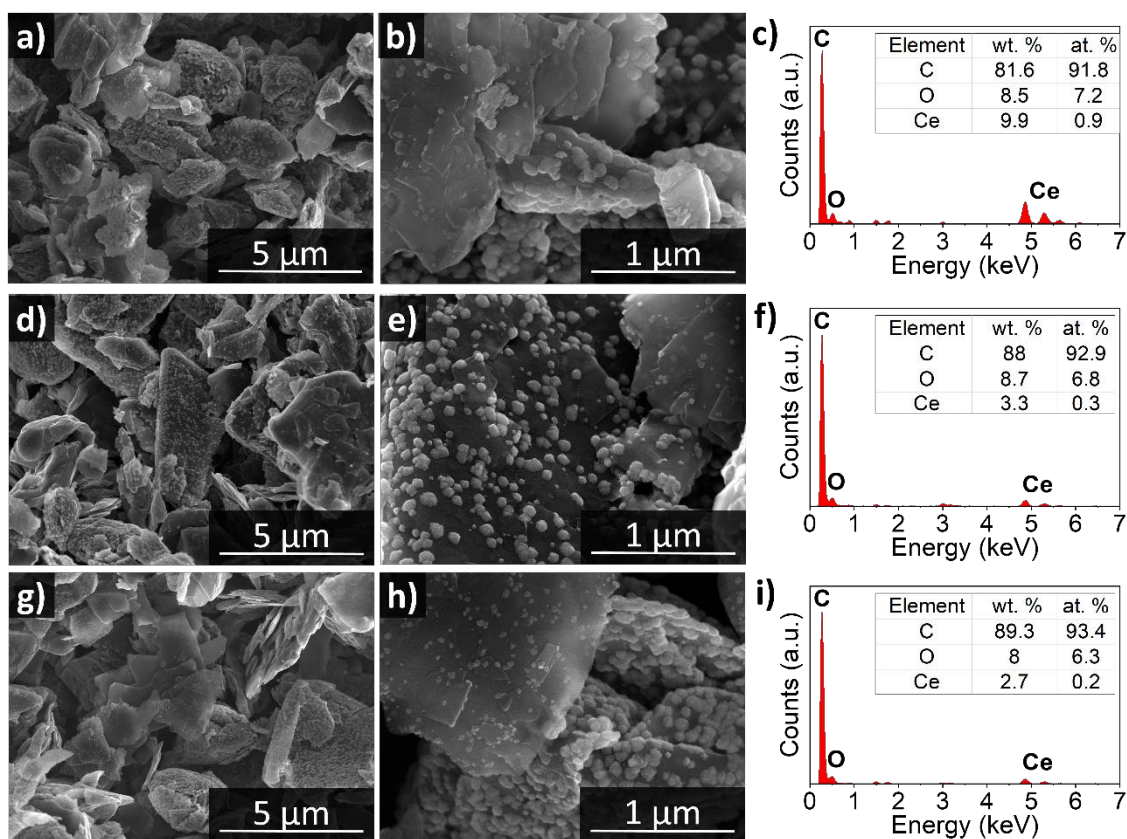
Figure 14. Scanning micrographs (SE) at 25000X and 50000X, and EDS of CeO_2/OGNP samples with different ratios (a, b, c): sample 1Ce1GO; (d, e, f): sample 1Ce2GO; and (g, h, i): 1Ce3GO sample.
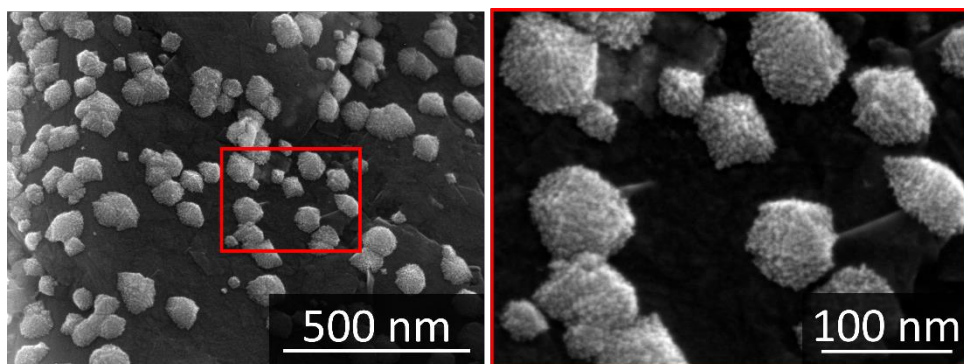
Figure 15. Scanning micrographs (SE) at 50000X and 100000X of 1Ce3GO.
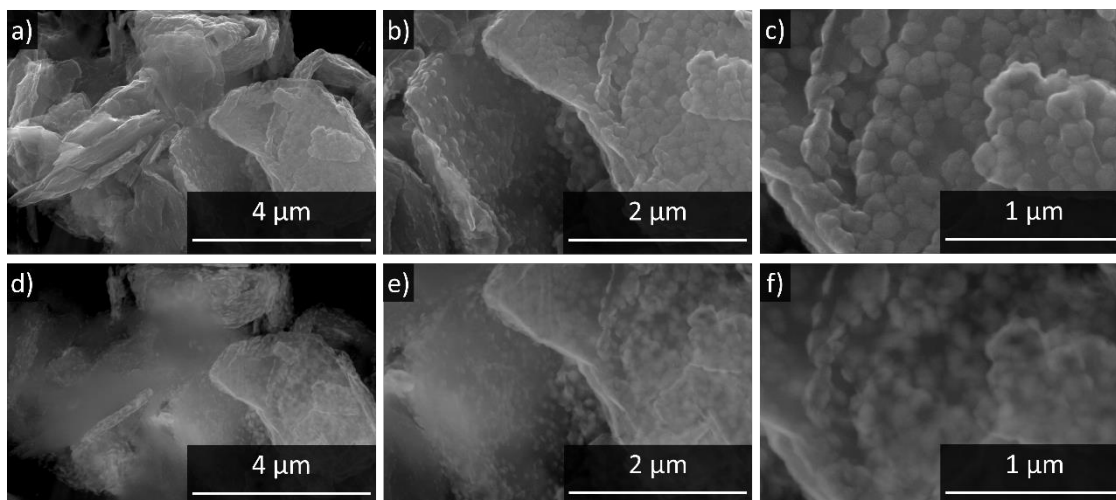
Figure 16. 1Ce1GO 25000X, 50000X and 100000X scanning micrographs with different types of detectors (a, b, c): secondary electron detector and (d, e, f): backscattered electron detector.

Similarly, **Figure 16** shows the micrographs of the 1Ce1GO sample. In the images with the backscattered electron detector (BSE), the contrast is appreciated by a difference in the atomic number of Carbon and Cerium (6 and 58), an effect of greater intensity in the scattered electrons when colliding with a larger nucleus. The lower contrast (brightness) in this sample compared to the 1Ce1G sample (**Figure 13)** could be because ceria is better dispersed on the surface of this material.

Table 6 shows the elemental cerium content by weight of each sample. Contrasting the values obtained from the measurements by EDS and ICP with the theoretical

value, the ICP analysis can be considered more appropriate since it considers a larger volume of the sample (bulk). This can be seen in **Figure 17**. In general, the values are close to the expected, so it is validated that the synthesis method is adequate to obtain ceria deposited with different concentrations.

Table 6. Weight content of elemental cerium in samples.

Sample	Theoretical Ce wt. %	EDS (1) Ce wt. %	ICP Ce wt. %
1Ce1G	19.4	9.4	14.1
1Ce2G	11.0	6.4	8.4
1Ce3G	7.7	4.3	7.0
1Ce1GO	19.4	9.9	15.5
1Ce2GO	11.0	3.3	8.7
1Ce3GO	7.7	2.7	5.9
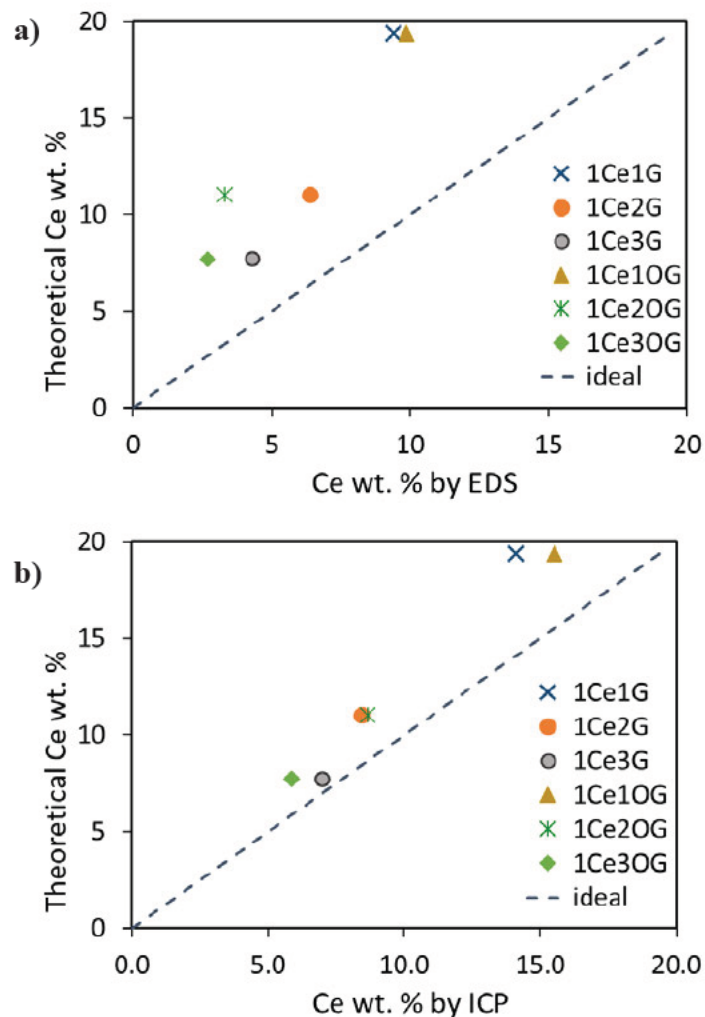
Figure 17. Deviation of elemental concentration of cerium by: a) EDS, b) ICP.

On the other hand, the elemental mapping of carbon, oxygen and cerium was carried out on the materials 1Ce1G and 1Ce1GO, and these are shown in **Figures 18 and 19,** respectively. In these figures the distribution of CeO_2 particles on the surface is not observed, this is attributed to the fact that the mapping, when taken with the BSE detector, provides information about the features that lie deep below the surface (> 1µm) [69].
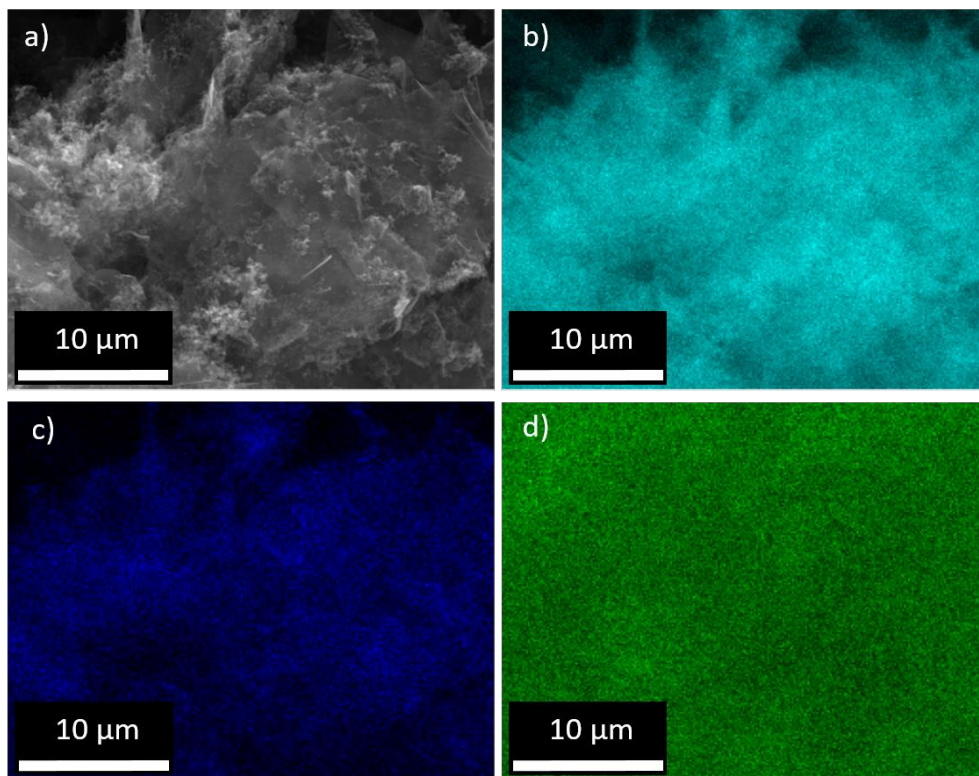
Figure 18. Elemental mapping of the 1Ce1G sample. a) image taken with BSE, b) carbon, c) oxygen, d) cerium.
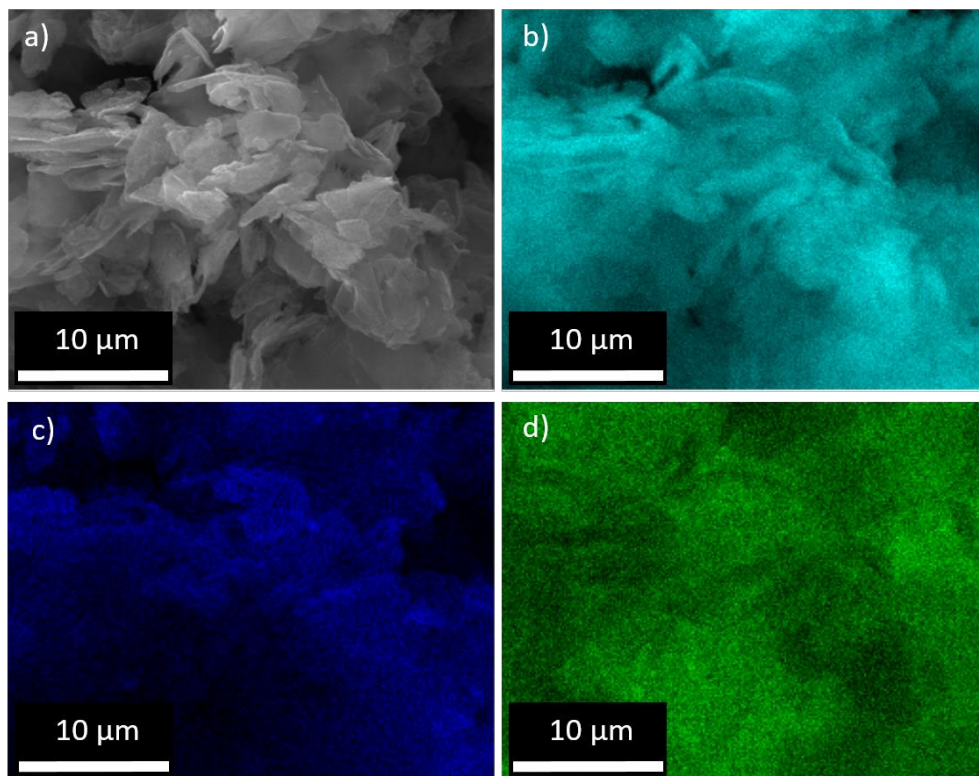
Figure 19. Elemental mapping of the 1Ce1GO sample. a) image taken with BSE, b) carbon, c) oxygen, d) cerium.

4.2.3. Interactions of CeO$_2$ deposition in graphene

4.2.3.1. Determination of acid sites by the Boehm method

Figure 20 shows the distribution of the concentration of oxygen-containing functional groups. On this occasion, the deviation of the samples in this sense is presented, since it can be compared without an effect due to the difference in the weights of each sample taken. It can be observed that samples containing CeO$_2$ present a greater dispersion of the data, this characteristic can be associated with the materials becoming less homogeneous with the addition of nanoparticles.
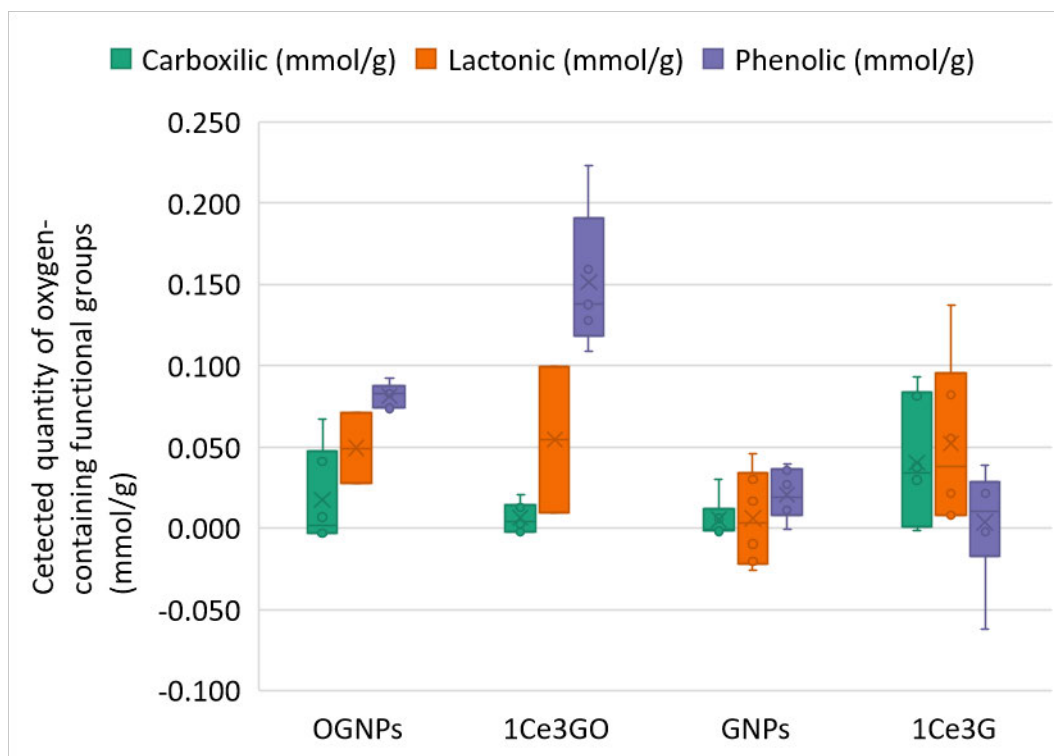
Figure 20. Dispersion of data in the quantification of oxygen-containing groups.

On the other hand, the quantification results averaged for each carbon sample are presented in **Figure 17**. When comparing the data presented, a remarkable contrast can be seen in the number of surface oxygen groups available between the 2 types of support, GNPs and OGNPs, being greater by an order of magnitude in the case of OGNPS (0.148 vs 0.058 mmol / g). In addition, it is observed that the total amount of these groups in both supports usually increases with the addition of nanoparticles, this could be due to the partial oxidation of graphene during synthesis and possible parallel deposition of CeO_2 nanoparticles.

In the work of Ren et al. [49], where the functionalization of graphene was carried out at different temperatures, it is said that by increasing the reaction temperature from 180 to 220 °C, the functionalities of the lactonic and phenolic groups change monotonically as a consequence of the increase in the esterification rate, while those of the carboxylic groups increase and then decrease due to equilibrium. between reaction yield and esterification consumption. In the case of reactions at 250 °C, carboxylic functionality was found to be greatly reduced, while phenolic functionality showed a significant increase. Based on this reference, the change in the distribution of functional groups of oxygen could be attributed to their interaction with the solvent used in the synthesis (butanediol), carrying out esterification and possibly cyclization reactions, as well as the reaction temperature (200 °C).
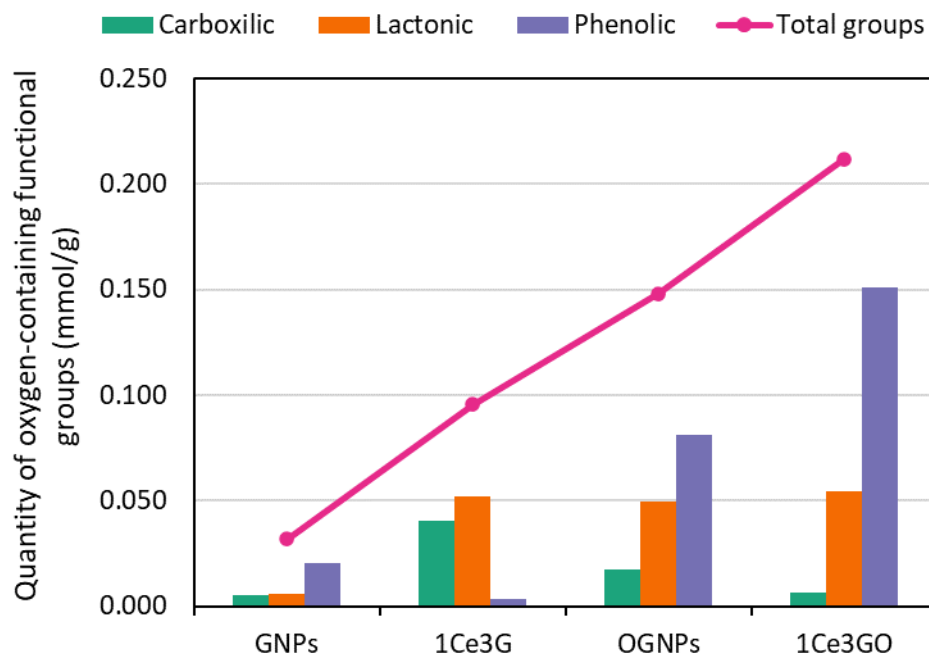
Figure 21. Content of surface groups determined by Boehm titration.

There is not much specific information on the interaction of graphene with ceria in the literature. However, Grewal et al. [70], mention that in ceria (100) (of the facets that fit best between the higher oxygens of ceria and the carbons of graphene), there is a formation of a covalent bond between the higher oxygens of ceria and graphene in the presence of hydroxyl groups.

The above happens differently in the case of the OGNPs support since a decrease in carboxylic groups is perceived so that the anchoring of the ceria could occur in these sites of acidic character. On the other hand, the number of phenolic groups increases by 60% of the 1Ce3GO sample concerning the support sample, OGNPs.

In the case of GNP support, there is an increase in the amount of carboxylic and lactonic groups with the deposition of CeO_2 nanoparticles, associated with the oxidation of graphene. However, the phenolic groups decrease, this could correspond to the anchoring of the ceria, in such a way that the electrons located on the surface of the ceria (generated by oxygen vacancies), can interact with these phenolic groups.

It is important to emphasize that the production or consumption of the different oxygen groups in the supports can be caused by oxidation with BD during the process of synthesis and deposition of nanoparticles. One way to verify this would be through the study of Boehm titrations with the supports subjected to these conditions (reaction with BD), however, it was not possible to carry out the analysis.

4.2.3.2. Determination of oxidation states and possible interactions by EELS

Figure 22 shows the EELS spectra obtained from the analysis of samples of pure and supported Ceria in GNPs and OGNPs, as well as the supports to identify and compare the significant signals. These were obtained for the edge regions corresponding to cerium, oxygen and carbon. The spectra were calibrated by adjusting the energy to each element: Ce M5 (883 eV), O-K (532 eV) and C-K (284 eV). The O-K signal corresponds to CeO_2-associated oxygen and the C-K signal comes from graphene. During the analysis in different regions of the graphene samples (GNPs and OGNPs), including at the edges of the sheets, it was not possible to identify signals belonging to the oxygen associated with graphene, which

may be because it is below the detection limit of the equipment under the conditions used.
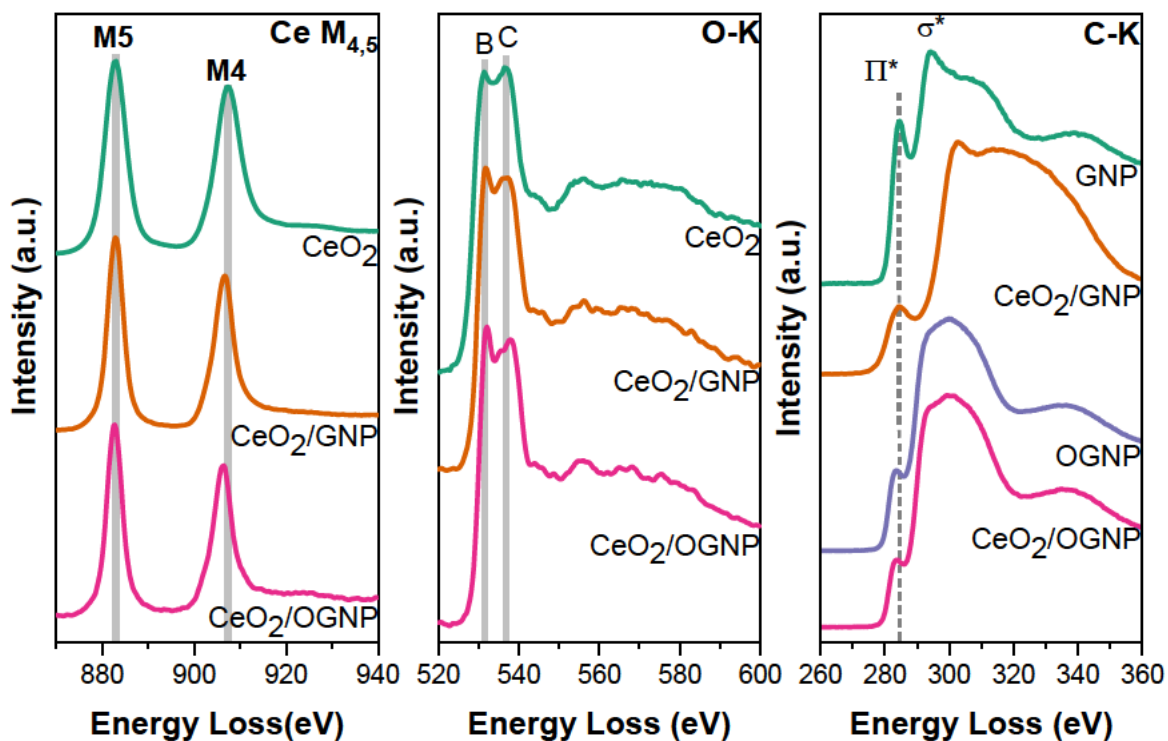
Figure 22. EELS spectra of CeO₂ and CeO₂/graphene and support (GNPs and OGNPs) samples: a) at the Ce-M4.5 edge; (b) at the O-K edge; (c) at the C-K edge

It has been possible to find information in the literature on the use of the EELS technique to infer the oxidation states of various metal oxides, such as uranium [71], yttrium [72], and cerium [73]. In the case of CeO_2, information on the oxidation states of Ce has been obtained from the spectra in the regions of the Ce-M5 and Ce-M4 edges, as well as the O-K edge [74].

In the spectra comprising the cerium-related region (Figure 5-a), the edges of Ce-M4 (901 eV), Ce-M5 (883 eV) can be seen. These result from electronic transitions from the 3d to the 4f state. Ce-M4 corresponds to the transition from the $3d_{3/2}$ state to the $4f_{5/2}$ state, while Ce-M5 is from the $3d_{5/2}$ state to $4f_{7/2}$ [75,76].

Some authors [74,77] have reported that materials with Ce^{4+} show signs towards greater energy loss at both edges. This behavior can be distinguished in the CeO_2 sample.

In addition to this, it is said that in oxides containing Ce with a fluorite-like structure, the relationship between the intensities of the M5 and M4 edges is directly proportional to the content of Ce^{3+} when there is a mixture of oxidation states (Ce^{4+} + Ce^{3+}) [74]. **Table 7** shows these data quantitatively. The I_{M5}/I_{M4} ratio tends to be higher for graphene-supported ceria samples, indicating higher Ce^{3+} content.

Table 7. Characteristics of the EELS spectra at the Ce-M4,5 edge of CeO_2 and CeO_2/graphene.

	Ce M5	Ce M4	
Sample	Energy Loss	Energy Loss	I_{M5}/I_{M4}
CeO_2	883.02	907.52	1.15
CeO_2/GNPs	882.85	906.85	1.25
CeO_2/OGNPs	882.74	906.44	1.27

It is important to consider that the contributions of Ce^{4+} ions stand out for bulk CeO_2, while CeO_2 in the form of nanoparticles usually presents higher contributions of Ce^{3+} [76]. In Turner's work [77] it was possible to verify by EELS that, in nanoparticles

with a diameter less than 5 nm, cerium is preferably in its reduced state, Ce^{3+}; while the proportion of Ce^{4+} increases as its size grows, the authors reported spectra of particles with a size of 30 nm that showed a combination of Ce^{3+} and Ce^{4+}, and 60 nm where Ce^{4+} predominated.

On the other hand, in stoichiometric CeO_2, that is, in its fully oxidized state, there are three absorption peaks at the O-K edge, located around 529, 531 and 536 eV (labeled as A, B and C), which are attributed to electronic transitions from the level of O 1s to the empty O 2p hole states, hybridized with cerium levels 4f, $5d-e_g$ and $5d-t_{2g}$, respectively [78].

Figure 22-b shows the spectra related to the oxygen present in the ceria of the materials analyzed in the region of the O-K edge. The absence of peak A is easily perceived, as an indication that the samples do not present the pure state of Ce^{4+}. The absence of hybridization between the states of Ce $4f^0$ and O 2p could arise from some structural changes and the formation of some Ce $4f^1$ instead of $4f^0$ [78]. The observation also coincides with the spectra reported by Xu and Wang [74], who attribute this "pre-edge" signal to oxygen bonding with Ce^{4+}.

Niu's work [79] showed that by introducing oxygen vacancies into CeO_2, the relative intensities of peaks A and C decrease, while that of peak B increases. Therefore, the remarkable increase in the intensity of peak B (about 532 eV) in the samples with the addition of graphene can be translated into an introduction of oxygen vacancies in the ceria.

Considering the previous explanations, the characteristics of the edges of Ce $M_{5,4}$ and O-K could indicate that there is probably a mixture of oxidation states (3+ / 4+) in all the studied materials, although in different proportions. In addition, it was found that there is an interaction between ceria and graphene such that it reduces its oxidation state, that is, it induced oxygen vacancies, leaving a material with a higher proportion of Ce^{3+}. This effect is even greater with the support of functionalized graphene, i.e. graphene oxide.

Finally, the modifications in the electronic structure of graphene were also studied by EELS. **Figure 22-c** presents the spectra at the C-K edge, of the support materials (GNPs and OGNPs) and of the composite materials (CeO_2/GNPs and CeO_2/OGNPs).

According to the literature [80,81], the spectra of graphitic materials (as well as graphene) at the C-K edge consist of a sharp peak π (about 284 eV) assigned to the transitions of carbon 1s to the anti-bond states π* of atoms with sp^3 hybridization. The second characteristic peak (found as σ or π+σ) occurs with greater intensity (about 290 eV for amorphous carbon and graphite). It is associated with transitions from level 1s to σ* orbitals for atoms with both sp^3 and sp^2 hybridization [82,83].

In the spectra of the C-K edge, it can be perceived that the intensities of the π* peak decrease with the deposition of CeO_2 in each type of support. According to Xu et al. [83], this would indicate that the oxygen content associated with graphene decreases in this sample. On the other hand, the more acute form in samples with GNPs indicates higher purity of graphene. The same authors explain this because when

oxygen is consumed, eventually the C atoms bound to sp^2 dominate, and the sample becomes increasingly graphitized, therefore, the sharpening of the EELS peaks indicates that crystallization improves. In the case of the samples studied, it could be that there is a decrease in oxygen when graphene interacts with CeO_2, due to the anchoring of this oxide in the functional groups of graphene.

In other publications [29,84] it has been mentioned that the displacement of the second signal at the C-K edge (σ*) towards greater energy loss is related to the number of graphene layers and that when the thickness exceeds 10 graphene sheets, the plasmon is assimilated to that of bulk graphite. In this sense, the displacement observed for the CeO_2/GNP sample related to the pristine support indicates an increase in graphene sheets, probably associated with the interaction of CeO_2 nanoparticles, which leads to the stacking of more graphene sheets. This characteristic in the modification of the structure of nanoplatelets (GNP) had already been previously appreciated by the XRD technique and EELS spectra confirm this interaction.

4.3. Remarks

In the obtained from CeO_2/graphene materials, it was possible to appreciate the dispersion and anchoring of the nanoparticles by SEM, which are more dispersed in the OGNPs support due to the presence of functional groups on the surface, that is, the interaction of oxygen vacancies in ceria with the functional groups of oxygen in graphene was confirmed. The CeO_2 content was estimated by XRD indicating that the synthesis method is suitable for preparing materials with different proportions of NPs.

The quantification of oxygen functional groups was carried out by the determination of acidic sites by the Boehm titration method, the results are representative to demonstrate possible interactions of the support. A difference in the availability of functional groups is shown with the addition of nanoparticles in the different types of supports, this could be associated with nanoparticle anchoring that occurs differently. Also, the change in the distribution of the groups and increase of the total of these in the synthesis and parallel deposition could have been by oxidation of the support caused by its interaction with the solvent (BD)

The EELS technique was useful to appreciate differences in the spectra of CeO_2 and CeO_2/graphene, some evidence was shown with which it can be inferred that ceria interacts with graphene in which the amount of Ce^{3+} increases. On the other hand, graphene presents structural changes with the addition of ceria nanoparticles, such as defects in the graphitic structure. Still, there is an increase in the number of sheets, due to a stacking induced by the interaction of Ce atoms.

5. Ni-Ce SYSTEM: SYNTHESIS AND CHARACTERIZATION

5.1. Materials and methods

5.1.1. Synthesis of Ni/CeO$_2$ materials

The synthesis of materials composed of Ni/CeO$_2$ was carried out by the method of polyol initiated by microwaves, adding at the beginning of reaction the precursor salt of cerium, $Ce(NH_4)_2(NO_3)_6$ (purity ≥98.5%, Sigma Aldrich) and 2 types of nickel precursor salts: Nickel nitrate (II) hexahydrate (purity ≥97.0% Sigma Aldrich) and nickel chloride (II) hexahydrate (purity ≥98% (Sigma-Aldrich). 2 types of polyols were also used as solvents: 1,4-butanediol (BD) and ethylene glycol (EG).

Unlike what was reported in the work of Komarneni et al. [85], who stated that the reaction is carried out at 200°C for 2 h, different reaction times were used in this work. The conditions used for each sample are summarized in **Table 8**.

Some of the samples (NiCe1, NiCe4, CeB, CeEG) were calcined at 400 °C for 3 h to ensure the evaporation of organic compounds and their thermal stability.

Table 8. Experiments for the synthesis of Ni/CeO$_2$.

Sample	Solvent	Ni Precursor	Synthesis time
NiCe1	BD	NiCl$_2$ · 6H$_2$O	40 min x 2
NiCe1-2 (rep.)	BD	NiCl$_2$ · 6H$_2$O	40 min x 2
NiCe1-3	BD	NiCl$_2$ · 6H$_2$O	40 min
NiCe1-4	BD	NiCl$_2$ · 6H$_2$O	20 min
NiCe1-5	BD	NiCl$_2$ · 6H$_2$O	10 min
NiCe2	EG	NiCl$_2$ · 6H$_2$O	40 min x 2
NiCe2-2 (rep.)	EG	NiCl$_2$ · 6H$_2$O	40 min x 2
NiCe2-3	EG	NiCl$_2$ · 6H$_2$O	40 min
NiCe2-4	EG	NiCl$_2$ · 6H$_2$O	20 min
NiCe2-5	EG	NiCl$_2$ · 6H$_2$O	10 min
NiCe3	BD	Ni(NO$_3$)$_2$ · 6H$_2$O	40 min x 2
NiCe3-2 (rep.)	BD	Ni(NO$_3$)$_2$ · 6H$_2$O	40 min x 2
NiCe3-3	BD	Ni(NO$_3$)$_2$ · 6H$_2$O	40 min
NiCe3-4	BD	Ni(NO$_3$)$_2$ · 6H$_2$O	20 min
NiCe3-5	BD	Ni(NO$_3$)$_2$ · 6H$_2$O	10 min
NiCe4	EG	Ni(NO$_3$)$_2$ · 6H$_2$O	40 min x 2
NiCe4-2 (rep.)	EG	Ni(NO$_3$)$_2$ · 6H$_2$O	40 min x 2
NiCe4-3	EG	Ni(NO$_3$)$_2$ · 6H$_2$O	40 min
NiCe4-4	EG	Ni(NO$_3$)$_2$ · 6H$_2$O	20 min
NiCe4-5	EG	Ni(NO$_3$)$_2$ · 6H$_2$O	10 min
CeB	BD	-	40 min x 2
CeEG	EG	-	40 min x 2

5.1.2. X-ray Diffraction (XRD)

XRD was used to characterize untreated materials to identify and quantify crystalline phases and estimate crystallite sizes. The SmartLab RIGAKU equipment was used in a 2θ interval from 10° to 90° and 0.01° steps.

5.1.3. Raman spectroscopy

It was performed in the inVia Basis Renishaw confocal Raman microscope with a laser radiation source with a wavelength of 532 nm to evaluate the presence and/or changes in the microstructure of metal oxides. Each powder sample was attached to a glass slide on double-sided tape.

5.1.4. Transmission electron microscopy (TEM)

TEM was performed in a TECNAI F30 Type FEG FEI microscope operated at 300 kV for HR-TEM imaging. The Z contrast mode was applied to differentiate the heavier elements from the samples. Under the same conditions, a semi-quantitative TEM-EDS elemental analysis was performed in different sample regions.

5.1.5. Fourier Transform Infrared Spectroscopy (FTIR)

The Nicolet iS10 equipment was used in the transmission mode to characterize the pristine supports. An amount less than 1mg of sample was diluted in 100 mg of KBr previously dried at 100 °C, the materials were ground to obtain a fine and homogeneous powder, which was pressed at 30 kN to obtain a wafer.

5.1.6. Scanning electron microscopy (SEM) and semi-quantitative elemental analysis (EDS)

The morphology of the materials was determined by SEM in the FEI Helios NanoLab 600i equipment with a double beam and a secondary electron detector operated at

5 kV. The same equipment and conditions were applied for semi-quantitative elemental analysis (SEM-EDS). The NiCe1 and NiCl$_2$ samples were attached to aluminum pins on carbon tape.

In the case of the Ni(NO$_3$)$_2$ and NiCe4 samples, they were mounted on copper grids to eliminate the charging effect.

Because some samples had electromagnetic charge, micrographs of the secondary electron detector (SE) could not be obtained, only images taken with the backscattered electron detector (BSE) are presented, while in other cases (Cu-grid samples) BSE and SE images were obtained.

5.2. RESULTS AND DISCUSSION

5.2.1. Evaluation of doping or deposition of Ni in Ni/CeO$_2$ materials

The samples obtained by simultaneously synthesizing CeO$_2$ and Ni by the microwave method, NiCe1, NiCe2, NiCe3 and NiCe4, and the repetition of these materials (NiCe1-2, NiCe2-2, NiCe3-2 and NiCe4-2), were analyzed by XRD to evaluate the phases, the possible doping with Ni and its reproducibility.

The samples were adjusted by Rietveld refinement to the phases shown in **Figure 23**, using the High Score Plus software and doing a search and match analysis against the Inorganic Crystal Structure Database (ICSD). The crystallographic parameters presented in **Table 9** were obtained.
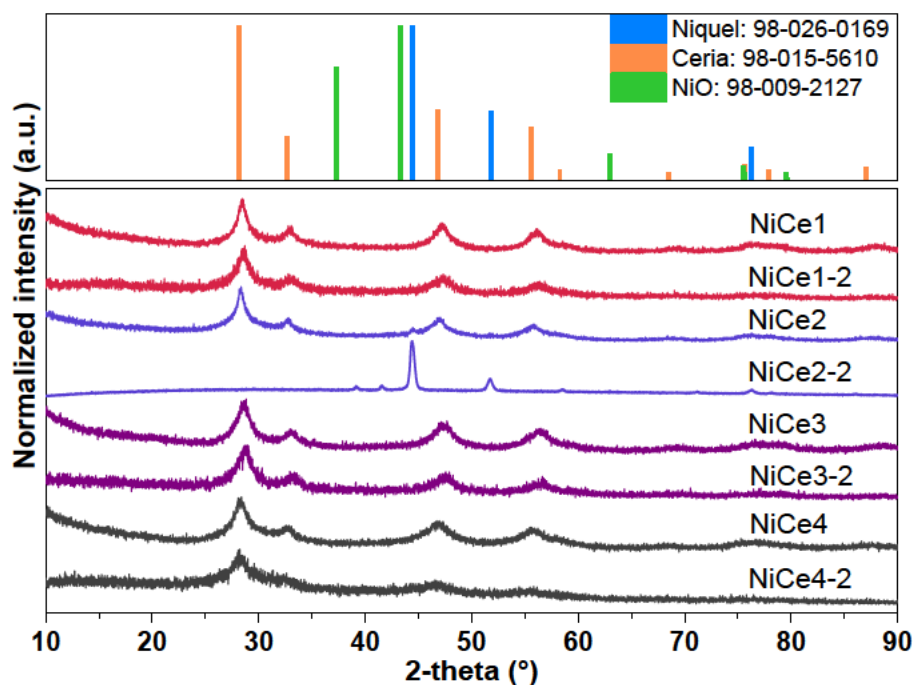
Figure 23. Diffractograms obtained from Ni/CeO$_2$ materials synthesized in 2 cycles of 40 min each.

Most of these materials have diffraction peaks corresponding to the cubic structure of ceria (cerianite). In the case of the NiCe2-2 sample, it shows signs of the crystalline phase of nickel, however, it is not reproducible since it is the repetition of NiCe2. On the other hand, diffractograms show broad peaks related to low crystallinity, assigned to the size of particles on the order of nanometers.

The samples were prepared to expect to obtain a nickel content of 10% by weight with respect to ceria, so a higher proportion of nickel in the samples is associated with a part of the cerium (due to its nanometric size) probably remaining in the solvent, decreasing its content in the sample.

Table 9. Results of XRD characterization of Ni/CeO₂ materials synthesized with 2 cycles of 40 min

Sample	Ni wt. %	NiO wt. %	CeO₂ wt. %	β Ceria (nm)	β Ni (nm)	a (Å)	Δa (Å)
NiCe1	21.7	0	78.3	3.7	1.8	5.446	-0.03
NiCe1-2	0	24.7	75.3	3.7	2.8	5.443	-0.03
NiCe2	25	0	75	3.0	2	5.477	-0.00
NiCe2-2	78% Ni	22% NiH	0		37.8	-	
NiCe3	33	0.8	66.2	3.5	1.9	5.429	-0.05
NiCe3-2	19.2		80.8	3.3	1.35	5.423	-0.05
NiCe4	6.2		93.8	2.6	1.4	5.481	0.00
NiCe4-2	8.3		91.7	2.1		5.499	0.02
CeB			100%	4.0		5.437	-0.04
CeEG			100%	3.6		5.542	0.06

β = crystallite size. Δa = change in Ceria lattice parameter from theoretical (5,479 Å), JCPDS: 98-015-5608.

In terms of the approach made to ceria doping and its analysis by XRD, this was assessed using Vegard's law, which, according to Cavendish [86], can be used to estimate the network parameter for solid solutions of one metal oxide in another. This law describes the linear relationship between the lattice parameter and the concentration of the solute.

For CeO₂, this relationship can be expressed as follows:

$$a = 5.479\text{Å} + \sum m_k (0.022\Delta r_k + 0.0015\Delta z_k)\,\text{Å} \qquad (14)$$

where a is the lattice parameter of the solid solution of ceria, Δr_k is the difference in ionic radii between the radius of the kth dopant and Ce^{4+} atoms in a coordination of eight (0.97 Å), Δz_k is the valence difference ($z_k - 4$), and m_k is the molar percentage of the dopant [87].

The CeO$_2$ lattice parameter is based on the JCPDS file: 98-015-5608. The value of the atomic radius for Ni^{2+} in an eight-fold coordination is estimated at 0.83 Å [87]. It is considered that the 10% molar nickel dopes the structure since it is reported in the literature that there is a solubility limit of ceria around 10%. [88]. Substituting these values, the expected network parameter value for a sample doped with 10% nickel was estimated at 5,425 Å.

The parameters calculated by refinement (**Table 9**), show that the values of the lattice parameter most similar to that expected for doped samples are those of the NiCe3 sample. However, from the diffraction of the ceria sample performed with the same type of solvent (CeB), a lower value (5.437Å) is obtained than the expected value (5.479Å). If this network parameter is used as the theoretical one, a network parameter of 5,383 Å would be expected for a 10% doped sample, which would mean that, if Vegard's law is met, the NiCe3 sample would not have Ni doping by substitution in CeO$_2$, or the doping is less than 10%.

 Figure 24 shows the Raman spectra of the different materials synthesized ceria (CeB and CeEG) and doped ceria (NiCe1, NiCe2, NiCe3 and NiCe4). Metal oxides with fluorite-like structures have a single Raman mode with F$_{2g}$ symmetry and can

be seen as a symmetrical expansion-contraction vibration mode of the oxygen atoms surrounding each cation. In CeO, the mode frequency is 465 cm^{-1} [89].

In the Raman spectra of doped ceria samples, a red-shift can be observed with respect to pure ceria samples. This could be due to the increase in topological disorder and the greater presence of defects [32].

In the range of 500-700 cm^{-1} the appearance of bands, usually associated with the introduction of defects, can be seen. This band was deconvoluted into 3 peaks for doped ceria materials.

The D1 band, located at ~590 cm^{-1}, can be observed in the Raman spectra of pure and doped ceria samples. This is attributed to the intrinsic vacancies of oxygen, that is, they are present in the structure of pure ceria. These vacancies are also associated with the presence of reduced Ce^{3+} cations [32].

The band ~620 cm^{-1} can be assigned to extrinsic oxygen vacancies, which result when Ce^{4+} ions are replaced with dopant ions (in this case Ni^{2+}), to maintain charge neutrality [90].

Regarding ceria doping, it has been reported [32] that the position of the D2 band depends on the doping element. Also, the D1 peak becomes more intense with the doping content, suggesting that, in this case, the addition of nickel causes an increase in the number of intrinsic and extrinsic defects.
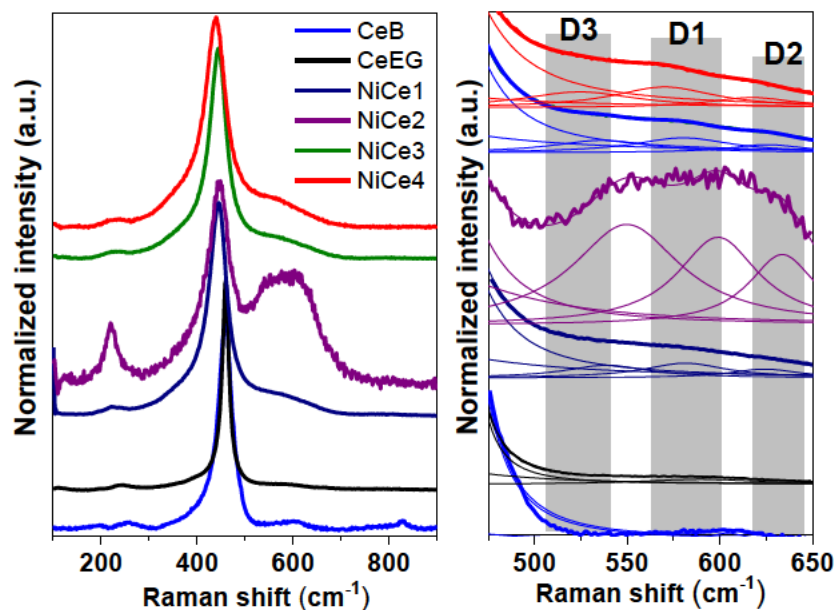
Figure 24. Raman spectra of ceria materials (CeB and CeEG) and doped ceria (NiCe1, NiCe2, NiCe3 and NiCe4).

The number of defects in the samples can be estimated employing the relationships between the intensities of the peaks D1, D2 or D3 and that of the F_{2g} band; These parameters (I_{D1}/I_{F2g}, I_{D2}/I_{F2g} and I_{D3}/I_{F2g}) are summarized in **Table 10,** together with their summation, I_D/I_{F2g}.

The data reported in **Table 10** confirm that the addition of nickel promotes the formation of defects. The greater abundance of defects in materials synthesized with ethylene glycol (NiCe2 and NiCe4), could be an effect of the interaction between the precursor salt of nickel and said solvent that promotes microstructural changes. However, in the case of NiCe2 material, a higher intensity of the D-band with respect to F_{2g} could be assigned to the presence of amorphous species, coming from intermediate species in the synthesis of nickel.

Table 10. Relationship of Raman intensities of ceria materials (CeB and CeEG) and doped ceria (NiCe1, NiCe2, NiCe3 and NiCe4)

Sample	I_{D1}/I_{F2g}	I_{D2}/I_{F2g}	I_{D3}/I_{F2g}	I_D/I_{F2g}
NiCe1	0.05	0.03	0.04	0.13
NiCe2	0.41	0.33	0.47	1.21
NiCe3	0.05	0.03	0.04	0.13
NiCe4	0.07	0.04	0.06	0.17
CeEG	0.02			0.02
CeB	0.02			0.02

5.2.2. Effect of synthesis time in Ni/CeO$_2$ materials

The effect of synthesis time (see **Table 11**) on the NiCe1 sample was evaluated by Raman spectroscopy. In these spectra (**Figure 25**) the characteristic bands of ceria F2g, D1, D2 and D3, described above, can be noticed.

Table 11. Synthesis time of the studied samples

Sample	Synthesis time
NiCe1-2	40 min x 2
NiCe1-3	40 min
NiCe1-4	20 min
NiCe1-5	10 min

As shown in **Figure 26**, the intensity ratios tend to increase as a function of the synthesis time, which would mean that defects are introduced in the crystal structure

of the ceria as the synthesis takes place. From this graph, it could also be deduced

that 40 min is enough reaction time for the synthesis of this material.
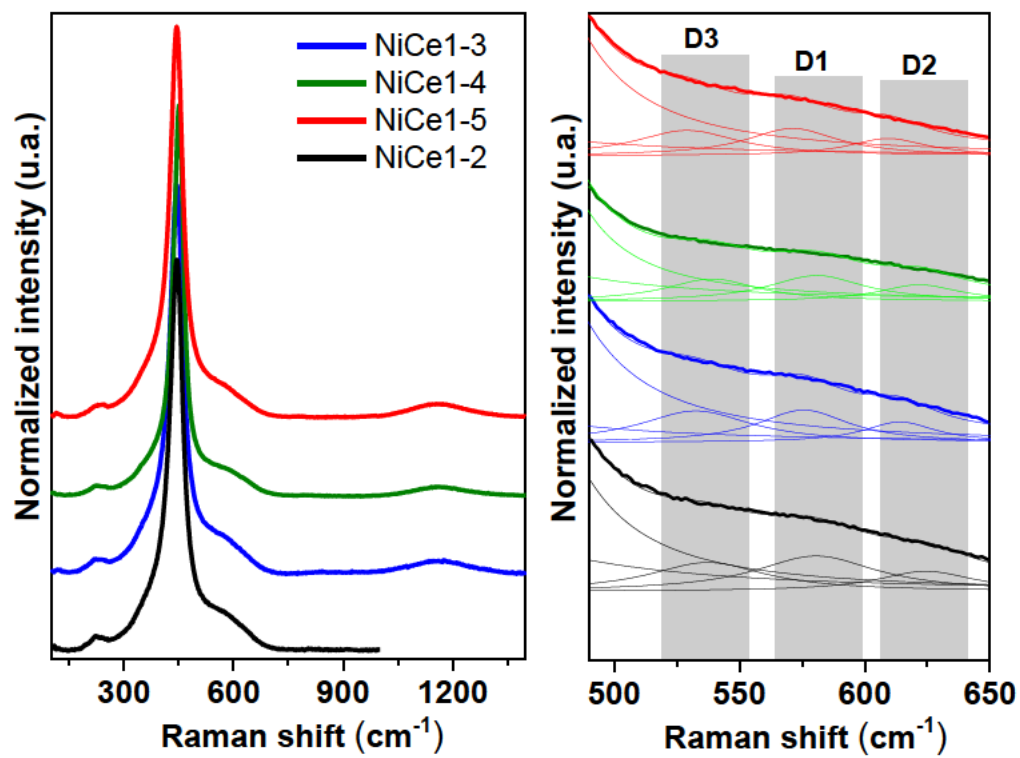
Figure 25. Raman spectra of NiCe1 material synthesized at different reaction times.
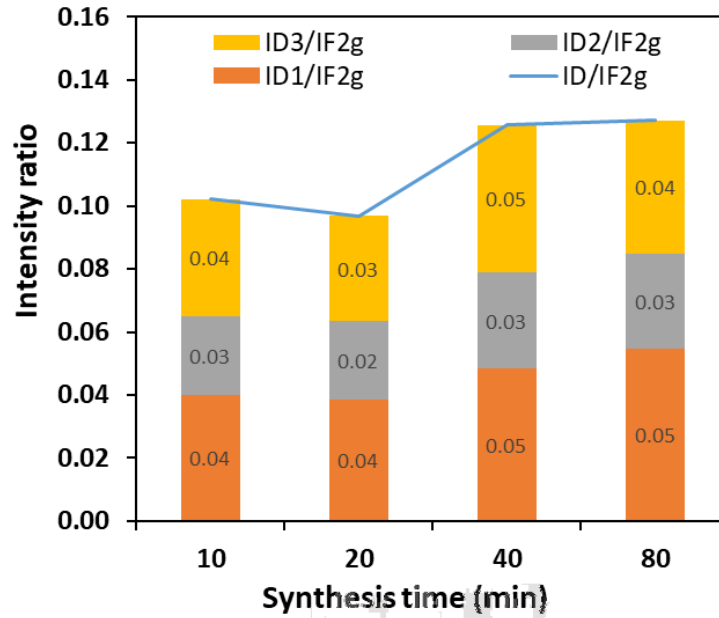
Figure 26. Raman intensity ratios as a function of synthesis time for the NiCe1 sample.

The samples CeB, NiCe1 and NiCe1-5 were analyzed by TEM to check changes in morphology due to the effect of the addition of dopant and synthesis time. In the CeB sample (**Figure 27**) agglomerated particles with uniform size and morphology (spheres with diameter around 3 nm) are observed.
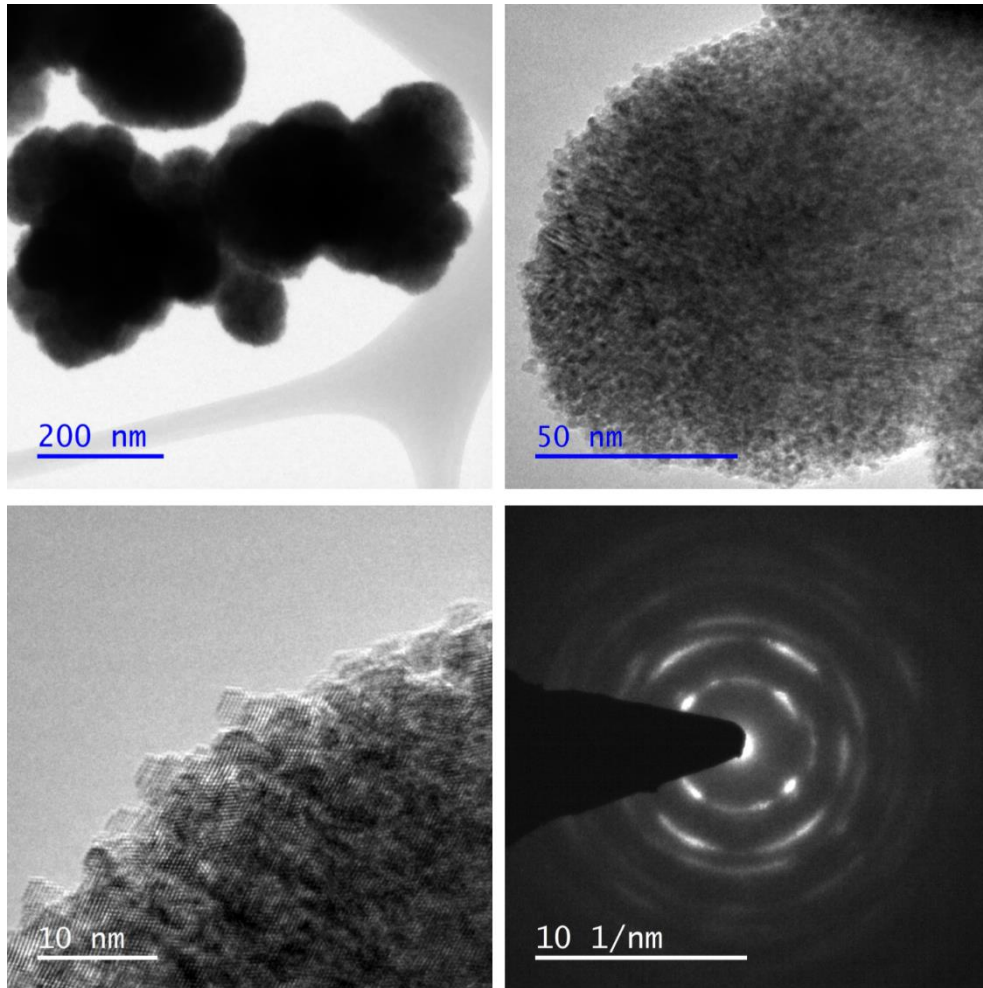
Figure 27. TEM micrographs and electron diffraction pattern of the CeB sample.
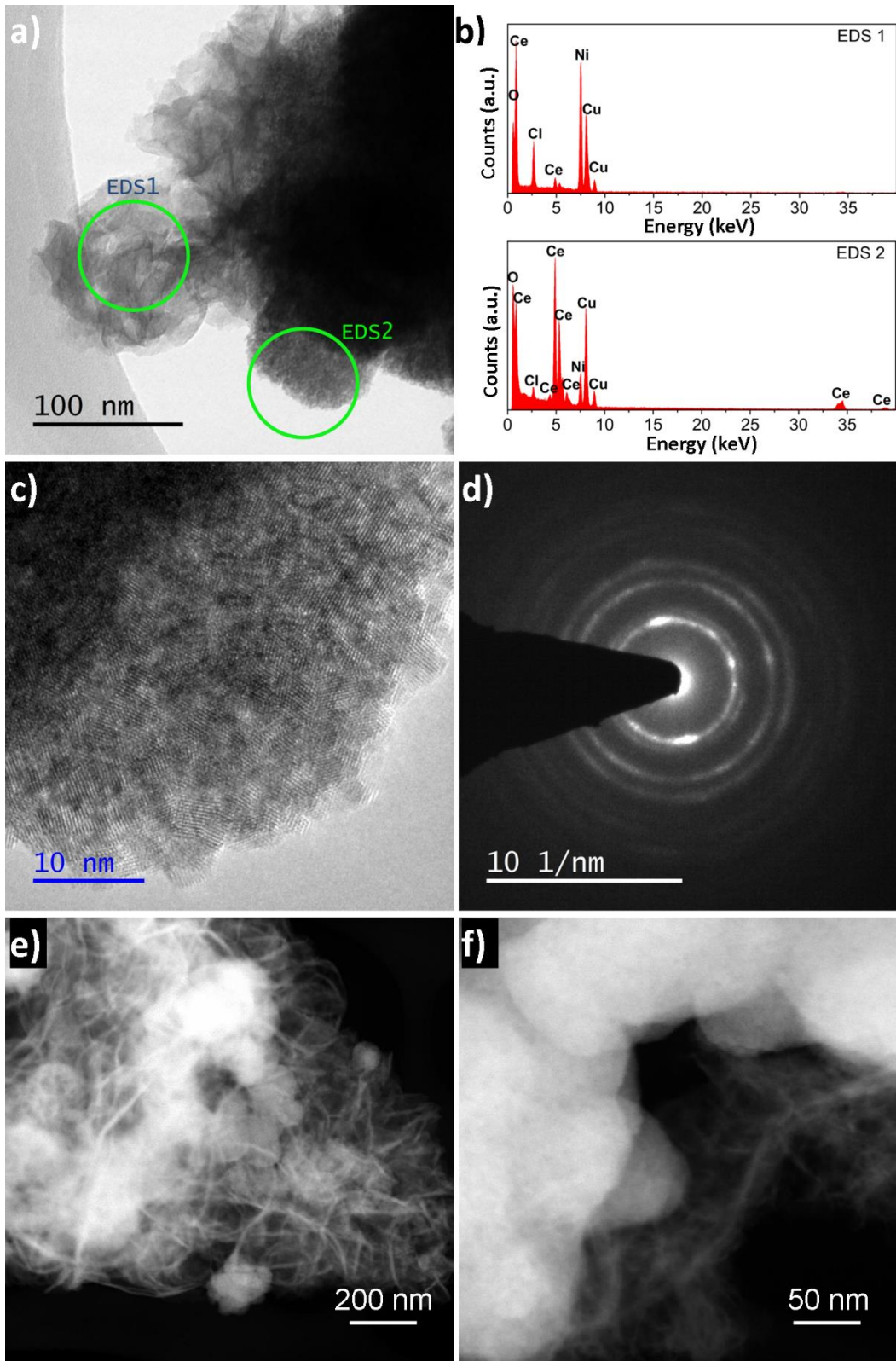
Figure 28. TEM analysis of the NiCe1 sample. (a) and (b): micrograph and its respective EDS. (c) and (d): HR-TEM micrograph and diffraction pattern. (e) and (f): micrographs in Z-contrast mode.

The micrographs of samples containing nickel, NiCe1 and NiCe1-5, in **Figures 28 and 29** show the spherical particles attributed to CeO_2. However, these are accompanied by a material in the form of sheets (similar to graphene sheets). These sheets are smooth in the sample NiCe1-5 (synthesized in 10 min), while for the sample NiCe1 (synthesized with 2 cycles of 40 min), they have some folds.

The EDS analysis applied to the different morphologies observed, confirms that the spherical particles contain cerium dioxide, however, there is also some nickel in the material, although it is unknown in what proportion.

As for the laminar structures, they contain nickel, although additionally they contain chlorine, which can be attributed to the precursor salt ($NiCl_2 \cdot 6H_2O$) although it is unknown if it is completely attributed to the salt that did not react, or if there is any part of the precursor that was reduced.
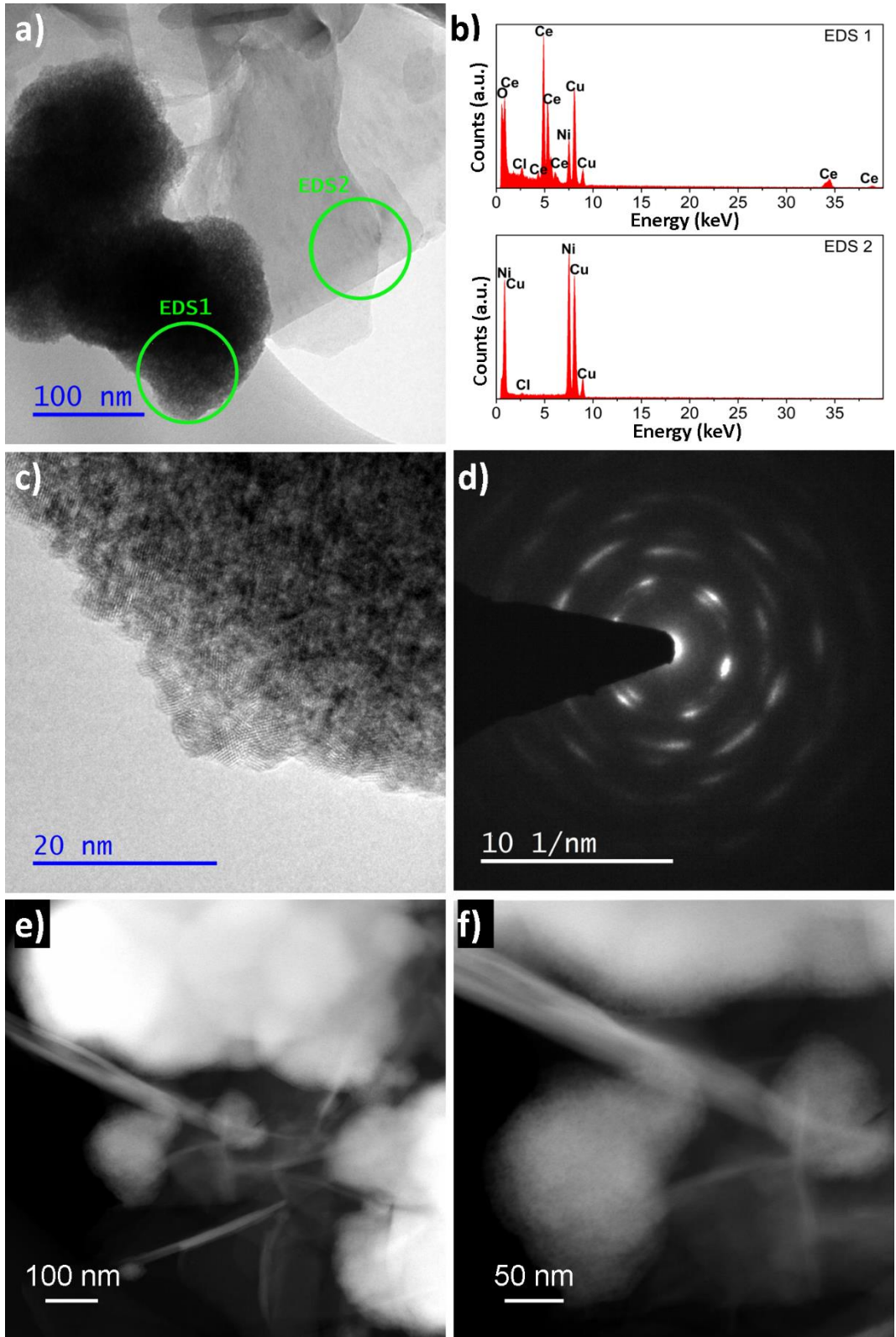
Figure 29. TEM analysis of the NiCe1-5 sample. A) and b): micrograph and their respective EDS. C) and d): HR-TEM micrograph and diffraction pattern. E) and (f): micrographs in Z-contrast mode.

Between nickel materials at different reaction times (NiCe1 and NiCe1-5), there is no significant difference in the size of the ceria particles. Still, in the morphology of the sheets containing nickel (best observed in the Z-contrast mode), in addition, the EDS of NiCe1-5 in these sheets does not present (or is relatively low) chlorine content.

Electron diffraction was applied in the areas with ceria particles, where a ring diffraction pattern was obtained (**Figures 27, 28-d and 29-d**), confirming the crystallinity of the materials. In areas with morphology attributed to nickel, electron diffraction was not possible since no crystalline zone was observed.

The interplanar distance of the CeB sample was calculated from the processing of the micrographs with the Digital Micrograph software, measuring in the strips of the lattice found in the crystalline grains. This was estimated at about 3.16 Å, while for XRD, the interplanar distance in the plane (111) is 3.12 Å. The similarity in these results could indicate that the sample is oriented preferably towards the plane (111) in the area where the analysis was performed.

Similarly, for the NiCe1-2 sample, the interplanar distance calculated from the obtained micrographs is 3.18 Å, while for XRD, the distance in the plane (111) is 3.12 Å.

Due to the presence of chlorine in the nickel-doped samples, these samples were calcined and analyzed by some characterization techniques, contrasting with the nickel precursor salts.

5.2.3. Effect of materials calcination

The Raman spectra of nickel/ceria samples before and after calcining are grouped by the type of precursor salt in **Figure 30**. In the case of those synthesized with NiCl$_2$, a slight shift (more noticeable for NiCe1) towards a higher wavenumber can be seen as a result of the calcination of the material. This is explained due to the expansion of the ceria crystal lattice due to the lack of Ce^{3+} ions [91].

In the case of NiCe2 material, a band around 220 cm^{-1} can be observed, both before and after calcination, which can be attributed to the presence of the nickel precursor.
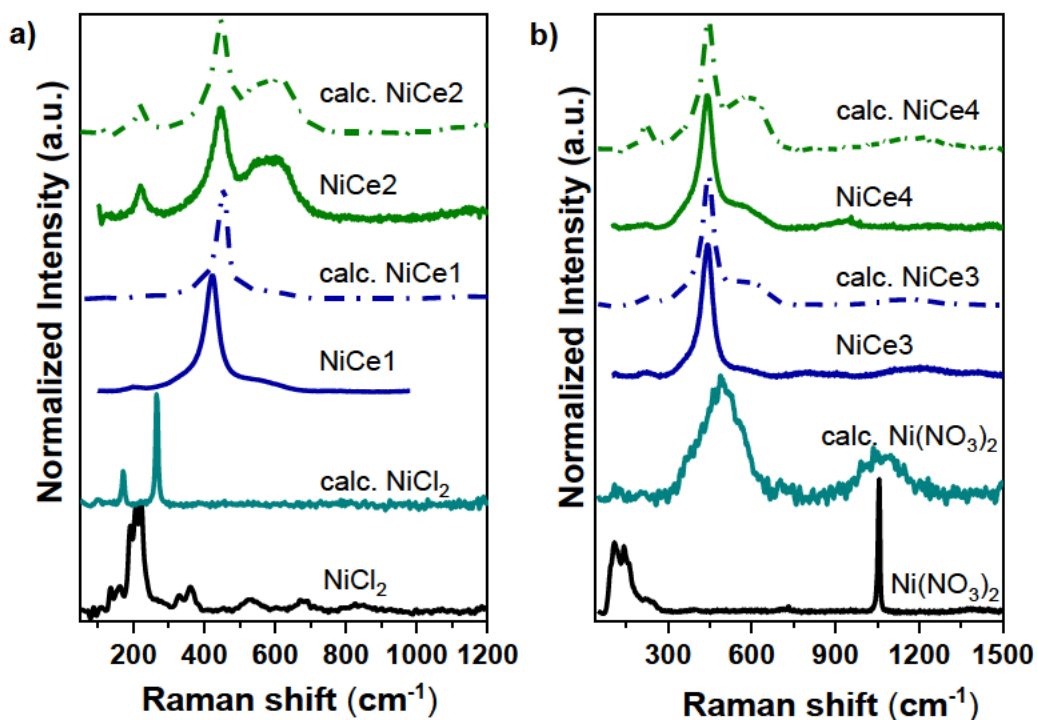
Figure 30. Raman spectra of materials before and after calcining, grouped by nickel precursor type: (a) NiCl$_2$, (b) Ni(NO$_3$)$_2$.

The Raman spectra corresponding to the precursor salt of nickel, $Ni(NO_3)_2$, is very similar to those published for aqueous nitrate solutions, with different metals [92]. Furthermore, there is a blue shift in the signals of materials synthesized with this precursor salt due to calcination in the materials. In the spectra of NiCe3 and NiCe4 after calcining, bands around 600 cm^{-1} are observed, which cannot be attributed entirely to the crystalline defects of the ceria. Still, they could be due to the presence of the precursor salt of nickel already calcined, or to the formation of intermediate species.

In a complementary sense, NiCe1 and NiCe4 samples were analyzed by FTIR before and after calcining. The spectra are shown in **Figure 31,** where these materials are contrasted with those of the precursor salts and the ceria material synthesized with the same solvent (that is, the material to which it would correspond without the addition of nickel).

Comparing the spectra shown in **Figure 31** suggests that materials containing Ni/CeO_2 have a very similar spectrum with those of ceria and do not present signals belonging to those of nickel precursors. A great similarity was found between these spectra and those obtained in the reference [67] used for the ceria synthesis method.
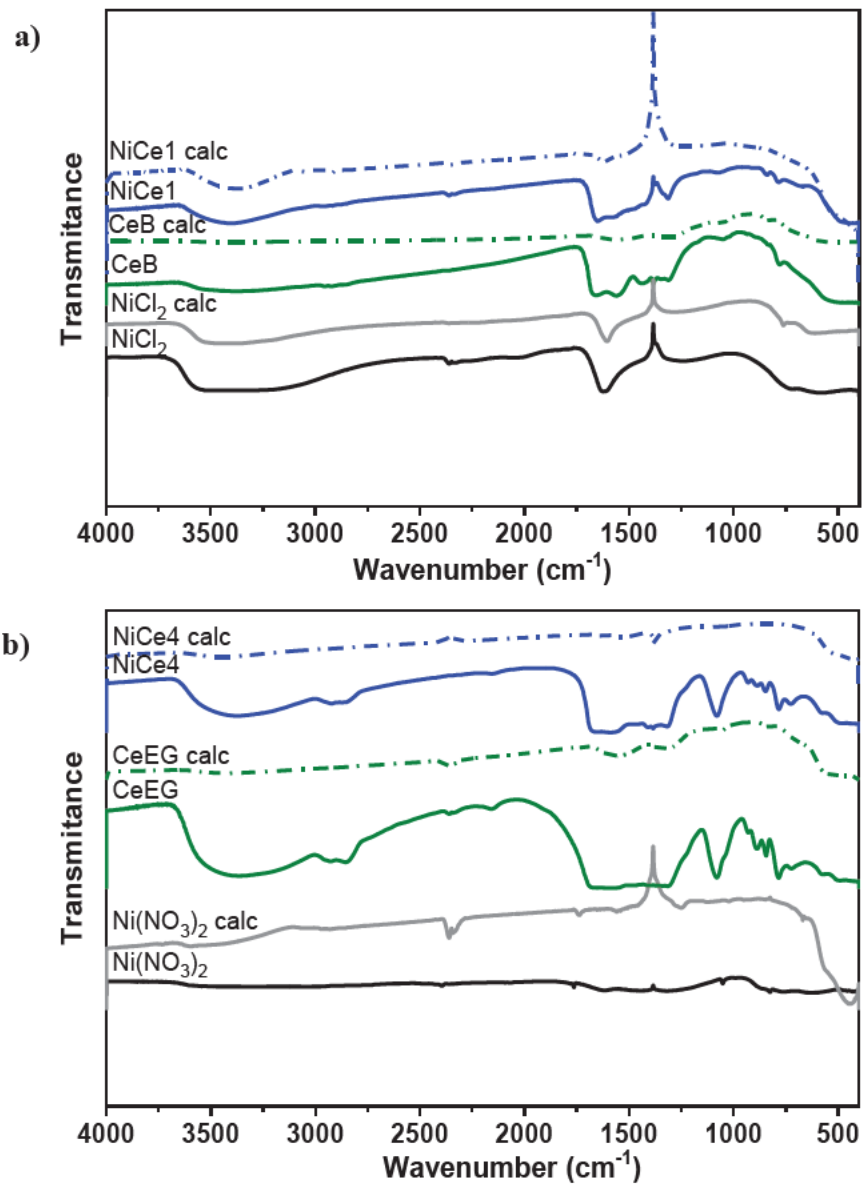
Figure 31. FTIR spectra of materials before and after calcining, grouped by nickel precursor type: (a) NiCl$_2$, (b) Ni(NO$_3$)$_2$.

The bands around 1440 and 780 cm^{-1} are assigned to N-O vibrations of ionic nitrate, just as the bands around 1300 and 1050 cm^{-1} have been assigned to the N-O vibrations of covalent nitrate. Another band at 1563 cm^{-1} has been assigned to

vibrations of the nitro group. All these bands are assigned to the precursor salt content of ceria remaining in the materials.

In general, these results indicate that the presence of these remaining organic species in the synthesized materials could be strongly decreased by calcination.

Continuing with the studies on the effect of the calcination of the materials, the materials NiCe1 and NiCe4 were studied by SEM, before and after calcination, contrasting them with the precursor salts of nickel.

Figures 32 and 33 show the micrographs of $NiCl_2$ and $Ni(NO_3)_2$, respectively. The change in the morphology of salts due to calcination is evident. In the case of $NiCl_2$, the material changes from rough plates to agglomerated spherical particles. On the other hand, $Ni(NO_3)_2$ passes from laminar structures to pyramidal particles. An important fact is that the particle size of $Ni(NO_3)_2$ is much smaller, which could favor the dispersion of nickel during synthesis. Another notable fact is that the EDS analysis for $NiCl_2$ shows a marginal change in composition before and after calcination, while for $Ni(NO_3)_2$ the nitrogen content decreases and the nickel content increases, probably due to loss of nitrates in the gas phase.

In micrographs of the NiCe1 sample (**Figure 34**), 2 kinds of morphologies are seen, following the observed by TEM analysis, this sample presented that of agglomerated particles, attributed to ceria (**Figure 28**); and the other comprised of sheets with folds, attributed to $NiCl_2$. In this case, due to the characteristics of the SEM analysis, the sheets with a shape similar to flowers were observed. After the calcination of the material, it was possible to see a change in this last morphology, obtaining a notable

reduction in the size of particles, accompanied by the formation of more folds. It should be mentioned that (as in the case of the pure NiCl₂) there was a marginal change in the semi-quantile composition analysis concerning the calcination of the sample.
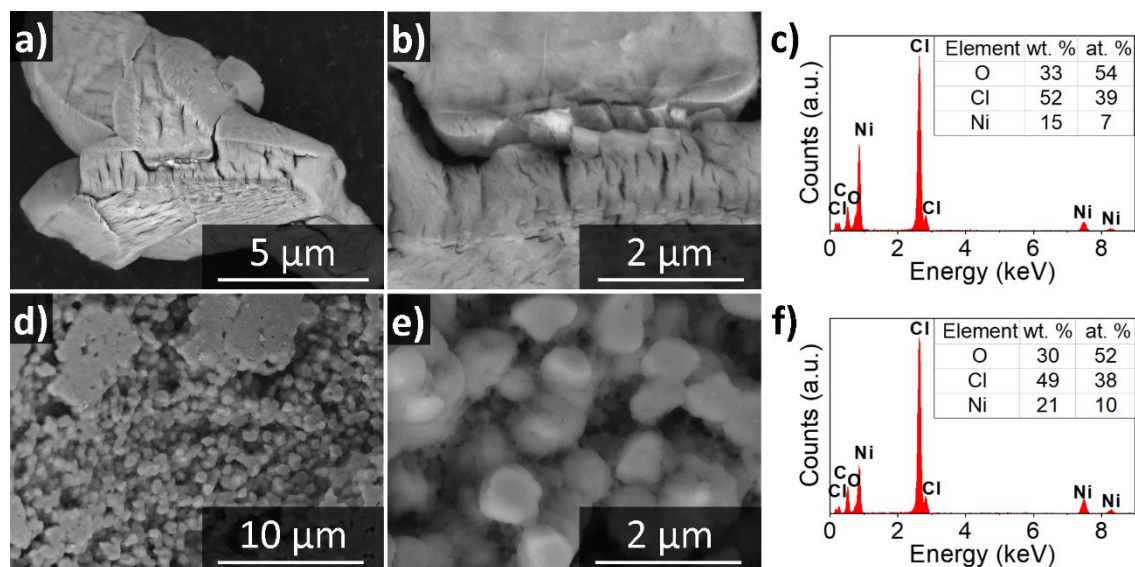
Figure 32. Scanning micrographs (BSE) and EDS of NiCl₂. (a, b, c): before calcination; (d, e, f): after calcination
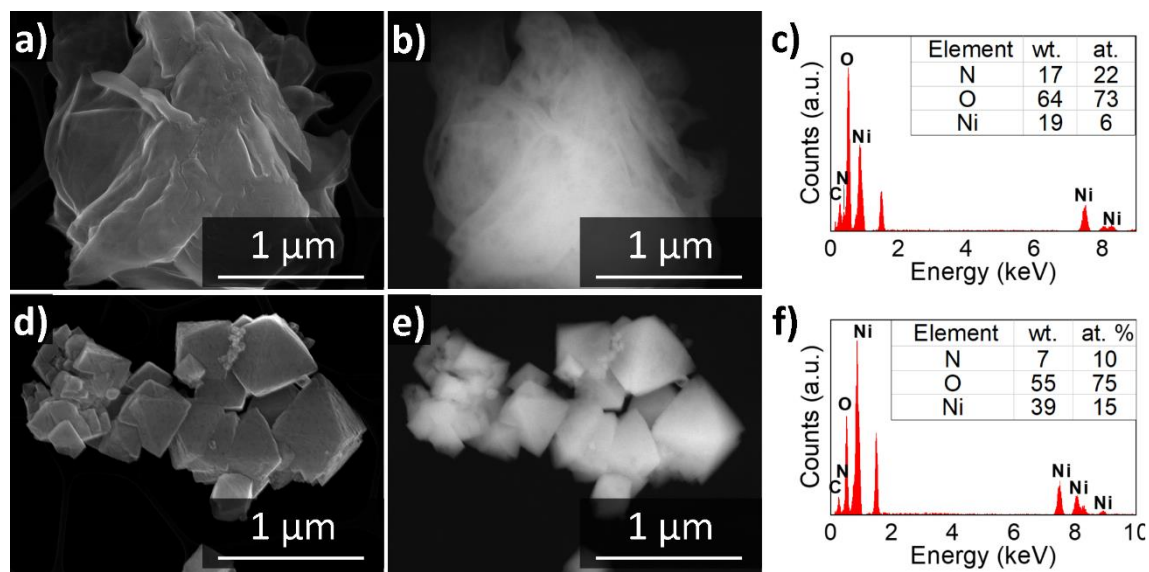
Figure 33. Scanning micrographs (ES and BSE) and EDS of Ni(NO₃)₂. (a, b, c): before calcination; (d, e, f): after calcination.
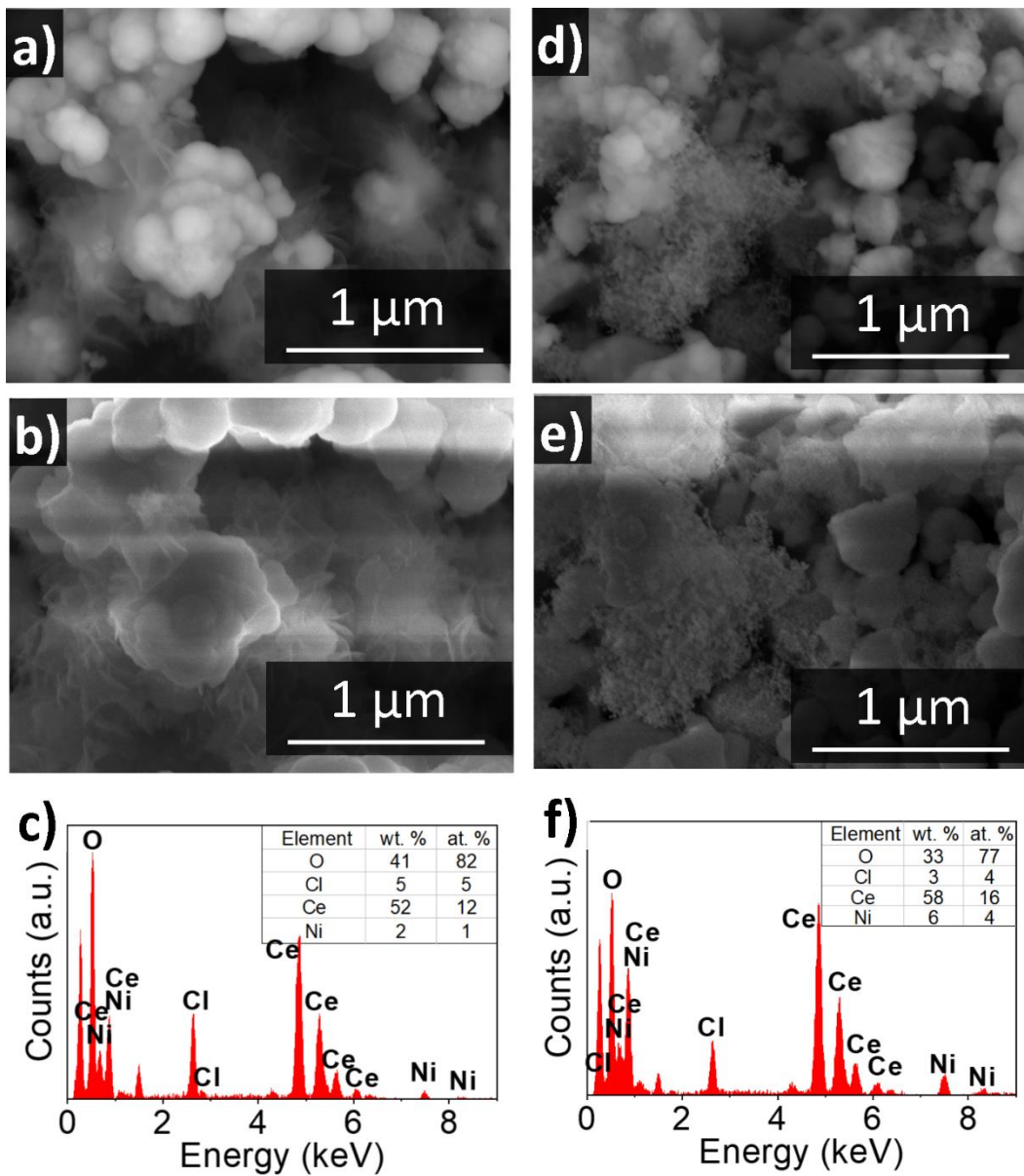
Figure 34. Scanning micrographs of the NiCe1 sample. (a, b, c) before calcination with a) BSE and b) EDS); (d, e, f): after calcination with a) BSE and b) EDS.
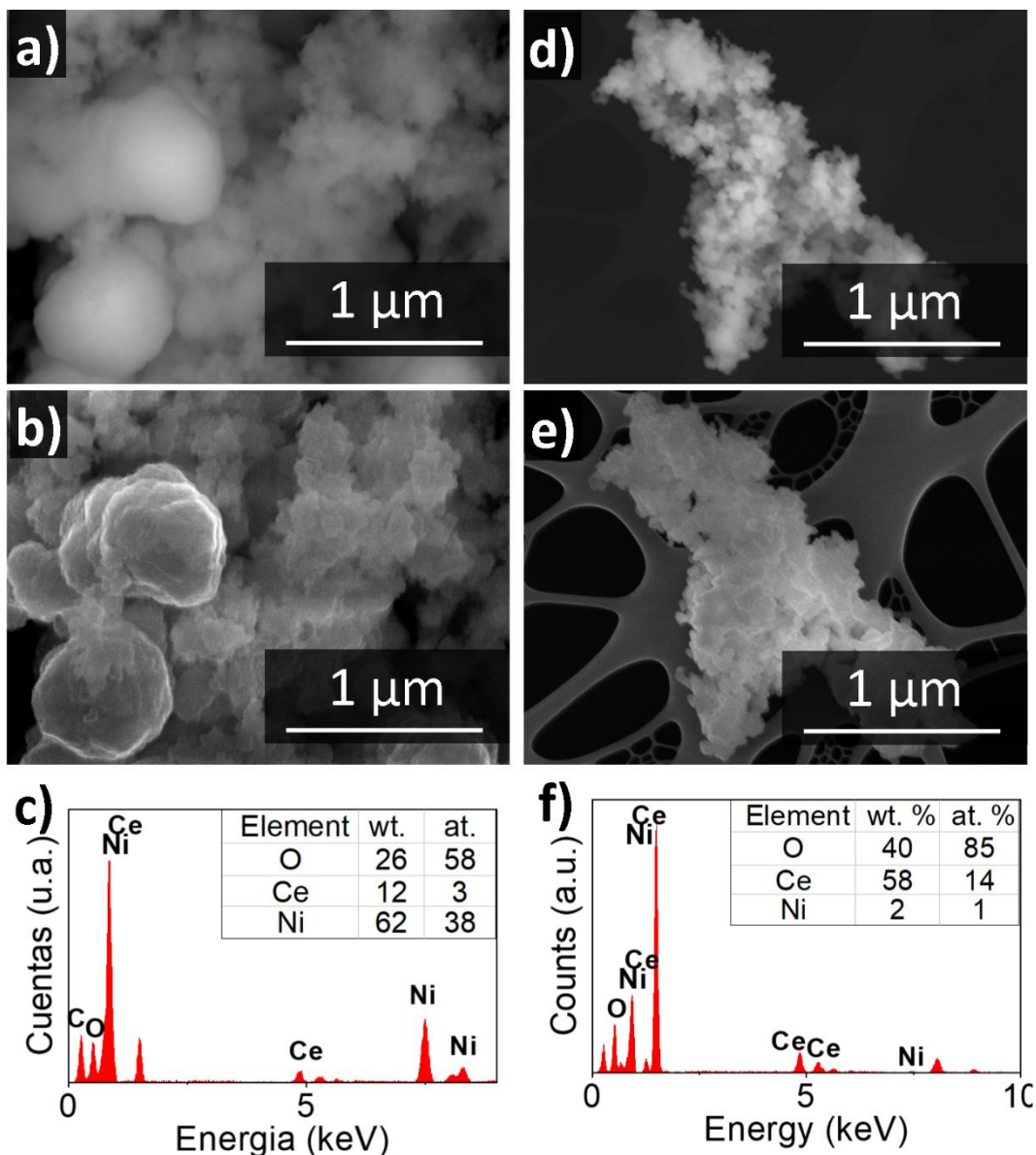
Figure 35. Scanning micrographs of the NiCe4 sample. (a, b, c) before calcination with a) BSE and b) EDS); (d, e, f): after calcination with a) BSE and b) EDS.

Figure 35 shows the scanning microscopy images obtained from the NiCe4 sample. In them, it can be seen, only a morphology of agglomerated spherical particles, again similar to those of ceria, although in this case some large particles (0.4-0.8 µm) are observed along with smaller ones (< 100 nm).

An EDS analysis (**Table 12**) was performed on areas where most of the particles grouped by size (large/small) were found. In these analyses, it was found that large particles have higher nickel content and almost zero cerium, so this morphology could be attributed to the nickel content in the sample, while small particles are attributed to CeO_2.

It is worth mentioning that in the overall EDS of the sample (**Figure 35-c**), low atomic percentages of ceria are observed, possibly because there was a higher nickel content in the area taken for analysis. However, it is important to note that in none of these analyses, nitrogen was found, which would imply the formation of Ni or NiO in the synthesis of the material.

Table 12. EDS results on large and small particles of the NiCe4 sample

	O at. %	Ce at. %	Ni at. %
Small particles	72	5	23
Large particles	53	1	46

5.3.   Remarks

It was possible to carry out the parallel synthesis of nanoparticles of NiO and CeO_2 and it was found that the addition of nickel in ceria increases its defect density, which could have a favorable impact on the catalytic activity of the materials.

It was also shown that calcination of materials is necessary to remove remaining precursors in materials. This can be seen most clearly with $Ni(NO_3)_2$, which would

mean that this salt decomposes at a lower temperature (The decomposition temperature to form NiO from this salt is around 250 °C [93]).

The effect of synthesis time was evaluated, showing that with 40 min of reaction almost the same density of defects is introduced into the microstructure of the ceria as with twice as much time.

6. SYNTHESIS AND CHARACTERIZATION OF *NiO-CeO2-graphene* COMPOSITES

6.1. MATERIALS AND METHODS

6.1.1. Synthesis of Ni-CeO2-graphene materials with different solvents

The carbon-based supports were commercially obtained from Graphene Supermarket in the form of graphene nanoplatelets (GNPs) with the specifications of average thickness lower than 3 nm (between 3-8 graphene monolayers) and 2-8 µm of lateral dimensions. OGNPs are oxygen-functionalized graphene nanoplatelets with a thickness of less than 50 nm and 0.3 to 5 µm of lateral dimensions.

The synthesis and deposition of NiO and CeO_2 nanoparticles was performed by the microwave-initiated polyol method [67]. The modification of the synthesis method consists of adding the carbon-based support materials at the beginning of the reaction, together with the other reagents, to obtain NiO and CeO_2 nanoparticles deposited on graphene material in a single process.

It was carried out on a Milestone ETHOS UP equipment at 200 °C for 40 min using ammonium nitrate and cerium (IV) (purity ≥98.5%, Sigma Aldrich) and nickel nitrate (II) hexahydrate (purity ≥97.0% Sigma Aldrich) as precursors. 1,4-butanediol (99%, Sigma Aldrich) and ethylene glycol (anhydrous, 99.8%, Sigma Aldrich) were used as solvents and reducing agents.

The samples were washed with ethanol and deionized water, and centrifuged until a translucent liquid was obtained. The solids were dried at 80 °C for 24 h and calcined at 400 °C for 3 h.

6.1.2.   Synthesis of Ni-CeO$_2$-graphene materials with different proportions of nanoparticles

Subsequently, the materials were synthesized with different concentrations using the same method and 1,4-butanediol as a solvent.

Table 13 presents the precursor/support ratios used to prepare NiO-CeO$_2$-graphene compounds with percentages of theoretical weights. The prepared samples were identified by the proportion of reagents used for preparation. For example, the nominated sample 1Ni5Ce5G started from 1 g of Ni precursor, 5 g of Ce precursor, and 5 g of graphene (marked G or GO depending on the type of carbon support).

Table 13. Experiments for the synthesis of Ni/CeO₂-graphene composites

Sample	Theoretical content (wt. %)		
	Graphene (C)	CeO$_2$	NiO
1Ce1G	76	24	0
1Ce2G	86	14	0
1Ce3G	91	9	0
1Ni5Ce5G	73	23	4
1Ni5Ce10G	85	13	2
1Ni5Ce15G	89	9	2
1Ce1GO	76	24	0
1Ce2GO	86	14	0
1Ce3GO	91	9	0
1Ni5Ce5GO	73	23	4
1Ni5Ce10GO	85	13	2
1Ni5Ce15GO	89	9	2

6.2. Characterization techniques

6.2.1. Scanning electron microscopy (SEM) and semi-quantitative elemental analysis (EDS).

The analysis was carried out on an FEI-QUANTA FEG-250 microscope with a voltage of 25 kV using a secondary electron detector and a backscattered electron detector. With the latter, elementary mappings were obtained. The samples were previously attached to aluminum pins on carbon tape.

6.2.2. X-ray diffraction (XRD).

X-ray analysis was performed using a Rigaku ULTIMA III X-ray diffractometer with Cu K-alpha radiation (λ= 1.540598 Å) as the X-ray source. The scans were done in the range of 10 to 90 de-grees of 2-theta using a 0.05-degree step and a counting time of 0.2 degrees per minute, operating at 40 kV and 44 mA to obtain the full diffractogram for each analyzed material. The samples were placed in a Rigaku zero background sample holder model 906163 (10mm x 0.2mm Well Si510) for their analysis. The data was processed with the Software PDXL from Rigaku and the crystalline domain sizes were calculated using the Scherrer equation as implemented in the PDXL software. The Crystallographic Open Database (COD) was used to identify the crystalline phases present in the samples.

6.2.3. Raman spectroscopy.

It was performed in the inVia Basis Renishaw confocal Raman microscope with a 532 nm laser radiation source to evaluate the presence and/or changes in the microstructure of metal oxides. Each powder sample was attached to a glass slide on double-sided tape.

6.2.4. Nitrogen physisorption.

The textural properties of the material were determined by N_2 physisorption. For this, the sample was de-gassed at 150 °C overnight under N_2 atmosphere. The pretreated sample then went through N_2 adsorption-desorption measurements at 77 K on a Micrometrics TriStar II analyzer. The Brunauer-Emmett- Teller (BET) method was used to calculate the surface area.

After the analysis, the data from adsorption isotherms was processed in the software SAIEUS to adjust the data to a model simulates with the non-localized density functional theory (NLDFT). The software used a 2D-NLDFT model for pores of infinite slit carbon materials, to calculate the pore size distribution. NLDFT is more accurate to study the actual microporous-mesoporous region while the commonly used method, Barrett-Joyner-Halenda (BJH), is suitable for the treatment of cylindrical pore models with a pore diameter larger than 5 nm [94].

6.2.5. Simultaneous thermal analysis TGA/DSC.

The thermal properties of the samples were evaluated in the ambient temperature range up to 700 °C under a flow of 100 ml/min of air (oxidative atmosphere), with a heating ramp of 10 °C/min.

6.2.6. Espectroscopía de emisión atómica de plasma acoplado (ICP-OES)

The contents of elemental metals (Ce and Ni) were determined by ICP. Prior to analysis, the samples were subjected to an acid digestion process. For this, 40 mg of the powder sample and 20 mL of an acid solution (HNO_3:H_2SO_4, 5:1) were deposited in a Teflon container and taken to microwave digestion (ETHOS UP, MILESTONE) with a heating ramp of 10°C/min until reaching 150°C and maintained for 40 min. The solution obtained was adjusted to 50 mL for subsequent analysis in the ICP team (Varian).

6.3. Results and discussion

6.3.1. Effect of the kind of solvent used in the synthesis of the sample 1Ni5Ce5G.

6.3.1.1. Morphology and semi-quantitative elemental analysis

Figures **36 and 37** show the micrographs obtained with different magnifications for the sample 1Ni5Ce5G synthesized with 1,4-butanediol (BD) and ethylene glycol (EG) as solvents and reducing agents. Although the resolution of the team limited the analysis in a certain way, a backscattered electron detector (BSD) was used thus areas with contrast differences were seen, attributed to the presence of metallic nanoparticles in the carbonaceous support, due to their greater atomic weight.
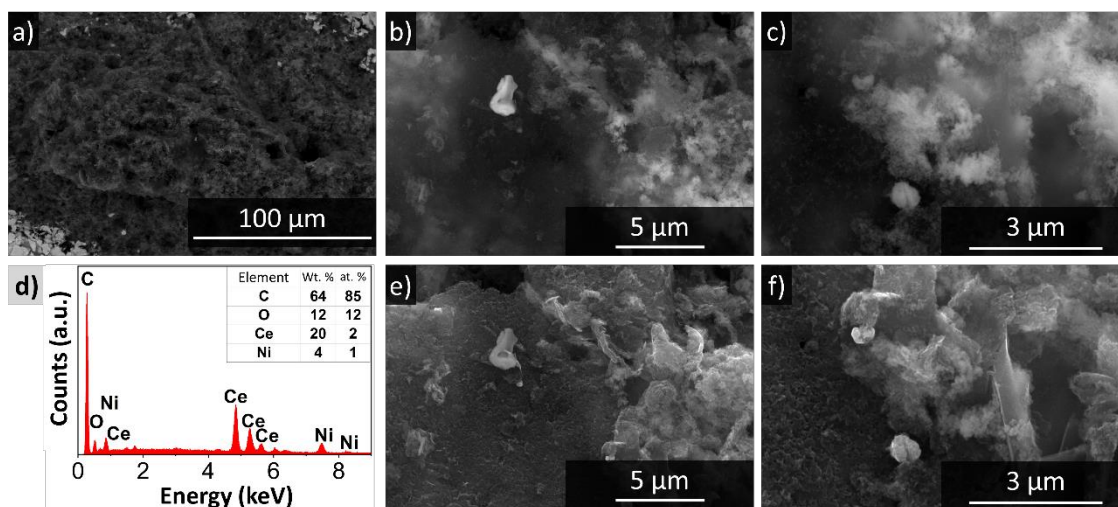
Figure 36. Scanning micrographs at 1000X, 10000X and 25000X of the sample 1Ni5Ce5G-BD (synthesized with BD) with BSD (a, b. c) and SE detector (e and f). (d) Semi-quantitative elemental analysis.
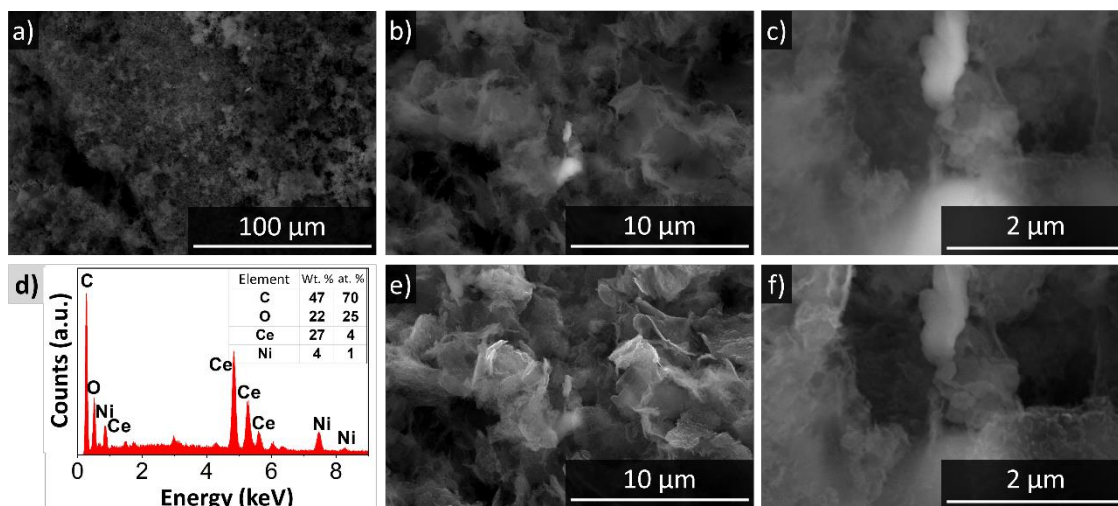
Figure 37. Scanning micrographs at 1000X, 10000X and 25000X of the sample 1Ni5Ce5G-EG (synthesized with ethylene glycol). Images with BSD (a, b. c) and SE detector (e and f). (d) Semi-quantitative elemental analysis.

That way, for both samples (1Ni5Ce5G-BD and 1Ni5Ce5G-EG) it was possible to distinguish the presence of particles deposited in the graphene, which gives a granulated texture to the flakes. This morphology is similar to that observed in CeO_2/graphene materials (chapter 4).

Only in the sample synthesized from BD particles with different morphology were distinguished. Those particles are spherical with a diameter of around 50 nm addition, they have a rough texture and were found less frequently, so they are related to the disposition of nickel agglomerations in some areas of the sample.

Concerning elemental analysis, the percentages by weight obtained in the material 1Ni5Ce5G-BD are very similar to those expected (73% C, 5% O, 19% Ce, and 3% Ni) However, in the sample 1Ni5Ce5G-EG concentrations of Ce and O increase, while that of C decreases. This could be associated with the partially transforming carbon support to produce CO_2 by oxidation. These differences in materials imply

an interaction between the carbonaceous support and ethylene glycol that promotes the oxidation of the latter.

Figures **38 and 39** show the elementary mappings made on the samples synthesized with different solvents. The images corresponding to the sample 1Ni5Ce5G-BD confirm that the spherical shaped-50 nm particles correspond to nickel and that there is also oxygen in the area, so these particles are comprised of nickel oxide (NiO). It is worth mentioning that both Ni and Ce appear widely dispersed on the surface of the material.

In the case of the mapping of the 1Ni5Ce5G-EG sample, it was not possible to see any contrast that could be associated with the nickel particles. This could indicate both that the nickel is well dispersed in the material, with a very small size; or, as well, the operating parameters of the instrument in which the mapping was carried out were not adequate.
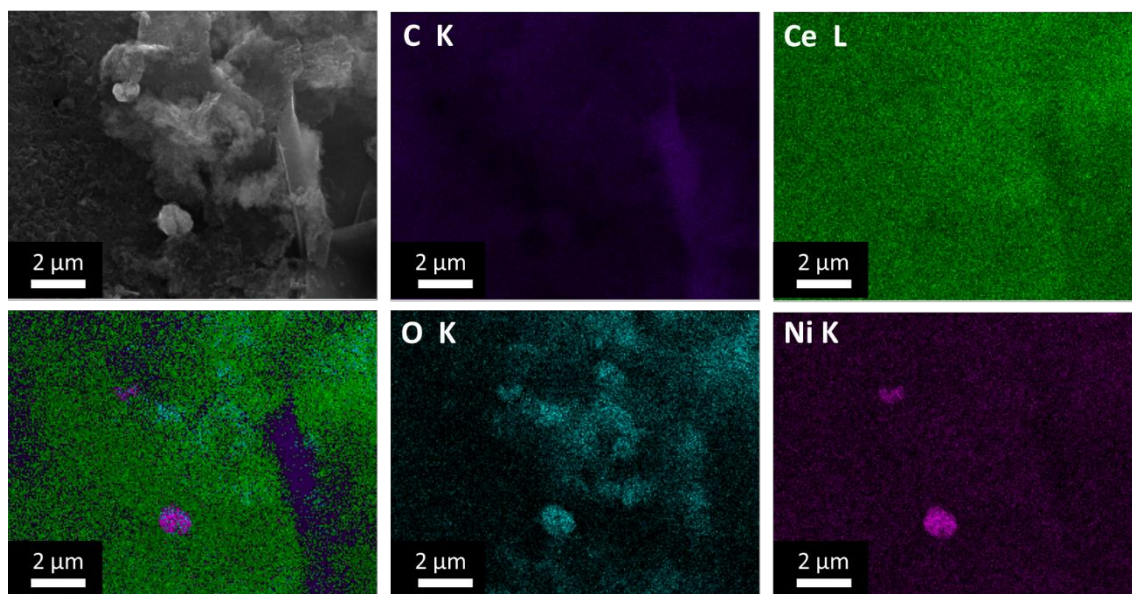
Figure 38. Elemental mapping of the 1Ni5Ce5G-BD sample. Initial micrograph (BSD), element mappings and elemental superposition.
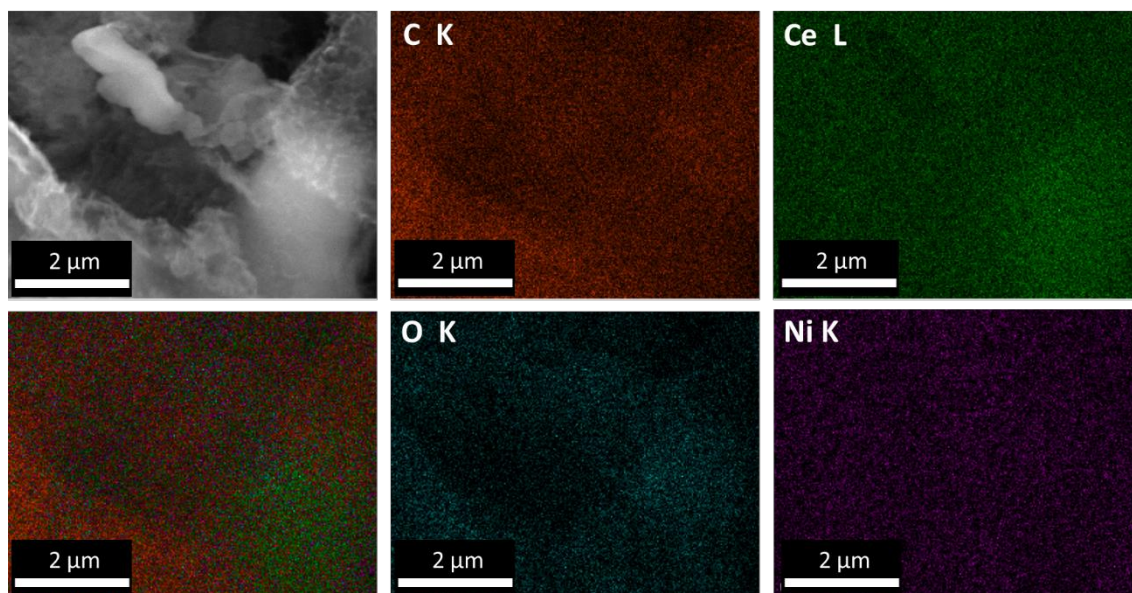
Figure 39. Elemental mapping of the 1Ni5Ce5G-EG sample. Initial micrograph (BSD), element mappings and elemental superposition.

6.3.1.2. Structural properties

Raman spectroscopy was used to characterize Ni-CeO$_2$-graphene materials with the solvents used (BD and EG) and to identify and compare their microstructure. The obtained spectra are shown in **Figure 40**.

The full spectrum image (measured from 100 to 2800 cm^{-1}) shows the characteristic signals for CeO$_2$ and graphite (graphene) phases. Firstly, in these spectra, the intensities of the bands suggest that the CeO$_2$ content is higher than that of carbon. However, the strong intensity of the CeO$_2$ bands is because CeO$_2$ is located on the surface of the material and is where the laser has been focused with the Raman microscope. However, due to its low content, no signal that could be related to nickel (Ni or NiO) was observed. A comparison of the materials synthesized with different solvents was made according to each phase (CeO$_2$ and graphene), in terms of identifying defects introduction that could be associated with anchoring, deposition, or doping related to nickel.

The characteristic vibration mode of pure CeO$_2$ occurs around 460 cm^{-1} [95]. In the spectra presented in **Figure 40-b**, there is a blue shift from this theoretical value, which is greater in the material synthesized with butanediol. According to the literature [32], this feature is related to disorder and the introduction of defects in the microstructure.
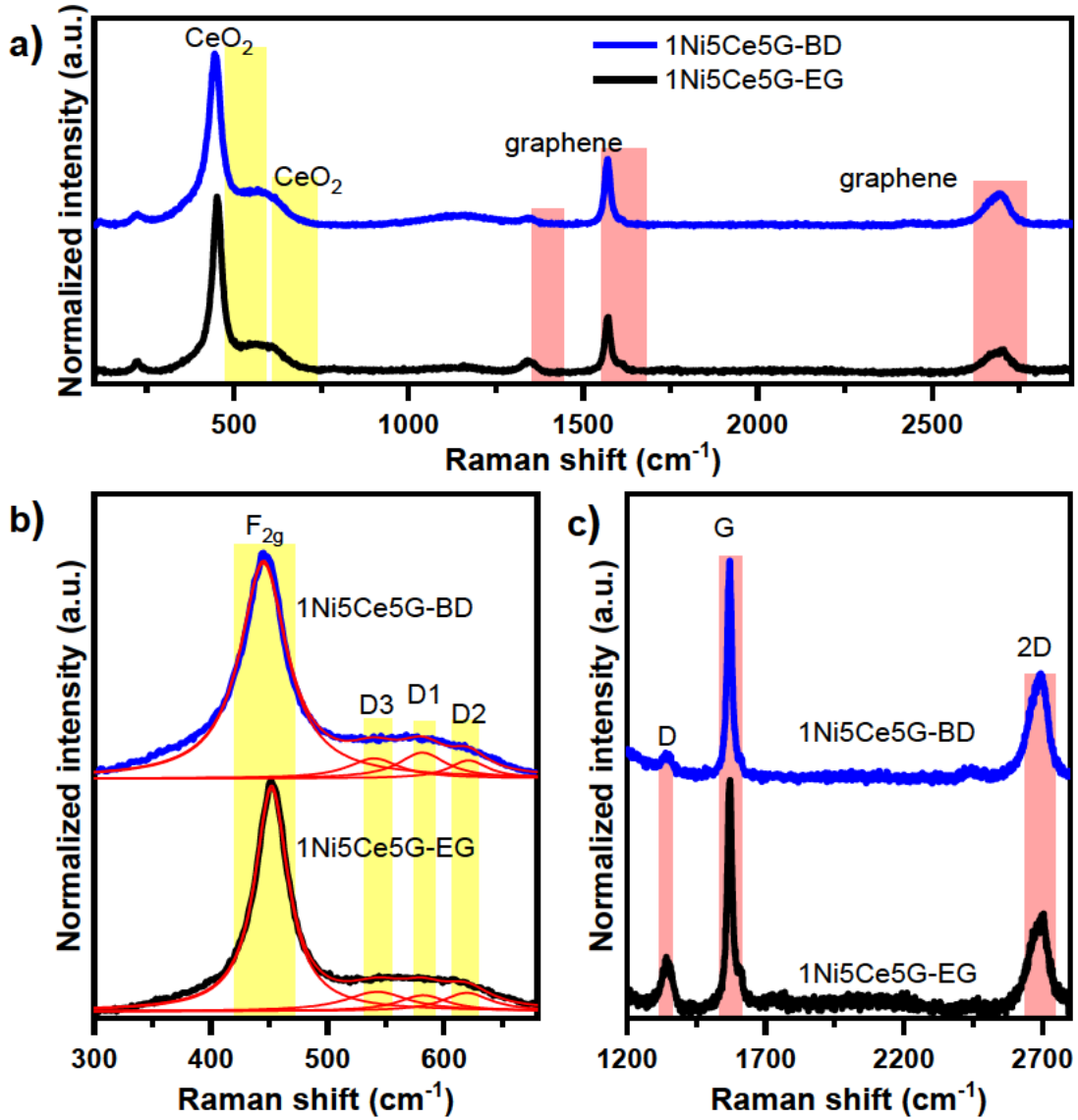
Figure 40. Raman spectra of samples 1Ni5Ce5G-BD and 1Ni5Ce5G-EG. a) general, b) CeO_2 signals, c) graphene signals

The introduction of defects in CeO_2 could be confirmed by the appearance of bands in the region of 500 to 700 cm^{-1}. This zone was deconvoluted into 3 bands, usually called D1, D2, and D3. The D1 band, located around 580 cm^{-1}, is related to oxygen vacancies which, being intrinsic, are also characteristic of pure CeO_2 [32]. Bands D2 and D3 are related to the presence of dopants. The first is due to the oxygen

stretching vibration between the Ce^{4+} ions and the dopant metal [96], due to which its position depends on the dopant element [32]. Finally, the D3 band is related to extrinsic oxygen vacancies, generated either by the presence of Ce^{3+} or by the presence of another cation [32,96].

The concentration of structural defects could be estimated by means of the ratio of intensities, I_D/I_{F2G}, where ID, is the sum of the intensities of the bands D1, D2 and D3. This value (see **Table 14**) is higher in the material synthesized with butanediol, which indicates that this solvent promotes the synthesis of a material with a greater number of defects. As is well known, defects, such as oxygen vacancies, provide greater catalytic activity to CeO_2, as they are linked to its ability to reduce [31,97].

In a complementary way, the characteristic bands in graphene were analyzed (**Figure 40-c**). The spectra exhibited mainly 3 signals characteristic of graphene. The D-band is induced by disorder or defects or the presence of carbon with sp^3 hybridization and its intensity is inversely proportional to the crystallite size. The G-band is the band of graphitic carbon as it originates from the C-C vibrations in the sp^2 carbon. The 2D band is interrelated with the band structure of graphene layers [98].

 Table 14 shows the data obtained from the Raman spectra of the samples 1Ni5Ce5G-BD and 1Ni5Ce5G-EG. The features of the support (GNPs), previously characterized, have been included. Based on the characteristics of the G-band, it can be deduced that there is an increase in crystallite size with the addition of nanoparticles to the support. The ratio of intensities, I_D/I_G, is lower in the material

97

with butanediol, which confirms that there is more graphitic carbon or increased crystallite size. As for the 2G band, it presents very few changes between materials, however, the I_{2D}/I_G ratio is slightly higher in the 1Ni5Ce5G-BD sample, which translates into a greater number of graphene sheets and therefore greater ordering [99].

Table 14. Parameters obtained by Raman spectroscopy of 1Ni5Ce5G materials synthesized with butanediol and ethylene glycol. Comparison with support (GNPs).

	Ceria		Graphene							
Sample	F_{2g} Band centroid (cm^{-1})	I_D/I_{F2g}	D Band		G Band		2D Band		I_D/I_G	I_{2D}/I_G
			Centroid (cm^{-1})	FWHM (cm^{-1})	Centroid (cm^{-1})	FWHM (cm^{-1})	Centroid (cm^{-1})	FWHM (cm^{-1})		
1Ni5Ce5G-BD	445	0.30	1339	11	1571	20	2694	77	0.06	0.49
1Ni5Ce5G-EG	452	0.24	1342	41	1573	20	2705	74	0.22	0.42
GNPs			1355	98	1579	35	2702	75	0.30	0.36

In summary, the observations made by Raman indicate the material synthesized with BD, has more crystalline defects in CeO_2 such as oxygen vacancies and carbon ordering, increasing its crystallite size. This also confirms BD's great capacity to anchorage the NPs to the graphene support. All this indicates a greater presence of nickel nanoparticles and a stronger interaction between nickel nanoparticles with ceria and with the support.

6.3.2. Characterization of Ni-CeO$_2$-graphene materials with different proportions of nanoparticles

Crystalline-structural analysis by XRD

The diffractograms of the samples supported in GNP and OGNP are presented in **Figure 41**, grouped by the kind of support and showing an increase in the region of NiO signals for samples containing this phase. Using the open crystallographic database, COD, profiles were identified with the crystalline phases of graphite (PDF No. 9000046), the cubic structure of CeO$_2$, cerianite (PDF No. 9009008) and NiO, bunsenite (No. 908693).

The quantification of phases by the RIR method and other crystallographic parameters obtained with the PDXL software are summarized in **Table 15**. In general, a tendency to increase the crystallite size of the graphite phase can be observed with the addition of nanoparticles, even more with NiO, indicating the effective deposition of nanoparticles between graphene layers.

This can be confirmed by the displacement at higher diffraction angles observed with the content of metal oxide NPs. This also happens with graphene oxide (OGNPs).
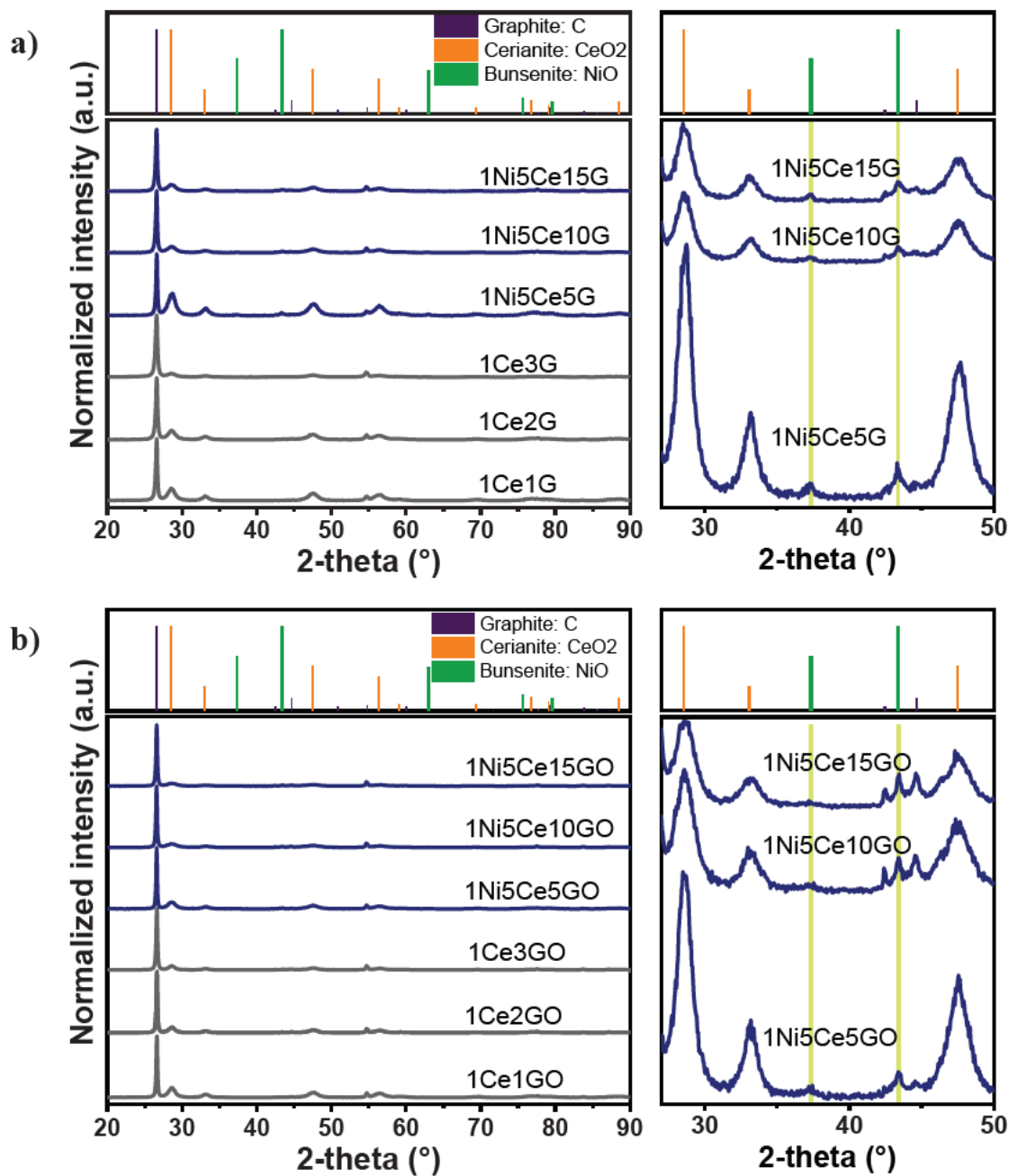
Figure 41. X-ray diffractograms of samples supported by: a) GNPs, b) OGNPs.

Table 15. Crystallographic parameters of Ni-CeO$_2$ samples supported in GNP and OGNPs.

Sample	Theoretical content (wt. %)			Content by XRD (wt. %)			Crystallite size (Å)			2θ (Higher intensity)		
	C	CeO$_2$	NiO	C	CeO$_2$	NiO	C	CeO$_2$	NiO	C	CeO$_2$	NiO
1Ce1G	76	24		89	11		327	78		26.58	28.61	
1Ce2G	86	14		91	9		320	74		26.58	28.60	
1Ce3G	91	9		97	3		269	73		26.58	28.67	
1Ni5Ce5G	73	23	4	76	20	4	379	74	98	26.59	28.64	43.34
1Ni5Ce10G	85	13	2	93	7	1	337	68	37	26.57	28.67	43.47
1Ni5Ce15G	89	9	2	92	7	1	393	67	207	26.54	28.57	43.38
1Ce1GO	76	24		90	10		461	84		26.61	28.62	
1Ce2GO	86	14		95	5		502	87		26.62	28.71	
1Ce3GO	91	9		96	4		432	84		26.62	28.67	
1Ni5Ce5GO	73	23	4	84	10	6	527	71	136	26.58	28.62	43.32
1Ni5Ce10GO	85	13	2	92	6	2	481	57	18	26.57	28.66	43.45
1Ni5Ce15GO	89	9	2	94	4	1	436	59	287	26.59	28.72	43.37

Microstructure analysis by Raman spectroscopy

Raman spectroscopy was used as part of the structural characterization of Ni-CeO$_2$-graphene materials in different proportions, identifying and comparing their microstructure. The spectra obtained are shown in **Figure 42**.

In the first place, in these spectra, the absence of bands assigned to the structure of Ni or Ce, or these signals are in the noise level. This is attributed to measuring the samples, focusing the laser mostly on the graphene material.
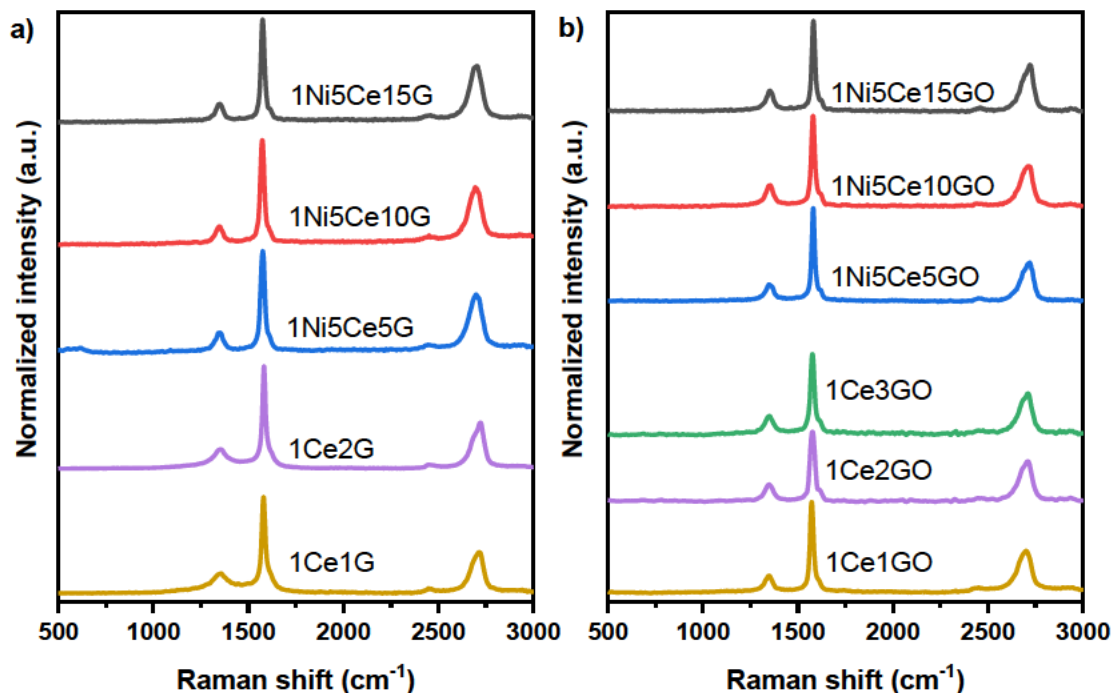
Figure 42. Raman spectra of samples of: a) NiO-CeO$_2$/GNPs, a) NiO-CeO$_2$/OGNPs

As for the distinguishable signals in the spectrum, all these correspond to the characteristic bands of graphitic materials. The D-band (~1350 cm^{-1}), is induced by disorder or defects or the presence of carbon with sp^3 hybridization, whose intensity is inversely proportional to crystallite size. The G-band (~1580 cm^{-1}) indicates graphitic carbon, which originates from C-C vibrations in the sp^2 carbon. The 2D band (~2700 cm^{-1}) is interrelated with the band structure of graphene layers [98].

 Table 16 shows the data obtained from the Raman spectra of the nanoparticle samples supported by GNPs and OGNPs. A blueshift in the D-band can be seen

with the deposition of nanoparticles on carbon carriers, this is associated with doping of materials since there is a change in the vibrational frequency [100].

Table 16. Parameters obtained from Raman spectroscopy analysis of samples.

Sample	D band		G band		2D band		Ratio of intensities	
	Centroid (cm^{-1})	FWHM (cm^{-1})	Centroid (cm^{-1})	FWHM (cm^{-1})	Centroid (cm^{-1})	FWHM (cm^{-1})	I_D/I_G	I_{2D}/I_G
1Ce1G	1440	432	1581	27	2704	89	0.17	0.49
1Ce2G	1439	422	1583	24	2709	87	0.14	0.49
1Ni5Ce5G	1347	73	1576	32	2695	89	0.18	0.54
1Ni5Ce10G	1347	65	1574	30	2693	85	0.16	0.51
1Ni5Ce15G	1348	60	1576	28	2696	87	0.17	0.55
1Ce1GO	1346	73	1573	28	2692	103	0.17	0.46
1Ce2GO	1348	66	1577	34	2698	89	0.23	0.55
1Ce3GO	1349	79	1577	33	2697	91	0.21	0.52
1Ni5Ce5GO	1351	81	1581	25	2706	86	0.17	0.44
1Ni5Ce10GO	1350	74	1580	29	2702	89	0.22	0.47
1Ni5Ce15GO	1352	68	1582	26	2708	83	0.21	0.52

The doping of the samples or the interaction of the nanoparticles in the support can also be appreciated by the intensity relationships. **Figure 43** shows the change in intensity ratios regarding adding metal oxide nanoparticles in the samples.

An aspect to consider is that the ratio of intensities, I_D/I_G, tends to increase with the addition of nanoparticles in samples with GNPs, this is due to an increase in the number of defects in graphene.

Contrary, in samples with OGNPs the ratio of intensities I_D/I_G, presents a decrease with the addition of metal oxides, this translates into an increase in graphitic carbon, probably due to an interaction such that nanoparticles promote some ordering in

graphene, increasing its crystallite size. Although less noticeable, this trend also occurs with the I2D/IG ratio. In addition, doping of graphene has been reported to reduce the intensity of the 2D band [99]. **Figure 43-b** confirms that there is a reduction in the intensity of this band with the introduction of metal oxide nanoparticles, some part of the metal oxides could be doping the OGNPs.
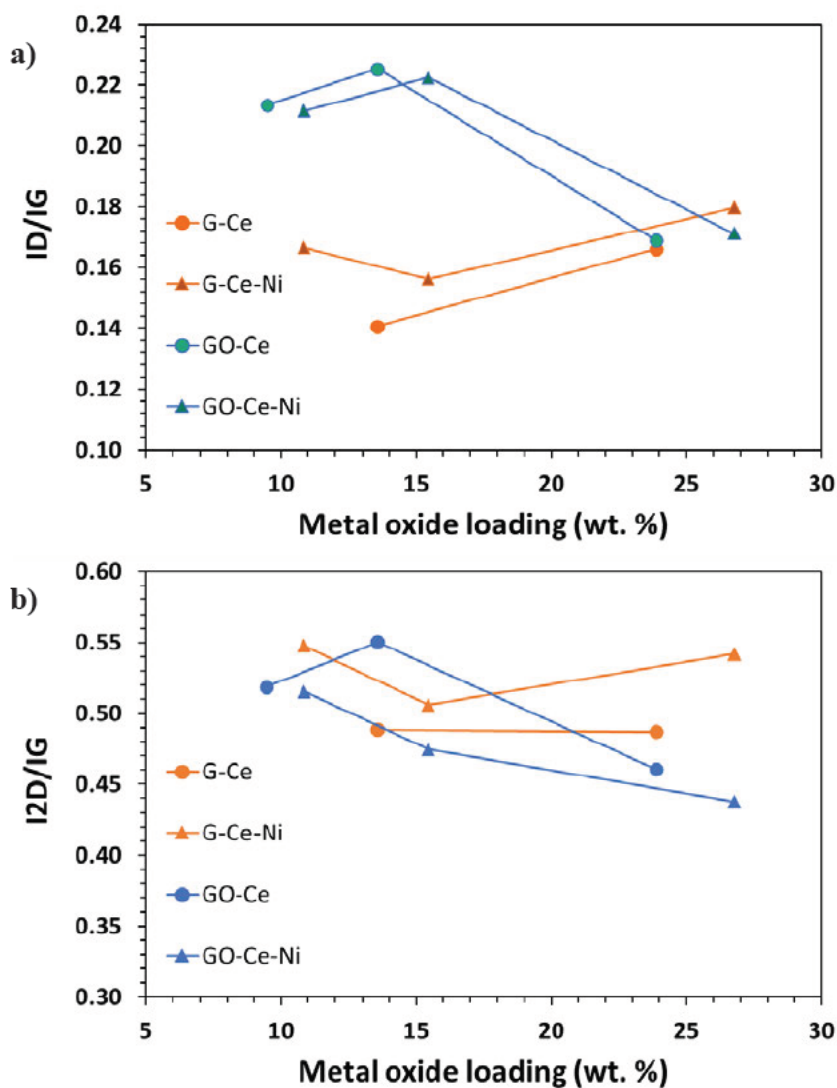
Figure 43. Raman intensity ratios as a function of metal oxide content.

Surface Area and PSD by N_2 Physisorption

The N_2 physisorption at 77K was carried out over all the composite materials samples, although, **Figure 44** only presents adsorption-desorption isotherms of Ce1G, 1Ce1GO, 1Ni5Ce5G, and 1Ni5Ce5GO for brief, since practically the same behavior was observed among the samples. In such isotherms, unrestricted monolayer-multilayer adsorption can be noticed. This isotherm is typical of nonporous or macroporous adsorbents since there is no saturation plateau near $P/P_0 = 1$, corresponding to Type II isotherm according to the IUPAC classification [101]. It is possible to appreciate the rapid increase of adsorbed amount at ultra-low pressure (P/P_0 from 0 to 0.06) due to adsorbent-adsorbent interactions in ultramicropores (of molecular dimensions), which results in the filling of micropores at very low P/P0 [102], as well as a hysteresis loop associated with capillary condensation, type H3, which is a typical behavior given by non-rigid aggregates of plate-like particles but also by macroporous materials which are not saturated.[101]
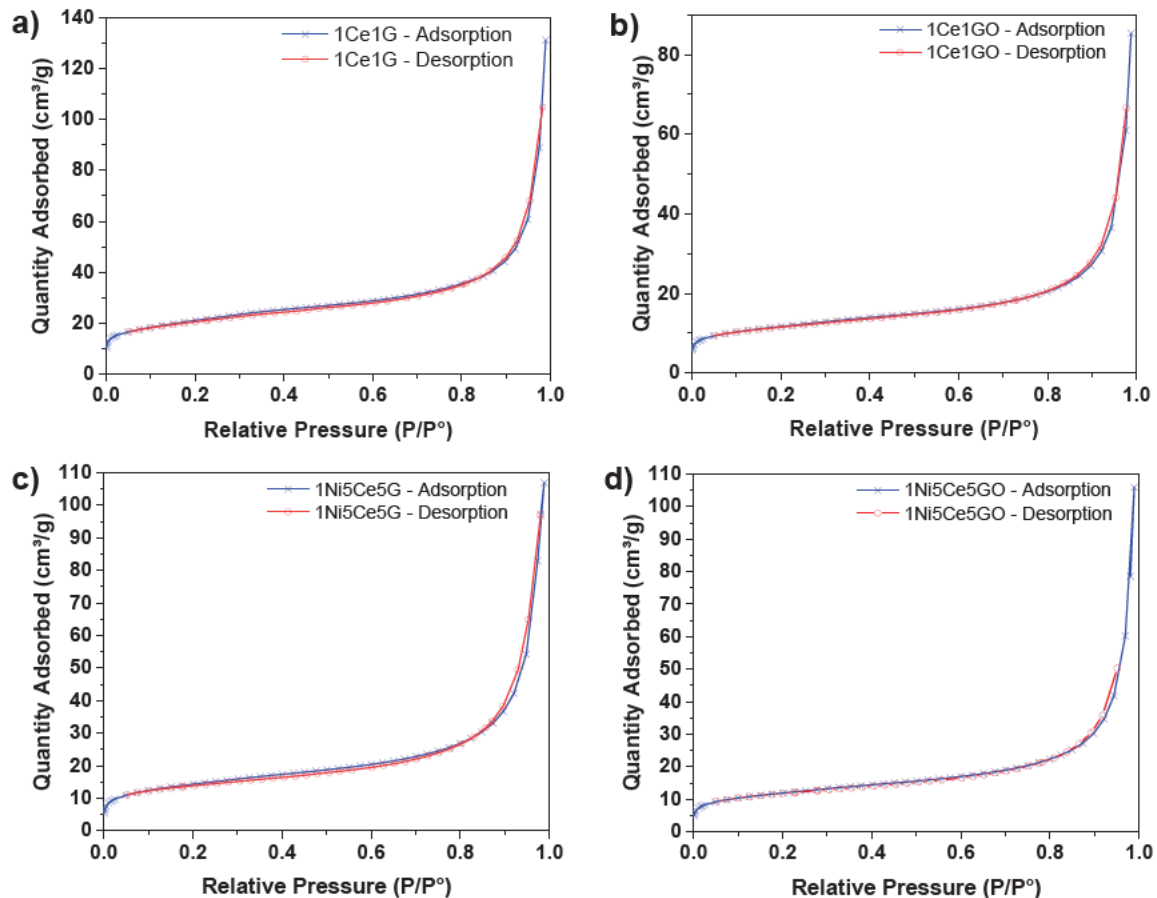
Figure 44. N$_2$ adsorption-desorption isotherms of: a) 1Ce1G, b) 1Ce1GO, c) 1Ni5Ce5G, and d) 1Ni5Ce5GO.

As mentioned in the methodology, the surface area was calculated using BET and NLDFT models. The NLDFT model was fitted to the adsorption isotherm, using the software SAIEUS (Graphs in **Annex II)**. The SA estimations from BET and NLDFT, as a function of the total metal oxide content (CeO$_2$ and NiO) for each sample are presented in **Figure 45**. A slight difference between both methods can be noticed, however, the materials follow a similar trend to increase their surface area with the increase of metal content of the same type. That is, approximately 60 to 70 m^2/g for CeO$_2$/GNP materials and 25 to 45 m^2/g for CeO$_2$/OGNP.
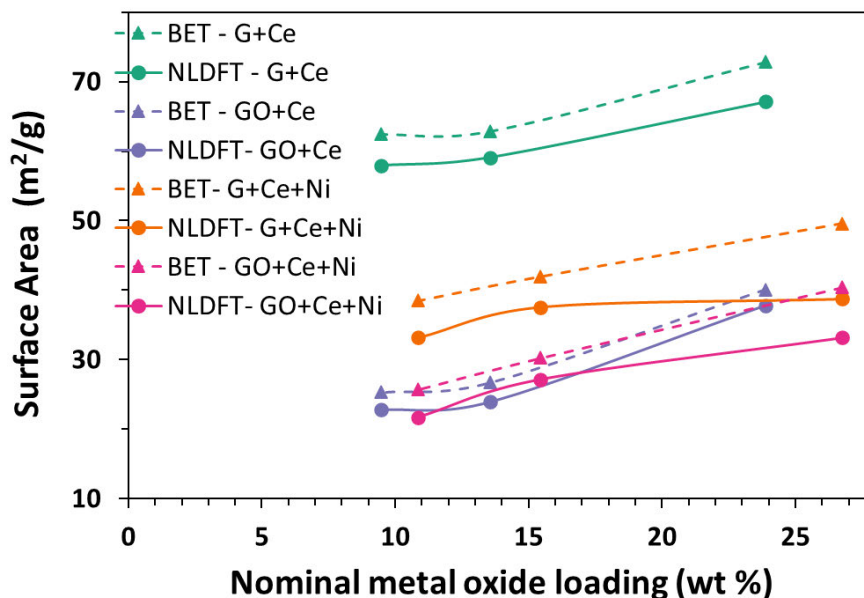
Figure 45. Surface area estimated by BET and NLDFT models as a function of the theoretical content of metal oxides.

Regarding the addition of nickel, only with GNP as support, a notable decrease is observed in the surface area of materials containing this metal, with similar total contents of metal oxides. This means that there is a different effect or interaction in the deposition of nanoparticles by the type of carbonaceous support (GNP and OGNPs).

Figure 46 shows the pore size distribution (PSD) of the samples, calculated by fitting the nitrogen adsorption data to a Nonlocal Density Functional Theory (NLDFT) model. The NLDFT is more accurate than the BJH method for studying the microporous-mesoporous region.

In this sense, NLDFT-PSD shows that composite materials have micro- and mesopores in the 5 Å to 300 Å range. In addition, the PSD shows a significant difference, mainly in the zone of microporosity (pore size up to 20 Å), this may be

associated with the incorporation of nanoparticles (CeO$_2$ and/or NiO), leading pores

between the nanoparticles with different sizes.
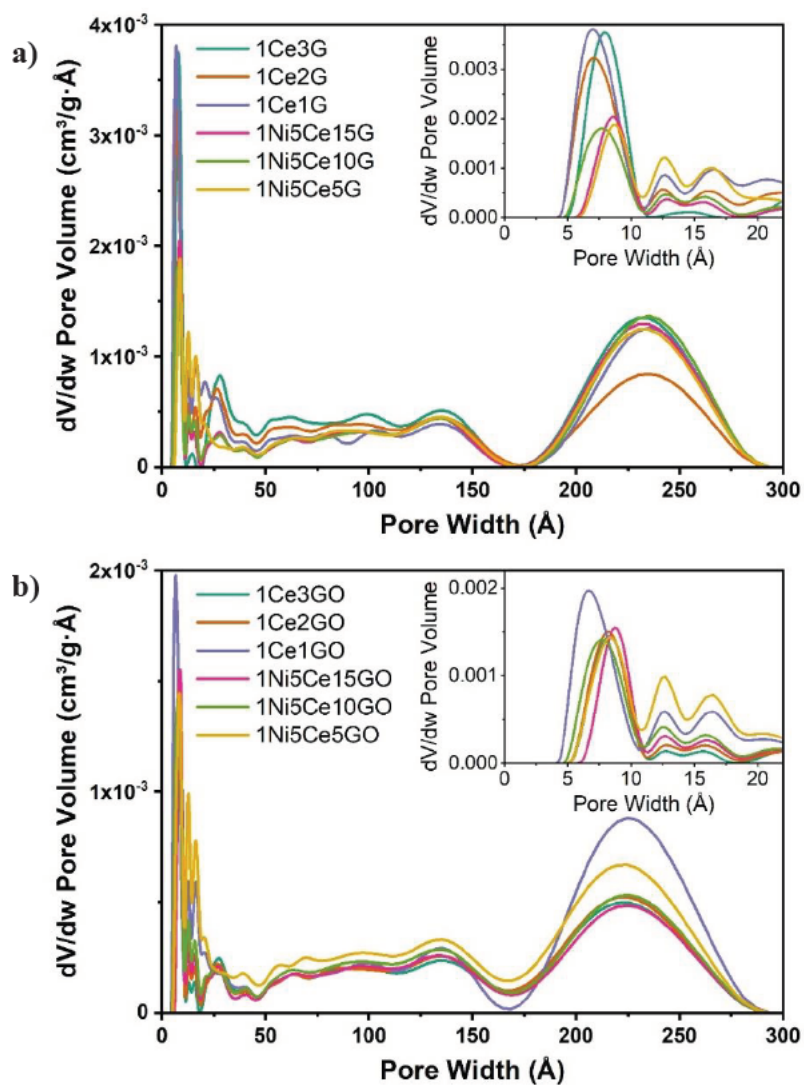
Figure 46. Pore size distribution by NLDFT of samples supported in a) GNPs, b) OGNPs.

Thermal stability (pyrolysis and oxidation) by TGA-DSC

The weight loss (TGA) and heat release (DSC) curves resulting from heating the samples in air are presented in **Figure 47**. The weight loss of graphene samples starts around 450 °C, while graphene oxide samples start losing weight around 500 °C. Exotherms in the 500 to 700 °C region, shown in the DSC thermogram, confirm the oxidation of materials releasing CO and CO_2.
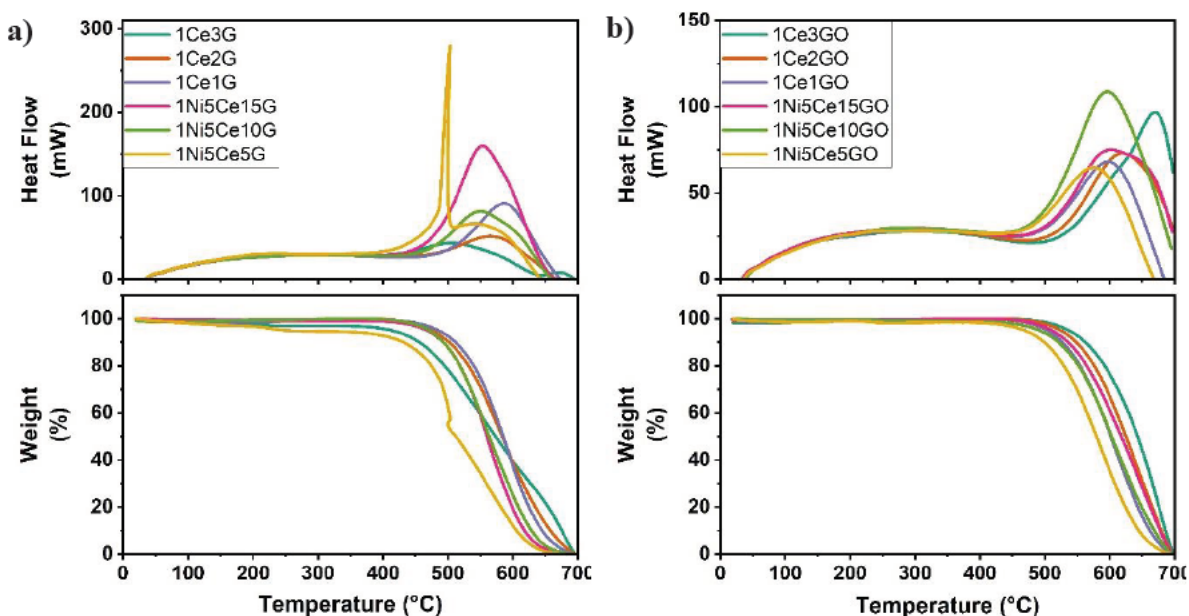
Figure 47. DSC and TGA thermograms of the samples supported in a) GNP and b) OGNPs.

The weight loss at 700 °C (at the end of the analysis) in air is shown in **Figure 48**. There is a tendency to decrease with the load of metal oxides. This confirms the increase in oxygen groups in the materials, so the heat generated by oxidation is lower. In addition, materials supported in OGNPs presented less weight loss than those supported in GPNs at similar concentrations, due to the presence of oxygen

groups in graphene oxide, it is less sensitive to the oxidation atmosphere because it is already partially oxidized.
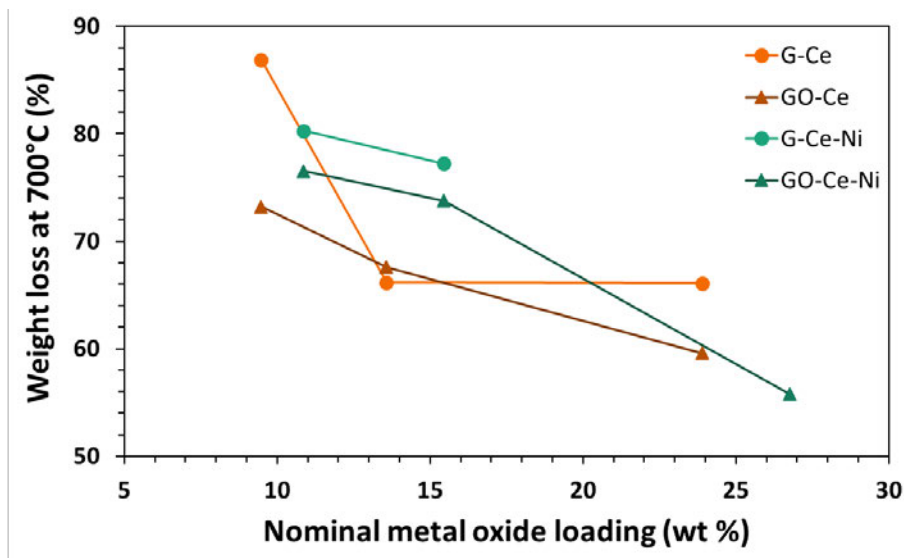
Figure 48. Weight loss up to 700 °C as a function of the theoretical content of metal oxides.

Lastly, the results of the TGA in nitrogen atmosphere were omitted since they did not present a significant signal in the measured range, which means that the material is stable in that environment up to 700 °C.

Metal (elemental) content by ICP

The deviation from the expected concentration of metals can be visualized in **Figures 49 and 50**. From **Figure 49** it can be deduced, as previously mentioned, that the synthesis method is suitable for depositing ceria nanoparticles in different proportions on graphene. In contrast, it is observed that there are samples with greater differences in the content of metal oxide (7.6% by weight difference in the sample 1Ni5Ce5G, about 3% by weight difference in samples 1Ce1G and 1Ce1GO), and these are the highest expected concentration (23 and 24% CeO_2 by theoretical

110

weight). This could occur by reducing and/or saturating the availability of sites on the graphene support to interact with the ceria. Additionally, there does not seem to be a difference in the type of support, that is, between oxygen-functionalized or non-functionalized graphene, OGNPs and GNPs, respectively.
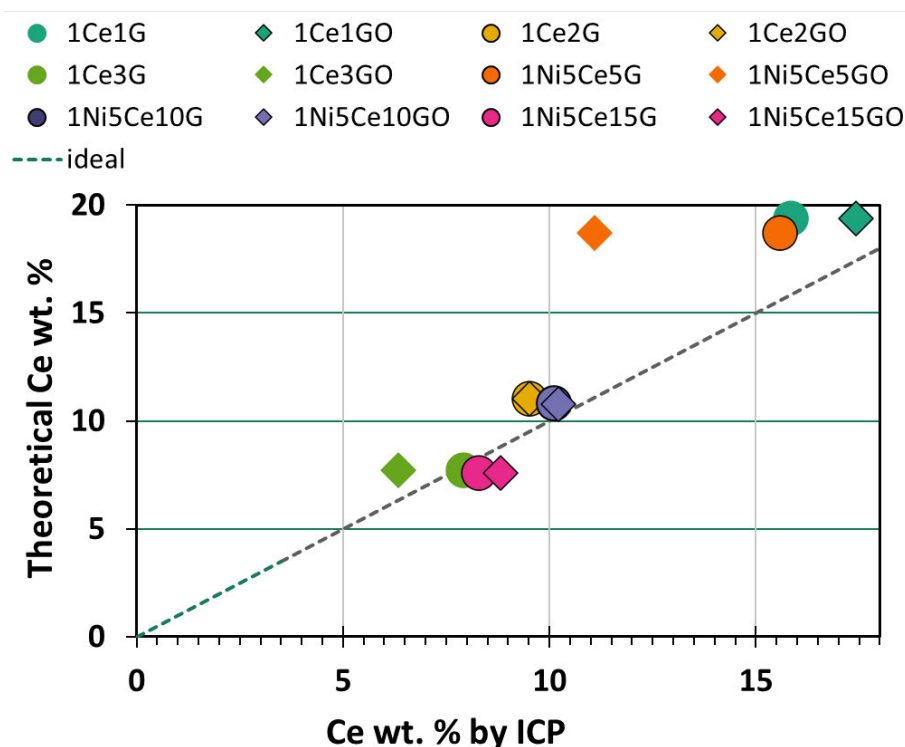
Figure 49. Deviation of the Ce concentration obtained by ICP in the materials.

On the other hand, **Figure 50** shows the deviation between the real and the theoretical nickel addition. In this one, there is a greater difference concerning the expected percentages, which is expected in a certain way since the theoretical percentage is very low. It is worth mentioning that the ICP-OES technique has a detection limit of about 5 (µg/L) [103], equivalent to a sample Ni content of 6.25 ppm. Therefore, the discrepancies could be due to the small amount of material used in the analysis, which also has a very low concentration of Ni, there could also be errors in the preparation of the samples or to the heterogeneity in them.
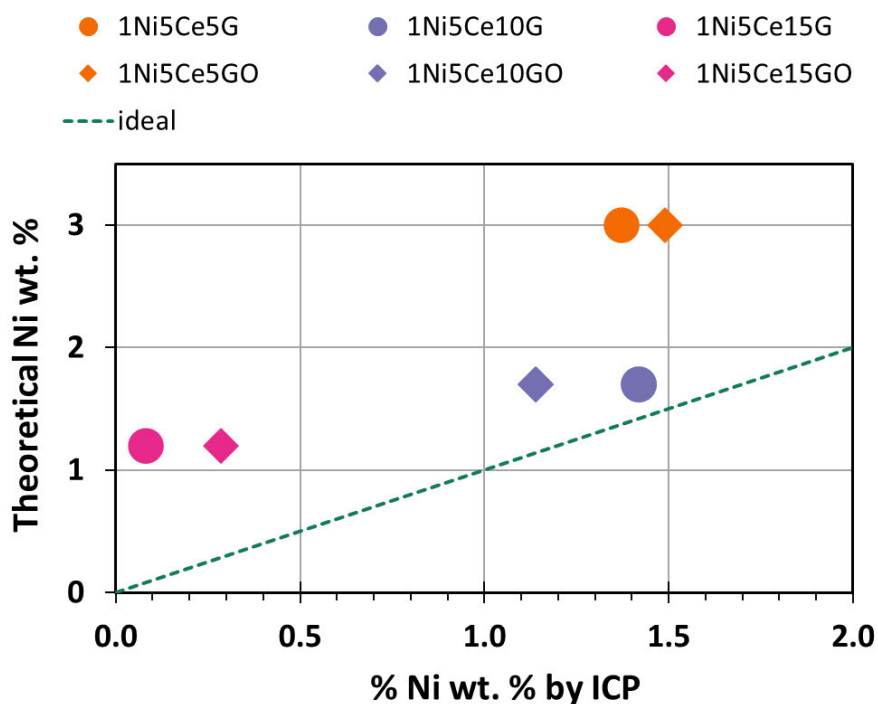
Figure 50. Deviation of the concentration of Ni obtained by ICP in the materials.

To compare the results of ICP with those obtained by XRD, the percentage by weight obtained from the quantification of the crystalline phases of the metal oxides identified in the diffractograms (cerianite, CeO_2 and bunsenite, NiO) has been converted. These contents were converted to elementary content using stoichiometric ratios and their atomic mass units. The results can be visualized in **Figure 51.**

In this graph, the tendency to obtain a higher Ce content employing the ICP technique is remarkable, which could indicate cerium doping capacity in graphene,

since it indicates a greater amount of Ce in samples that do not have a crystalline structure.

In the case of Ni in the samples, apparently, it does not interact as a dopant in the compounds since it presented a higher content by its analysis by XRD, which means that it belongs to the crystal structure of NiO.
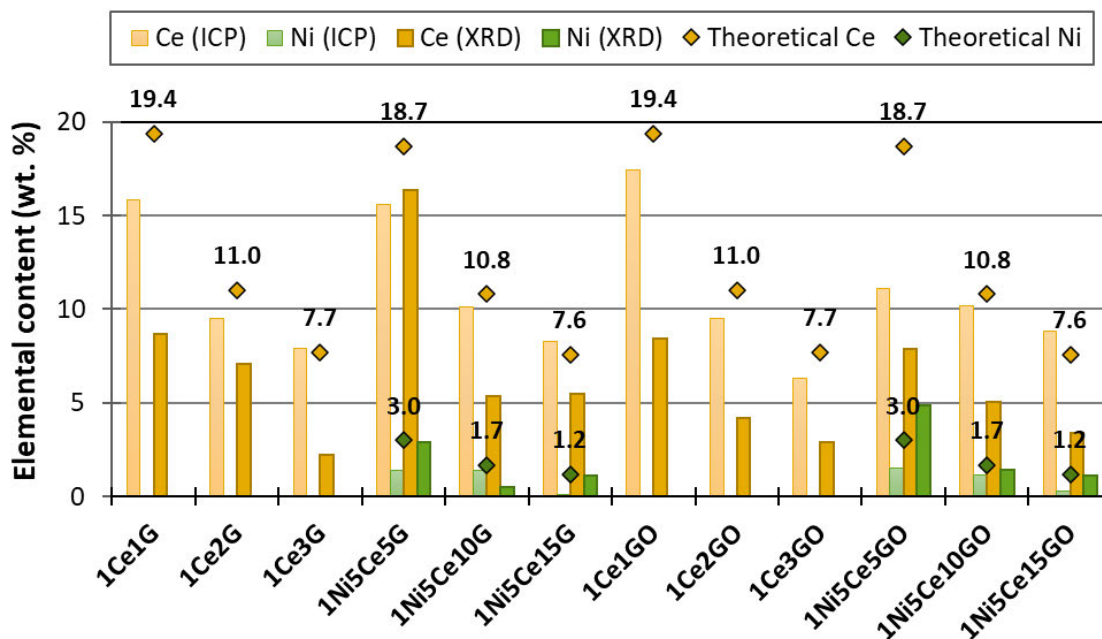
Figure 51. Elemental content of metals (Ce and Ni) in the samples, theoretical and estimated by ICP and XRD.

Figure 52 presents the relative error in the quantification of metals and metal oxides by different characterization techniques. It is important to consider that each technique has its limitations or considerations to be able to quantify the materials. The values of the content of Ni in the samples present a greater deviation than those of Ce, probably due to it being more dispersed in the sample and the concentrations of this metal being lower.
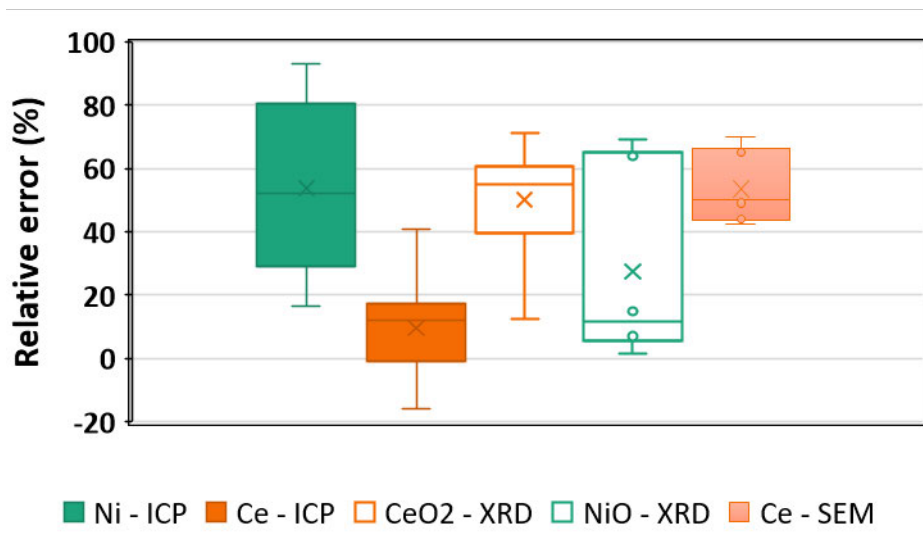
Figure 52. Variation of the relative error in the quantification of metal content or metal oxides in the samples by different techniques.

6.4. Remarks

The 1Ni5Ce5G sample was synthesized using 2 types of solvents: 1,4-butanediol and ethylene glycol, and certain differences in the resulting materials were observed depending on the type of solvent. The material synthesized with butanediol shows the deposition of Ni nanoparticles and a concentration very similar to that expected, in addition, its structural properties indicate greater deposition or doping with Ni. These characteristics indicate that 1,4-butanediol is more appropriate for the synthesis and simultaneous deposition of CeO_2 and Ni.

Changes in pore size distribution suggest that nanoparticles, both CeO_2 and NiO, are deposited between graphene sheets during synthesis. The materials obtained have good thermal stability around the desired working temperature (around 400 °C).

By Raman spectroscopy, it was possible to evaluate some changes in the microstructure of graphene with the content of NiO and CeO_2. It was appreciated

114

that there is a different interaction with the supports (GNPs and OGNPs), concerning the introduction of defects.

The elemental contents of the metals deposited in graphene were obtained by the ICP analysis. The results show that CeO_2 is deposited in concentrations similar to those expected, although in materials with higher content of this, there is a greater difference with what was expected, this is attributed to the decrease in the availability of sites where it is deposited, in addition to the difference between the results of ICP and XRD, it can be expected that part of the available Ce is doping graphene. The discrepancy in the content of elementary Ni is because having a lower content is harder to analyze accurately; however, in some samples the results seem to be closer to the expected.

7. CATALYTIC PERFORMANCE EVALUATION

7.1. Evaluation of the reducibility of materials by X-ray absorption

7.1.1. Materials and methods

X-ray absorption spectroscopy (XAS) was applied to the materials to deep insight into their structural changes when undergoing reduction (ex-*situ*). Analyses on the X-ray absorption near-edge structure (XANES) and the extended X-ray absorption fine structure (EXAFS) were performed on the soft X-ray microcharacterization (SXRMB) beamline at the Canadian Light Source (CLS) The line uses a bending magnet source to bend the path of the electron beam and covers a spectral range of 1.7 - 10 keV. The samples (Ce and Ni) were analyzed using the solid-state end station equipped with fluorescence yield (FLY) and total electron yield (TEY) detectors. The obtained spectra from XANES (Ce) and EXAFS (Ni) were processed in the Athena software [104].

Before analysis, the samples **(Table 17)** were subjected to reduction treatment at 250, 300, and 350 °C. To do this, about 10 mg of powder sample was taken and pressed in a *six-hole shooter* capable of processing 6 samples at a time. The shooter with the catalyst samples was installed in a quartz tube reactor and the treatment was carried out for 3 h. After treatment, the reactor was cooled to room temperature while 100 ml/min of N_2 flowed through it. The reactor was sealed and taken to a glove box to protect the samples from reoxidation while they were deposited on a plate for scanning in XAS.

Table 17. Composition of samples (as prepared) studied by X-ray Absorption

	Composition (wt. %)		
Sample	**Graphene**	**CeO$_2$**	**NiO**
1Ce3G	91	9	
1Ce3GO	91	9	
1Ni5Ce5G	73	23	4
1Ni5Ce5GO	73	23	4
1Ni5Ce10G	85	13	2
1Ni5Ce10GO	85	13	2

7.1.2. Results and discussion

The oxidation state of Ce was assessed by XANES (the region near the X-ray absorption edge) at the L3 border. This method is simple and applicable to valence determination in rare earth compounds [105].

A typical spectrum for CeO$_2$ consists of 4 signals, identified as A, B, (high energy) C (low energy), and D (pre-edge peak). Component A is assigned to the final excited state of Ce4+ with configuration 2p4f05d*, where 2p denotes a gap in the 2p layer (J=3/2), while 5d* refers to the excited electron with configuration 5d. Component B, also assigned to Ce^{4+}, corresponds to a 2p4f05d*L state, where L represents a gap in the ligand anion orbital. Component C (5727-5729 eV) is attributed to the presence of Ce^{3+} as an impurity. Finally, the weak component, D, is explained by a forbidden transition from 2p$_{3/2}$ to 4f as a result of 5d admixtures to the 4f state [105,106].

Following the above, the percentage of ceria in its reduced state was determined, that is, the concentration of Ce^{3+} in the CeO_2 matrix. The following relation [106,107] was used:

$$[Ce^{3+}] = A(Ce^{3+})/(A(Ce^{3+}) + A(Ce^{4+}))\qquad(16)$$

Where $A(Ce^{3+})$ and $A(Ce^{4+})$The peak areas correspond to oxidation states 3+ (C) and 4+ (A and B). These areas were obtained by fitting the data to Gaussian curves and using an arctangent function to simulate the jump on the axis and remove the background. An example of this setting is illustrated in **Figure 52**.
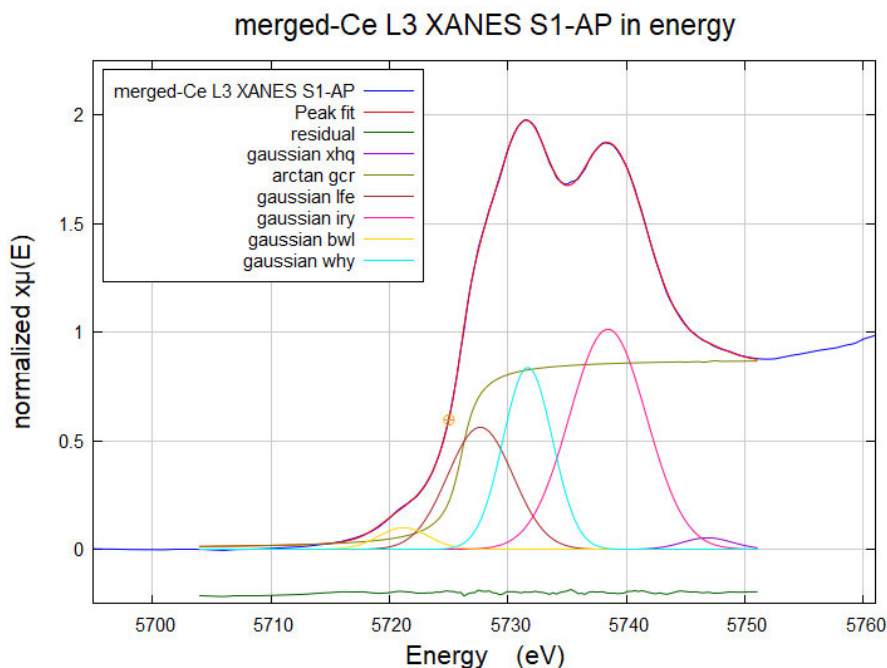
Figure 53. An example of curve fitting in Athena software [104], shows 1Ce3G as prepared (unreduced).

Figure 54 shows the proportion of cerium that is in oxidation state III, as a function of the temperature to which each sample was reduced, as well as before reduction. In general, it can be perceived that the content of Ce^{3+} decreases with the addition of NiO nanoparticles, which can be attributed to the interaction between these phases so that oxygen atoms bonded to the structure of cerium and nickel are found at the interface of the crystals.

The reduced state of CeO_2 (Ce^{3+}) is diminished by the NiO content. This probably occurs due to the introduction of oxygen atoms to carry out the anchoring of NiO nanoparticles in the ceria. These oxygen atoms are strongly bonded, so that a Ce-O-Ni interface is formed. **Figure 54** shows the structure of cerianite (CeO_2) and how a part of the structure of bunsenite (NiO) could be anchored.
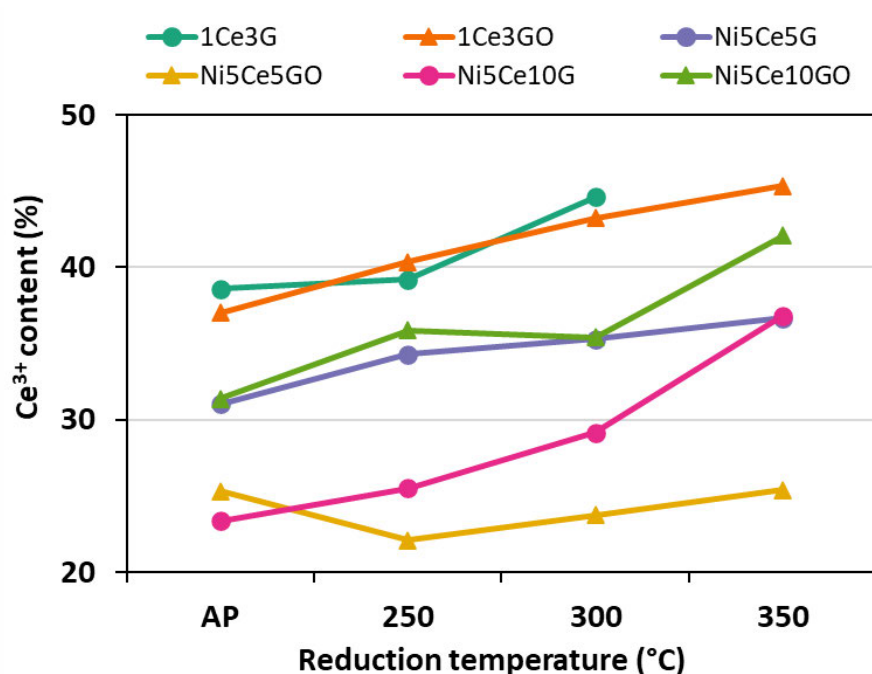
Figure 54. Proportion of Ce^{3+} with respect to the CeO_2 matrix as a function of the reduction temperature (AP = material as prepared, without reduction).
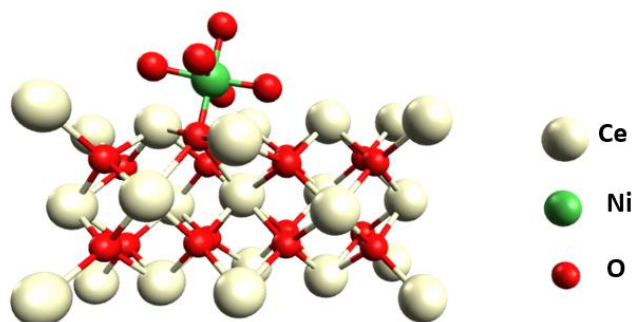
Figure 55. Figure 50. NiO anchoring in the cerianite (CeO$_2$) structure

Regarding the differences in the type of carbonaceous support (GNPs and OGNPs), the content of Ce^{3+} is very similar when they do not contain NiO, both initially and at different reduction temperatures. However, in materials with GNPs, there is a direct relationship between the content of Ce^{3+} and the addition of nanoparticles of CeO$_2$ and NiO. This is a consequence of the agglomeration of the supported nanoparticles, hindering the mobility of ions and therefore the reduction.

This happens oppositely in materials supported by OGNPs, which can be explained by the ability of the supports to promote the dispersion of deposited nanoparticles. In oxygen-functionalized graphene (OGNPs) the particles are more dispersed and homogeneous (see 4.2.2 section), promoting ceria reduction.

It should be noted that the materials that present a greater reduction, in comparison to their initial state (greater than 10%), correspond to those that have a higher graphene content (see **Table 17**) and lower NiO nanoparticle content (1Ni5Ce10G and 1Ni5Ce10GO). This observation could be evidence that a hydrogen Spillover phenomenon is promoted by graphene and nickel in the reduced state, in which these phases adsorb hydrogen, migrates in a dissociated form towards CeO$_2$ and

120

promotes its reduction. This phenomenon occurs at low concentrations of Ni, which would result in an advantage in terms of production costs of this type of catalyst.

On the other hand, the reducibility of NiO nanoparticles was studied through Fine Structure Extended X-ray Absorption Spectroscopy (EXAFS). This technique allows information about structural parameters such as interatomic distances and coordination numbers of nearby neighbors [108]. **Figure 56** shows the absorption spectra obtained at the Ni-K edge of the samples after their reduction at different temperatures, compared with the nickel sheet as a standard of Ni^0, and the respective Fourier transforms.

As can be seen, all samples exhibit similar behavior. At first glance, it is noticeable that as the reduction temperature of the material increases, the signals are more similar to those of the metallic Ni standard. The first coordination sphere in the unreduced samples, about 1.8 A, corresponds to the Ni-O bonds. It can be seen that its intensity also decreases as the reduction temperature of the materials increases. In addition, a peak shift of around 2.5 A can be seen in the unreduced sample to 2.2 A in those reduced to 350 °C. This suggests a change in the distance of the Ni-Ni bonds due to reduction, which is consistent with that reported in the literature [109,110].

The above means that the reduction of Ni in the samples is occurring and favored at a higher temperature (350 °C). In previous work, it was observed at a reduction temperature of 290 °C for the NiO bulk, while, it was said that the reduction of Ni cations in the crystal lattice of ceria is reduced from 400 to 700 °C [10].
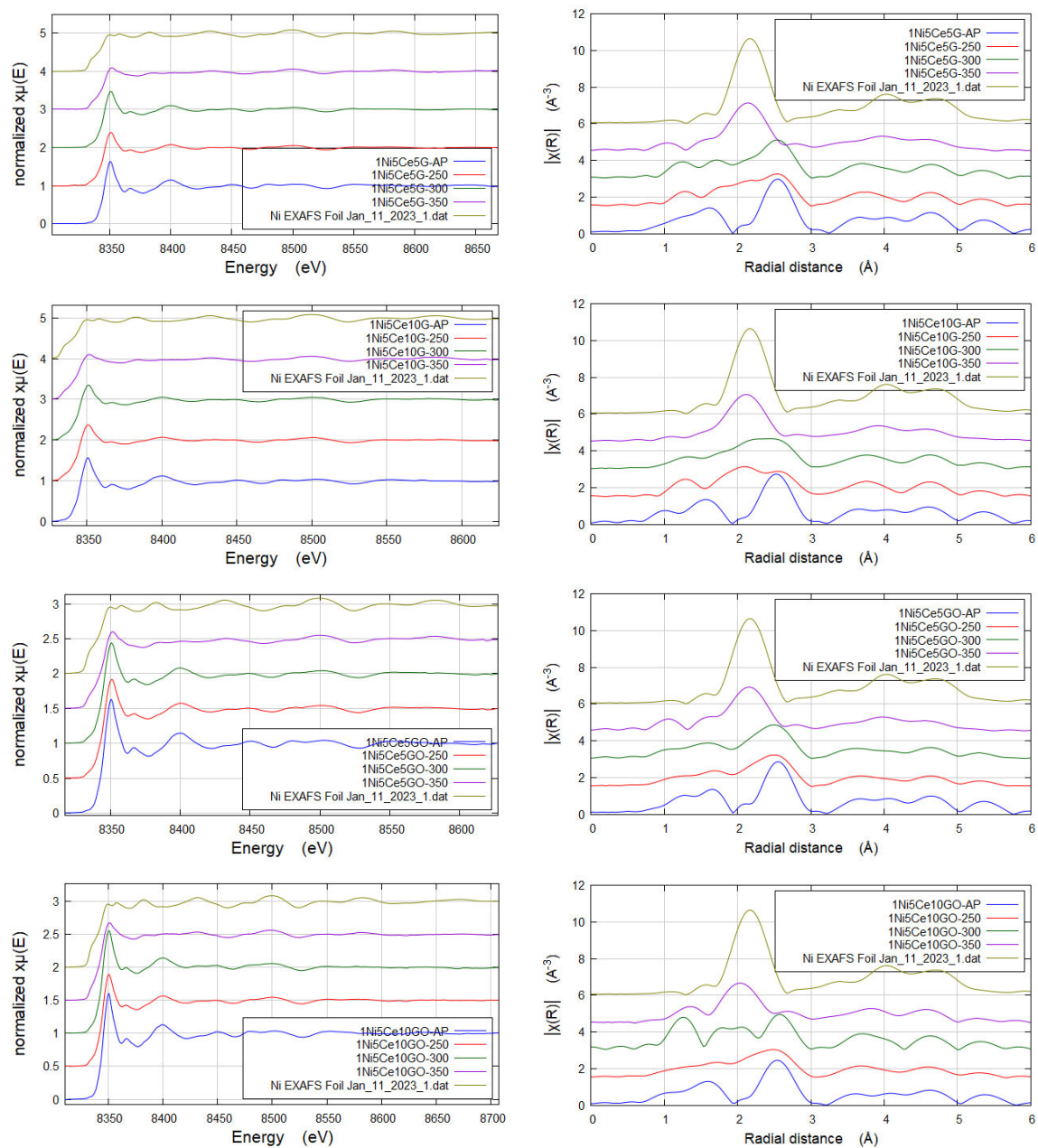
Figure 56. EXAFS spectra on the Ni-K edge of the samples and their respective Fourier transforms (right).

The degree of reduction of Ni in the materials was quantified using the "*linear combination fitting"* mode in the Athena software [104], which adjusts an unknown

spectrum to a standard. In this case, Ni0 spectra and that of the same unreduced sample were used as standard.

The results of the degree of reduction as a function of temperature are summarized in **Figure 56.** It is observed that the reduction of Ni in materials is carried out with a similar trend, in terms of temperature. Thus, about 30% of Ni reduction is achieved at 250 °C. Whereas, at 300 °C, there appears to be a decrease in the reduced nickel content, Ni0, which tends to be more noticeable in materials with higher graphene oxide content (OGNPs). Finally, at 350 °C the materials reach about 75% reduction of Ni, again the material with more graphene oxide content (1Ni5Ce10GO) presents a lower reduction degree because the oxidized species present in graphene coordinate with Ni limiting its oxidation.

It is worth mentioning that, although most of the NiO in the samples is reduced, the remaining percentage (about 25%) could be the result of the strong Ce-O-Ni interaction due to the formation of a mixed oxide of $Ce_{1-x}Ni_xO_{2-y}$, which requires a higher temperature for its reduction, since it involves the reduction of Ce^{4+} to Ce^{3+} as well as the reduction of Ni to Ni^0 [10].

Through this analysis, it was possible to demonstrate that the graphene support influences the reduction of metal oxides due both to the dispersion that is promoted with the available oxygen functional groups, and by a metallic behavior that mobilizes the hydrogen ions adsorbed to the surface.
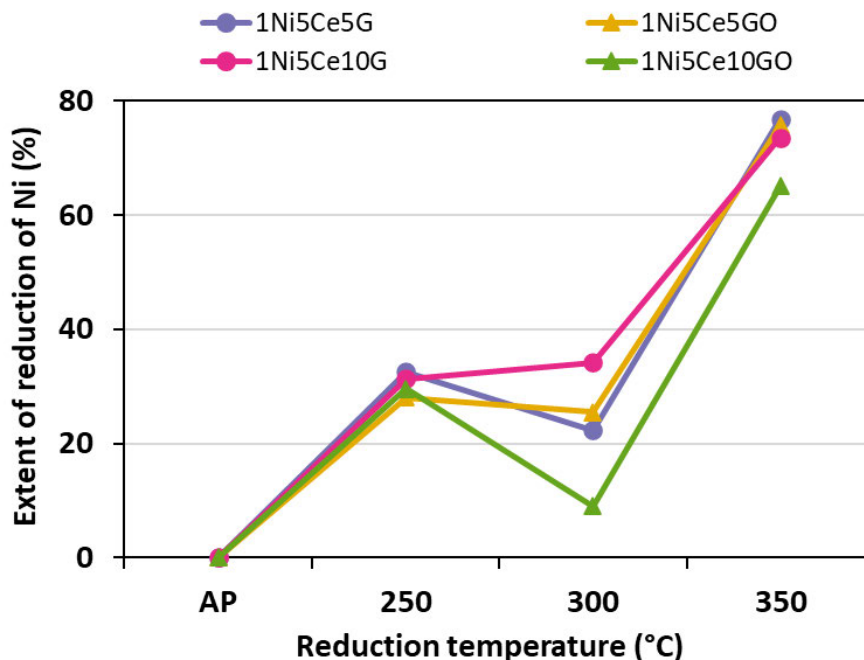
Figure 57. Extent of reduction of Ni as a function of the reduction temperature (AP = material as prepared, without reduction).

7.2. Evaluation in water-gas shift reaction (WGSR)

7.2.1. Materials and methods

As previously mentioned, this work proposes evaluating the performance of catalysts in WGSR, as an intermediate step for the *in situ* production of hydrogen that can be used in the Upgrading of oils. In this aspect, some of the previously characterized materials were selected: 1Ce3G, 1Ce3GO, 1Ni5Ce10G, and 1Ni5Ce10GO. The last 2 contain Ni nanoparticles in low concentration and according to the EXAFS results, tend to have a greater degree of reduction than those with twice Ni. The material was sieved to obtain 2-3 mm particles, and 1 g of the sieved catalyst was placed in the fixed-bed reactor.

The reaction system shown in **Figure 58** was used. Before the reaction, the catalyst was reduced with 100 ml/min of H_2 flow at 350 °C for 3 h. Subsequently, it was purged with N_2, and the temperature was lowered to 200 °C, passing water with a flow of 0.003 ml/min for 20 min. Subsequently, the temperature in the reactor was increased to 300 °C, and once reached, the CO-Ar mixture flowed to maintain a spatial velocity, WHSV of 0.2 h^{-1} (WHSV = mass flow of CO/mass of the catalyst).

The reaction system was kept at this temperature for 1 hour to reach equilibrium and then samples of the effluent gas were taken. Then the temperature was increased by 20 °C and the procedure was repeated up to 400 °C.

Gas mixture analysis was performed on an Agilent 6890 gas chromatograph with a TCD detector and an Altech 28301PO packed column, using N_2 as the carrier gas.

The conversion of CO and selectivity towards the products H_2, CH_4, and CO_2 was estimated at the different reaction temperatures by the following equations:

$$Conversion \ of \ CO = \frac{n \ CO_{feed} - n \ CO_{products}}{n \ CO_{feed}} \tag{17}$$

$$Selectivity_i = \frac{(n_i)_{products}}{\Sigma_i(n_i)_{products}} \tag{18}$$
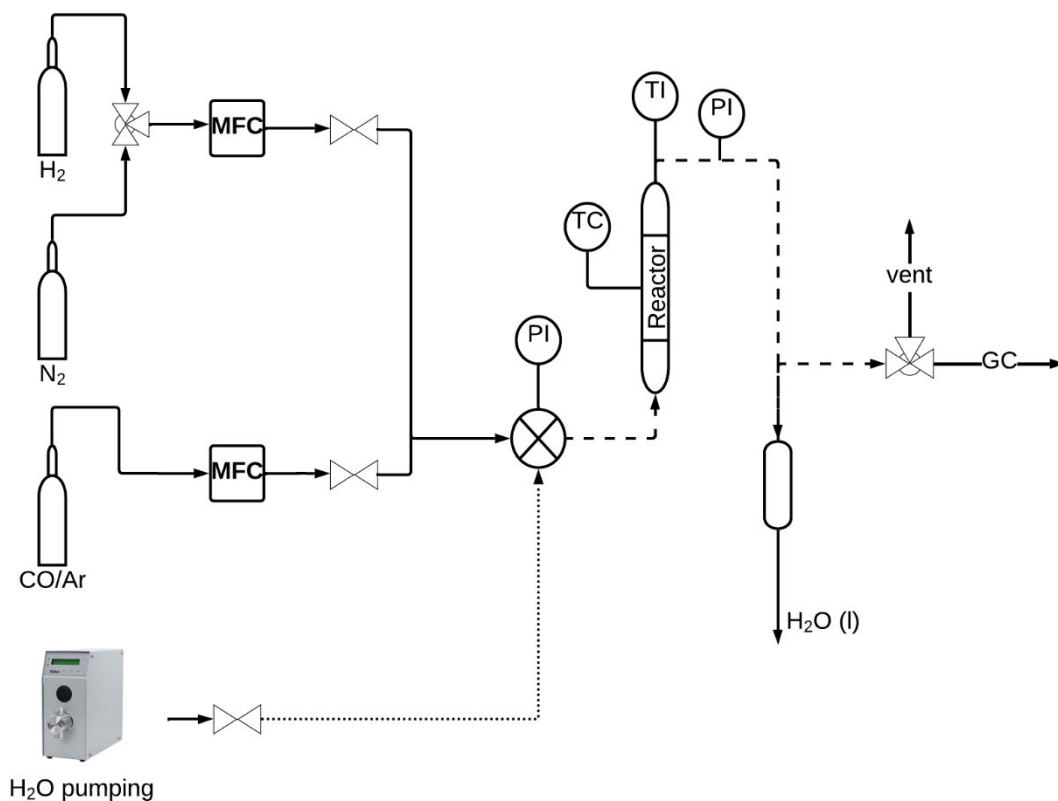
Figure 58. Diagram of the system used for WGSR

7.2.2. Results and discussion

Figure 59 shows the CO conversion results and the selectivity towards the products obtained (H_2, CH_4 and CO_2) of WGSR in the 300-400 °C range. An important fact is that all materials show activity towards WGSR under the conditions evaluated. In another published work, a CO conversion of less than 2% was obtained in the CeO_2/C support, indicating that Ni is the one that takes the role of the active phase in WGSR [111].
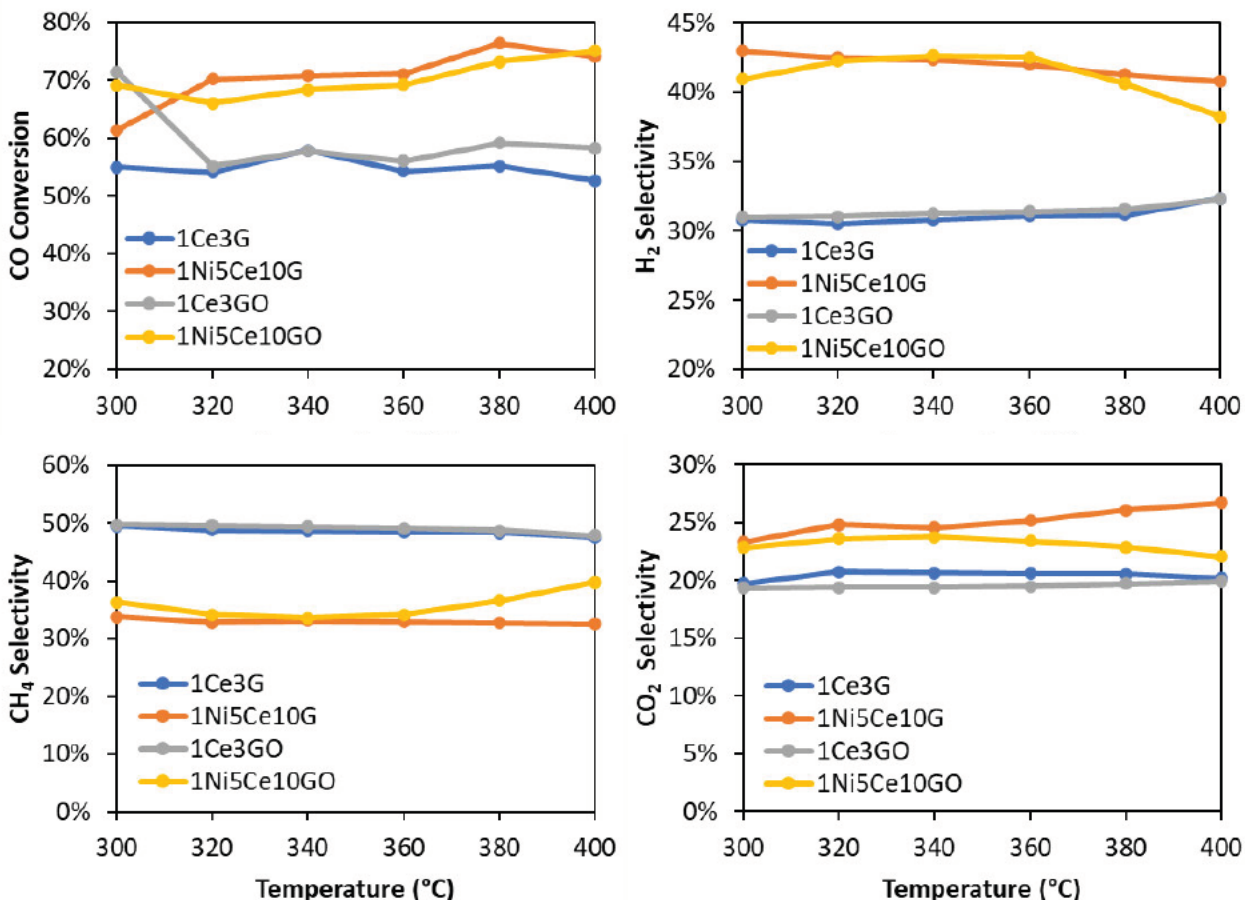
Figure 59. CO conversion and selectivity towards the respective WGSR products with 1Ce3G, 1Ni5Ce10G, 1Ce3GO and 1Ni5Ce10GO catalysts.

At first glance, there is a big difference between materials with and without Ni nanoparticles, since, with the addition of these, the conversion of CO increases by more than 10%, and even about 20% at higher temperatures. In addition, the effect of temperature on increasing conversion is more noticeable in materials with Ni, which can also speak to the catalytic activity of materials.

Regarding selectivity, a considerable difference between the materials with the deposition of Nickel was noted. In the case of obtaining hydrogen, it is observed that materials with Ni exceed approximately 10% of those that do not contain it. In

addition, at lower temperatures, materials with Ni, have greater selectivity towards H_2, although the variation is very little with the increase in temperature, at higher temperatures, the production of hydrogen decreases.

On the other hand, non-Ni-containing materials (1Ce3G and 1Ce3GO) were found to be around 20% more selective towards CH_4. This characteristic is interesting, since it is contrary to what is expected, since it is generally accepted that the supported nickel nanoparticles are highly active towards methane production [10,27,110].

The increase in selectivity towards CH_4 with the catalysts 1Ce3G and 1Ce3GO could be attributed to the fact that graphene acts as a metal during the reaction, that is, it adsorbs CO molecules, however, it promotes its dissociation, which leads to the formation of species of the formate group, which are intermediates in the production of methane by hydrogenation of CO_2 [113].

On the other hand, it is proposed that the lower selectivity towards CH_4 in catalysts 1Ni5Ce10G and 1Ni5Ce10GO is due to the chemical adsorption of CO in Ni, but with an inhibition of the breakdown of the C-O bond, this is likely by strong electronic interactions between the metal and support. The electron-enriched metal ($Ni^{\delta-}$) could increase electron donation to the $2\pi^*$ orbital of CO, increasing its chemisorption strength at an interface of the $Ni^{\delta-}-O_v- Ce^{3+}$ type [114]. An improvement in CO adsorption related to the electron density of the interfacial metal and inhibits methane formation [27,112]. This agrees with a "redox" reaction mechanism that involves the formation of CO adsorbed to result in the formation of CO_2.

It is worth mentioning that the catalysts studied have catalytic activity and deactivation at different temperatures under the reaction conditions studied. Thus, the catalyst with which the highest production of H_2 is obtained corresponds to 1Ni5Ce10G. The highest production obtained with this material is at 380 °C, and its catalytic activity decreases with a higher temperature (400 °C).

7.2.3. Remarks

The catalytic evaluation of the materials included the study of their reducibility, which is an important parameter to activate the catalysts and can give indications of their behavior in the catalytic reaction. The reduction of CeO_2 and NiO in different samples was analyzed. The observed CeO_2 reducibility was similar among materials without Ni. The differences in the behavior of materials with Ni, with different supports and concentrations, show a synergistic effect between this metal and graphene, which promotes the reduction of CeO_2. Materials with a lower Ni content exhibit higher reducibility of CeO_2.

On the other hand, the dispersion of CeO_2 in graphene (improved with functionalization) also influences its reducibility. NiO reducibility is achieved by a similar percentage for all materials at 350 °C, but slightly lower for 1Ni5Ce10GO material. About 25% of Ni remains as Ni^{2+}, possibly due to a strong interaction by forming a mixed oxide of type $Ce_{1-x}Ni_xO_{2-y}$.

Regarding the activity in WGS, it was observed that even a low quantity of supported Ni NPs increases the conversion of CO by 20 %. In addition, there was no noticeable effect due to the type of graphene support with the selected samples. However, this

might be different from other samples. It is estimated that CO adsorption occurs with less extension in materials without deposited Ni deposited, changing the reaction route and promoting the formation of methane.

8. CONCLUSIONS AND PERSPECTIVES

In the analysis of graphene as a catalytic support, in the form of functionalized and non-functionalized nanoplatelets, it was observed that these materials (GNPs and OGNPs) have structural-crystalline differences and in the availability of functional groups, which influences the deposition and dispersion of nanoparticles.

The materials with OGNPs present a great dispersion nanoparticle of CeO_2, this is due to the availability of functional groups of oxygen in the graphene functionalized with oxygen. In addition, a higher proportion of Ce^{3+} was distinguished in materials with graphene than in pure CeO_2, prepared under the same conditions, indicating a strong electronic interaction between these phases.

The study of the $Ni-CeO_2$ system was carried out to study in a more simplified way the synthesis and deposition of Ni in low concentrations in composite materials. In this sense, the synthesis was selected using butanediol as the solvent and $Ni(NO_3)_2 \cdot 6H_2O$ as the precursor salt of Ni. With these conditions, it is perceived that there is an introduction of defects such as oxygen vacancies with the deposition of Ni and that it is also associated with possible doping by substitution of Ni in the structure of CeO_2.

The characterization of the $NiO-CeO_2$-graphene composites was somewhat complex since, in addition to there being 3 different crystalline phases, there are interactions between them, and there is a low concentration of Ni of which, a part is in the form of widely dispersed nanoparticles and another part as a dopant. However, compounds with concentrations similar to those expected were obtained. When

evaluating structural properties, it was noted that there is an interaction between the carbon support and the nanoparticles and that it occurs differently between the two types of graphene. The surface area of materials tends to increase with the addition of nanoparticles, and the density of micropores increases (< 20 Å).

The *ex-situ* study of structural changes with the reduction of materials showed that at 350 °C about 70% reduction of Ni^{+2} to Ni^0 is achieved. The remaining percentage of Ni^{2+} could be related to the formation of a mixed oxide solution of the type $Ce_{1-x}Ni_xO_{2-y}$, this observation coincides with the doping or substitution of Ni in the structure of CeO_2. This study also showed the influence of Ni on CeO_2 reducibility, since the proportion of Ce^{3+} in the ceria matrix is lower with NiO content. This is attributed to the anchoring of NiO nanoparticles, forming a strong Ni-O-Ce interaction at the interface. However, there is synergy between the graphene phases explained by the H_2 Spillover phenomenon.

Finally, in the evaluation of WGSR, it was observed that the selected materials present catalytic activity to the operating conditions studied. No significant difference was obtained in the conversion of CO achieved with materials with different types of support (GNPs and OGNPs), however, there is an increase in catalytic activity with the addition of a low amount of Ni (2% by weight), which again is attributed to a synergistic effect between the phases of the compounds. The materials with Ni turned out to have a greater selectivity towards H_2 and CO_2 and lower towards CH_4 due to an increase in the strength of chemisorption of CO, given by an electronic effect at the interface of the type $Ni^{\delta-}-Ov-Ce^{3+}$.

Among the catalysts evaluated, the sample 1Ni5Ce10G presented a higher production of H_2 at 380 °C, reaching a CO conversion of 76 % with a selectivity towards H_2 of 41 % and towards CH_4 of 33 %.

In general, catalysts with adequate performance and stability were obtained by a method of synthesis and deposition of a single step, with low concentrations of a transition metal (Ni), which would also be active in oil improvement processes through the production of hydrogen *in situ* and subsequent reactions of addition of H_2 (hydrogenation), as is Aquaprocessing.

Some of the areas of opportunity for the materials generated in this work are:

The study of the adsorption of CO in materials would be useful to deepen the reaction mechanism that takes place. Adsorption followed by programmed temperature desorption (TPD) could assess the strength of CO is adsorbed to the materials.

The material reduction could be studied with programmed temperature (TPR) methods to complement the information obtained in the XAS analysis.

Having access to a synchrotron light laboratory could apply the analysis of the pair distribution function (PDF), through which the *in situ* reduction of materials could be evaluated and establish interactions and mechanisms, since with this technique information is obtained directly from the structure at the level of pairs of atoms.

As mentioned, hydrogen spillover is one of the possible mechanisms in the type of materials studied for the WGSR. FTIR spectroscopy can be used to look for evidence

of hydrogen-deuterium exchange (H-D exchange) as proof that spillover is taking place.

Evaluating the catalytic performance of catalysts in the aquaprocessing of heavy oils at different reaction conditions (spatial velocity, reaction time, temperature), and in a pilot-scale system, would be beneficial for commercializing such a catalyst.

9.   BIBLIOGRAPHY

[1]   J. Speight, The Chemistry and Technology of Petroleum, Fourth Edition, 2006. https://doi.org/10.1201/9781420008388.

[2]   R. Martínez-Palou, M. de L. Mosqueira, B. Zapata-Rendón, E. Mar-Juárez, C. Bernal-Huicochea, J. de la Cruz Clavel-López, J. Aburto, Transportation of heavy and extra-heavy crude oil by pipeline: A review, J Pet Sci Eng. 75 (2011) 274–282. https://doi.org/10.1016/j.petrol.2010.11.020.

[3]   J.G. Speight, CHAPTER 8 – UPGRADING HEAVY OIL, in: Enhanced Recovery Methods for Heavy Oil and Tar Sands, 2009: pp. 261–294. https://doi.org/10.1016/B978-1-933762-25-8.50013-4.

[4]   M.M. Fathi, P. Pereira-Almao, Catalytic aquaprocessing of arab light vacuum residue via short space times, Energy and Fuels. 25 (2011) 4867–4877. https://doi.org/10.1021/ef200936k.

[5]   E.A. Garcia-Hubner, Catalytst Evaluation for Catalytic Steam Cracking of De-asphalted Oil in a Fixed Bed Reactor, University of Calgary, 2015.

[6]   W. Li, J. Zhu, J. Qi, Application of nano-nickel catalyst in the viscosity reduction of Liaohe extra-heavy oil by aqua-thermolysis, Journal of Fuel Chemistry and Technology. 35 (2007) 176–180. https://doi.org/10.1016/S1872-5813(07)60016-4.

[7]   M. Dejhosseini, T. Aida, M. Watanabe, S. Takami, D. Hojo, N. Aoki, T. Arita, A. Kishita, T. Adschiri, Catalytic cracking reaction of heavy oil in the presence of cerium oxide nanoparticles in supercritical water, Energy and Fuels. 27 (2013) 4624–4631. https://doi.org/10.1021/ef400855k.

[8]   V. Alvarado-González, Desarrollo de catalizadores para el hidroprocesamiento de aceites pesados y extrapesados, Instituto Potosino de Investigación Científica y Tecnológica, A.C., 2018.

[9]   D. Joung, V. Singh, S. Park, A. Schulte, S. Seal, S.I. Khondaker, J. Accepted, Anchoring Ceria Nanoparticles on Reduced Graphene Oxide and Their Electronic Transport Properties, J. Phys. Chem. C. 115 (2011) 24494–24500. https://doi.org/10.1021/jp206485v.

[10]   L. Barrio, A. Kubacka, G. Zhou, M. Estrella, A. Martínez-Arias, J.C. Hanson, M. Fernández-García, J.A. Rodríguez, Unusual Physical and Chemical Properties of Ni in Ce1-xNixO2-y Oxides: Structural Characterization and Catalytic Activity for the Water Gas Shift Reaction, J. Phys. Chem. C. 114 (2010) 12689–12697.

[11]   R.G. Santos, W. Loh, A.C. Bannwart, O. v. Trevisan, An overview of heavy oil properties and its recovery and transportation methods, Brazilian Journal of Chemical Engineering. 31 (2014) 571–590. https://doi.org/10.1590/0104-6632.20140313s00001853.

[12]   J.G. Speight, Heavy and Extra-heavy Oil Upgrading Technologies, 2013. https://doi.org/10.1016/B978-0-12-404570-5.00001-6.

[13]   A.-Y. Huc, Heavy Crude Oils: From Geology to Upgrading : an Overview, 2010. https://books.google.com/books?id=_gsri7-F9vkC&pgis=1.

[14]   Dwijen K. Banerjee, Oil Sands, & Bitumen Heavy Oil From Recovery To Refinery,   2012. http://app.knovel.com/web/toc.v/cid:kpOSHOBFRL/viewerType:toc/root_slug:oil-sands-heavy-oil-bitumen/url_slug:kt00BIDWF3?b-q=properties   of   bitumen&b-group-by=true&b-search-type=tech-reference&b-sort-on=default.

[15]   T. Sato, Upgrading of heavy oil by hydrogenation through partial oxidation and water-gas shift reaction in supercritical water, Journal of the Japan Petroleum Institute. 57 (2014) 1–10. https://doi.org/10.1627/jpi.57.1.

[16]   O.O. Mironenko, G.A. Sosnin, P.M. Eletskii, Y.K. Gulyaeva, O.A. Bulavchenko, O.A. Stonkus, V.O. Rodina, V.A. Yakovlev, A Study of the Catalytic Steam Cracking of Heavy Crude Oil in the Presence of a Dispersed Molybdenum-

Containing Catalyst, Petroleum Chemistry. 57 (2017) 618–629. https://doi.org/10.1134/S0965544117070088.

[17]   P.M. Eletskii, O.O. Mironenko, S.A. Selishcheva, V.A. Yakovlev, Investigating the Process of Heavy Crude Oil Steam Cracking over Disperse Catalysts. I: Selection of Optimal Steam Cracking Conditions without Catalyst, Catal Ind. 8 (2016) 217–223. https://doi.org/10.1134/S207005041603003X.

[18]   P. Pereira, R. Marzin, L. Zacarias, J. Córdova, J. Carrazza, M. Mariño, Steam conversion process and catalyst, U.S. Patent No. 5885441, 1999. https://patentimages.storage.googleapis.com/33/86/93/0ee2a1ae93a82c/US5885441.pdf.

[19]   F.T.T. Ng, S.K. Tsakiri, Activation of water in emulsion for catalytic desulphurization of benzothiophene, Fuel. 71 (1992) 1309–1314. https://doi.org/10.1016/0016-2361(92)90059-W.

[20]   K. Arai, T. Adschiri, M. Watanabe, Hydrogenation of Hydrocarbons through Partial Oxidation in Supercritical Water, (2000). https://doi.org/10.1021/ie000326g.

[21]   A.C. Pitchford, Upgrading of crude oils, U.S. Patent No. 3676331 A, 1972.

[22]   O. P. Avbenake, F. Ibrahim Yakasai, B. Y. Jibril, Sustainability Effect of Water Gas Shift Reaction (Syngas) in Catalytic Upgrading of Heavy Crude Oil and Bitumen, in: Sustainable Alternative Syngas Fuel [Working Title], IntechOpen, 2019. https://doi.org/10.5772/intechopen.86236.

[23]   A. Hart, G. Leeke, M. Greaves, J. Wood, Downhole Heavy Crude Oil Upgrading Using CAPRI: Effect of Steam upon Upgrading and Coke Formation, (2014). https://doi.org/10.1021/ef402300k.

[24]   D.B. Pal, R. Chand, S.N. Upadhyay, P.K. Mishra, Performance of water gas shift reaction catalysts: A review, Renewable and Sustainable Energy Reviews. 93 (2018) 549–565. https://doi.org/10.1016/j.rser.2018.05.003.

[25]   E. Toon Saw, U. Oemar, M. Li Ang, H. Kus, S. Kawi, High Temperature-Water Gas Shift on Ni-Cu/CeO 2 Catalysts: Effect of Ceria Nano-Crystal Size on Carboxylate Formation, J. Name. 00 (2013) 1–3. https://doi.org/10.1039/x0xx00000x.

[26]   A.B. Dongil, L. Pastor-Pérez, N. Escalona, A. Sepúlveda-Escribano, Carbon nanotube-supported Ni-CeO2 catalysts. Effect of the support on the catalytic performance in the low-temperature WGS reaction, Carbon N Y. 101 (2016) 296–304. https://doi.org/10.1016/j.carbon.2016.01.103.

[27]   J. Ashok, M.H. Wai, S. Kawi, Nickel-based Catalysts for High-temperature Water Gas Shift Reaction-Methane Suppression, ChemCatChem. 10 (2018) 3927–3942. https://doi.org/10.1002/cctc.201800031.

[28]   M. Zhou, T.N.-M. Le, L.K. Huynh, B. Liu, Effects of structure and size of Ni nanocatalysts on hydrogen selectivity via water-gas-shift reaction—A first-principles-based kinetic study, Catal Today. 280 (2017) 210–219. https://doi.org/10.1016/J.CATTOD.2016.07.018.

[29]   J.C. Idrobo, W. Zhou, A short story of imaging and spectroscopy of two-dimensional materials by scanning transmission electron microscopy, Ultramicroscopy. 180 (2017) 156–162. https://doi.org/10.1016/J.ULTRAMIC.2017.02.002.

[30]   D. Vovchok, C.J. Guild, J. Llorca, R.M. Palomino, I. Waluyo, J.A. Rodriguez, S.L. Suib, S.D. Senanayake, Structural and chemical state of doped and impregnated mesoporous Ni/CeO2 catalysts for the water-gas shift, Appl Catal A Gen. 567 (2018) 1–11. https://doi.org/10.1016/j.apcata.2018.08.026.

[31]   M.E. Khan, M.M. Khan, M.H. Cho, Ce3+-ion, Surface Oxygen Vacancy, and Visible Light-induced Photocatalytic Dye Degradation and Photocapacitive Performance of CeO2-Graphene Nanostructures, Sci Rep. 7 (2017) 1–17. https://doi.org/10.1038/s41598-017-06139-6.

[32]   E. Sartoretti, C. Novara, F. Giorgis, M. Piumetti, S. Bensaid, N. Russo, D. Fino, In situ Raman analyses of the soot oxidation reaction over nanostructured ceria-based catalysts, Sci Rep. 9 (2019). https://doi.org/10.1038/s41598-019-39105-5.

[33]   L.Z. Linganiso, V.R.R. Pendyala, G. Jacobs, B.H. Davis, D.C. Cronauer, A.J. Kropf, C.L. Marshall, Low-Temperature Water–Gas Shift: Doping Ceria Improves Reducibility and Mobility of O-Bound Species and Catalyst Activity, Catalysis Letters 2011 141:12. 141 (2011) 1723–1731. https://doi.org/10.1007/S10562-011-0720-1.

[34]   D. Andreeva, M. Kantcheva, I. Ivanov, L. Ilieva, J.W. Sobczak, W. Lisowski, Gold supported on ceria doped by Me3+ (Me = Al and Sm) for water gas shift reaction: Influence of dopant and preparation method, Catal Today. 158 (2010) 69–77. https://doi.org/10.1016/J.CATTOD.2010.05.030.

[35]   G. Jacobs, E. Chenu, P.M. Patterson, L. Williams, D. Sparks, G. Thomas, B.H. Davis, Water-gas shift: comparative screening of metal promoters for metal/ceria systems and role of the metal, Appl Catal A Gen. 258 (2004) 203–214. https://doi.org/10.1016/J.APCATA.2003.09.007.

[36]   S. Hilaire, X. Wang, T. Luo, R.J. Gorte, J. Wagner, A comparative study of water-gas-shift reaction over ceria supported metallic catalysts, Appl Catal A Gen. 215 (2001) 271–278. https://doi.org/10.1016/S0926-860X(01)00535-X.

[37]   A. Haryanto, S.D. Fernando, S.D. Filip, P.H. Steele, L. Pordesimo, S. Adhikari, Hydrogen Production through the Water-Gas Shift Reaction: Thermodynamic Equilibrium versus Experimental Results over Supported Ni Catalysts, Energy & Fuels. (2009) 3097–3102. https://doi.org/10.1021/ef801076r.

[38]   L. Pastor-Pérez, R. Buitrago-Sierra, A. Sepúlveda-Escribano, CeO2-promoted Ni/activated carbon catalysts for the water-gas shift (WGS) reaction, Int J Hydrogen Energy. 39 (2014) 17589–17599. https://doi.org/10.1016/j.ijhydene.2014.08.089.

[39]   S. Alamolhoda, G. Vitale, A. Hassan, N.N. Nassar, P. Pereira Almao, Development and characterization of novel combinations of Ce-Ni-MFI solids for water gas shift reaction, Canadian Journal of Chemical Engineering. 9999 (2018) 1– 12. https://doi.org/10.1002/cjce.23201.

[40]   E.F. Gallei, M. Hesse, E. Schwab, Development of Industrial Catalysts 1 A list of symbols used in the text is provided at the end of the chapter., Handbook of Heterogeneous   Catalysis.   (2008)   57–66. https://doi.org/10.1002/9783527610044.HETCAT0004.

[41]   P. Munnik, P.E. De Jongh, K.P. De Jong, Recent Developments in the Synthesis of Supported Catalysts, Chem Rev. 115 (2015) 6687–6718. https://doi.org/10.1021/cr500486u.

[42]   M. Campanati, G. Fornasari, A. Vaccari, Fundamentals in the preparation of heterogeneous   catalysts,   Catal   Today.   77   (2003)   299–314. https://doi.org/10.1016/S0920-5861(02)00375-9.

[43]   G. Busca, Structural, Surface, and Catalytic Properties of Aluminas, 1st ed., Elsevier Inc., 2014. https://doi.org/10.1016/B978-0-12-800127-1.00003-5.

[44]   C.H. Bartholomew, Mechanisms of catalyst deactivation, Appl Catal A Gen. 212 (2001) 17–60. https://doi.org/10.1016/S0926-860X(00)00843-7.

[45]   A. V. Nelmark, L.I. Kheifez, V.B. Fenelonov, Theory of Preparation of Supported Catalysts, Industrial and Engineering Chemistry Product Research and Development. 20 (1981) 439–450. https://doi.org/10.1021/i300003a006.

[46]   K. Kakaei, M.D. Esrafili, A. Ehsani, Introduction to Catalysis, in: Graphene Surfaces: Particles   and   Catalysts,   Elsevier,   2019:   pp.   1–21. https://doi.org/10.1016/B978-0-12-814523-4.00001-0.

[47]   D. Deng, K.S. Novoselov, Q. Fu, N. Zheng, Z. Tian, X. Bao, Catalysis with two-dimensional   materials   and   their   heterostructures,   11   (2016)   218–230. https://doi.org/10.1038/nnano.2015.340.

[48]   A. Bianco, H.M. Cheng, T. Enoki, Y. Gogotsi, R.H. Hurt, N. Koratkar, T. Kyotani, M. Monthioux, C.R. Park, J.M.D. Tascon, J. Zhang, All in the graphene family - A recommended nomenclature for two-dimensional carbon materials, Carbon N Y. 65 (2013) 1–6. https://doi.org/10.1016/j.carbon.2013.08.038.

[49]   H. Ren, E. Cunha, Q. Sun, Z. Li, I.A. Kinloch, R.J. Young, Z. Fan, Surface functionality analysis by Boehm titration of graphene nanoplatelets functionalized via a solvent-free cycloaddition reaction, Nanoscale Adv. 1 (2019) 1432–1441. https://doi.org/10.1039/C8NA00280K.

[50]   H. Dong, Y.C. Chen, C. Feldmann, Polyol synthesis of nanoparticles: status and options regarding metals, oxides, chalcogenides, and non-metal elements, Green Chemistry. 17 (2015) 4107–4132. https://doi.org/10.1039/c5gc00943j.

[51]   M. Valiskò, D. Boda, Relative permittivity of polar liquids, comparison of theory, experiment, and simulation, Journal of Physical Chemistry B. 109 (2005) 6355–6365. https://doi.org/10.1021/JP046960F/ASSET/IMAGES/LARGE/JP046960FF00008.JPEG.

[52]   Y. Wang, Y. Zheng, C.Z. Huang, Y. Xia, Synthesis of Ag nanocubes 18-32 nm in edge length: The effects of polyol on reduction kinetics, size control, and reproducibility, J Am Chem Soc. 135 (2013) 1941–1951. https://doi.org/10.1021/JA311503Q/SUPPL_FILE/JA311503Q_SI_001.PDF.

[53]   S. Komarneni, D. Li, B. Newalkar, H. Katsuki, A.S. Bhalla, Microwave−Polyol Process for Pt and Ag Nanoparticles, Langmuir. 18 (2002) 5959–5962. https://doi.org/10.1021/LA025741N.

[54]   K. Fujimoto, Catalyst design based on spillover theory, Stud Surf Sci Catal. 77 (1993) 9–16. https://doi.org/10.1016/S0167-2991(08)63150-X.

[55]   A. Hassan, K. Fujimoto, K. Tomishige, T. Kusakari, A. Akasaka, In-situ FTIR study of hydrogen spillover and reaction kinetics in hybrid catalysts, in: Stud Surf Sci

Catal, Elsevier Inc., 2001: pp. 39–46. https://doi.org/10.1016/s0167-2991(01)80011-2.

[56] W.C. Conner, J.L. Falconer, Spillover in Heterogeneous Catalysis, Chem Rev. 95 (1995) 759–788. https://doi.org/10.1021/cr00035a014.

[57] J.M. Herrmann, E. Ramaroson, J.F. Tempere, M.F. Guilleux, Semiconductivity study of ceria-supported nickel related to its methanation catalytic activity, Appl Catal. 53 (1989) 117–134. https://doi.org/10.1016/S0166-9834(00)80016-0.

[58] R. Prins, Hydrogenation by spillover of hydrogen from metal to acidic support or by reverse spillover of the reactant molecule from the support to the metal, Stud Surf Sci Catal. 138 (2001) 1–2. https://doi.org/10.1016/S0167-2991(01)80007-0.

[59] D. Scarano, S. Bordiga, C. Lamberti, G. Ricchiardi, S. Bertarione, G. Spoto, Hydrogen adsorption and spill-over effects on H-Y and Pd-containing Y zeolites. An experimental and theoretical investigation, Appl Catal A Gen. 307 (2006) 3–12. https://doi.org/10.1016/j.apcata.2006.03.015.

[60] R. Prins, Hydrogen Spillover. Facts and Fiction, (2012). https://doi.org/10.1021/cr200346z.

[61] S.M. Schimming, G.S. Foo, O.D. Lamont, A.K. Rogers, M.M. Yung, A.D. D'amico, C. Sievers, Kinetics of hydrogen activation on ceria-zirconia, (2015). https://doi.org/10.1016/j.jcat.2015.05.027.

[62] J.H. Lehman, M. Terrones, E. Mansfield, K.E. Hurst, V. Meunier, Evaluating the characteristics of multiwall carbon nanotubes, Carbon N Y. 49 (2011) 2581–2602. https://doi.org/10.1016/j.carbon.2011.03.028.

[63] S. Osswald, M. Havel, Y. Gogotsi, Monitoring oxidation of multiwalled carbon nanotubes by Raman spectroscopy, Journal of Raman Spectroscopy. 38 (2007) 728–736. https://doi.org/10.1002/jrs.1686.

[64]   G. Rajender, P.K. Giri, Formation mechanism of graphene quantum dots and their edge state conversion probed by photoluminescence and Raman spectroscopy, J Mater Chem C Mater. 4 (2016) 10852–10865. https://doi.org/10.1039/c6tc03469a.

[65]   R. Sharma, N. Chadha, P. Saini, Determination of defect density , crystallite size and number of graphene layers in graphene analogues using X-ray diffraction and Raman spectroscopy, 55 (2017) 625–629.

[66]   A. Bellunato, H.A. Tash, Y. Cesa, G.F. Schneider, Chemistry at the edge of graphene,   n.d. https://openaccess.leidenuniv.nl/bitstream/handle/1887/48274/Openaccess_Chem PhysChem_Chemistryattheedgesofgraphene.pdf?sequence=1 (accessed May 15, 2019).

[67]   S. Soren, M. Bessoi, P. Parhi, A rapid microwave initiated polyol synthesis of cerium oxide nanoparticle using different cerium precursors, Ceram Int. 41 (2015) 8114–8118. https://doi.org/10.1016/j.ceramint.2015.03.013.

[68]   P.A. Jan Schönherr, Johannes R. Buchheim, Peter Scholz, Boehm Titration Revisited (Part I): Practical Aspects for Achieving a High Precision in Quantifying Oxygen-Containing Surface Groups on Carbon Materials, Journal of Carbon Research. 4 (2018) 21. https://doi.org/10.3390/c4020021.

[69]   W. Zhou, • Zhong, L. Wang, Fundamentals of Scanning Electron Microscopy (SEM), 2006. https://doi.org/10.1007/978-0-387-39620-0_1.

[70]   S. Grewal, A. Macedo Andrade, Z. Liu, J.A. Garrido Torres, A.J. Nelson, A. Kulkarni, M. Bajdich, M.H. Lee, Highly Active Bifunctional Oxygen Electrocatalytic Sites Realized in Ceria–Functionalized Graphene, Adv Sustain Syst. 4 (2020). https://doi.org/10.1002/ADSU.202000048.

[71]   F. Jollet, T. Petit, S. Gota, N. Thromat, M. Gautier-Soyer, A. Pasturel, The electronic structure of uranium dioxide: an oxygen K-edge x-ray absorption study,

Journal of Physics: Condensed Matter. 9 (1997) 9393. https://doi.org/10.1088/0953-8984/9/43/022.

[72]   S. Ostanin, A.J. Craven, D.W. McComb, D. Vlachos, A. Alavi, M.W. Finnis, A.T. Paxton, Effect of relaxation on the oxygen K-edge electron energy-loss near-edge structure in yttria-stabilized zirconia, Phys Rev B Condens Matter Mater Phys. 62 (2000) 14728–14735. https://doi.org/10.1103/PHYSREVB.62.14728.

[73]   G. Strasser, F.P. Netzer, Core electron energy loss spectroscopy of cerium: Surface oxidation, Journal of Vacuum Science & Technology A: Vacuum, Surfaces, and Films. 2 (1984) 826–830. https://doi.org/10.1116/1.572516.

[74]   H. Xu, Y. Wang, Electron energy-loss spectroscopy (EELS) study of oxidation states of Ce and U in pyrochlore and uraninite - Natural analogues for Pu- and U-bearing waste forms, Journal of Nuclear Materials. 265 (1999) 117–123. https://doi.org/10.1016/S0022-3115(98)00566-2.

[75]   H. Dexpert, R.C. Karnatak, J.M. Esteva, C. J. P., M. Gasgnier, P.E. Caro, L. Albert, X-ray absorption studies of CeO2, PrO2, TbO2, Phys Rev B. 36 (1987) 1750.

[76]   K. Song, H. Schmid, V. Srot, Cerium reduction at the interface between ceria and yttria-stabilised zirconia and implications for interfacial oxygen non-stoichiometry, 2 (2014) 32104. https://doi.org/10.1063/1.4867556.

[77]   S. Turner, S. Lazar, B. Freitag, R. Egoavil, J. Verbeeck, S. Put, Y. Strauven, G. van Tendeloo, High resolution mapping of surface reduction in ceria nanoparticles, Nanoscale. 3 (2011) 3385–3390. https://doi.org/10.1039/c1nr10510h.

[78]   S.Y. Chen, R.J. Chen, W. Lee, C.L. Dong, A. Gloter, Spectromicroscopic evidence of interstitial and substitutional dopants in association with oxygen vacancies in Sm-doped ceria nanoparticles, Physical Chemistry Chemical Physics. 16 (2014) 3274–3281. https://doi.org/10.1039/c3cp54613f.

[79] G. Niu, M.A. Schubert, F. D'Acapito, M.H. Zoellner, T. Schroeder, F. Boscherini, On the local electronic and atomic structure of Ce1-xPrxO2-δ epitaxial films on Si, J Appl Phys. 116 (2014). https://doi.org/10.1063/1.4896590.

[80] W. Zhou, S.J. Pennycook, J.C. Idrobo, Probing the electronic structure and optical response of a graphene quantum disk supported on monolayer graphene, Journal of Physics Condensed Matter. 24 (2012). https://doi.org/10.1088/0953-8984/24/31/314213.

[81] K.A. Mkhoyan, A.W. Contryman, J. Silcox, D.A. Stewart, G. Eda, C. Mattevi, S. Miller, M. Chhowalla, Atomic and electronic structure of graphene-oxide, Nano Lett. 9 (2009) 1058–1063. https://doi.org/10.1021/NL8034256.

[82] L.A.J. Garvie, A.J. Craven, R. Brydson, Use of electron-energy loss near-edge fine structure in the study of minerals, American Mineralogist. 79 (1994) 411–425.

[83] Z. Xu, Y. Bando, L. Liu, W. Wang, X. Bai, D. Golberg, Electrical conductivity, chemistry, and bonding alternations under graphene oxide to graphene transition as revealed by in situ TEM, ACS Nano. 5 (2011) 4401–4406. https://doi.org/10.1021/NN103200T.

[84] Z. Xu, Y. Bando, L. Liu, W. Wang, X. Bai, D. Golberg, Electrical Conductivity, Chemistry, and Bonding Alternations under Graphene Oxide to Graphene Transition As Revealed by In Situ TEM, ACS Nano. 5 (2011) 4401–4406. www.acsnano.org (accessed November 3, 2021).

[85] S. Komarneni, R. Pidugu, Q.H. Li, R. Roy, Microwave-hydrothermal processing of metal powders, J Mater Res. 10 (1995) 1687–1692. https://doi.org/10.1557/JMR.1995.1687.

[86] R. Cavendish, Structural Analysis of Nickel Doped Cerium Oxide Catalysts for Fuel Reforming in Solid Oxide Fuel Cells, 2012.

[87]   J. Xu, B. Xue, Y.-M. Liu, Y.-X. Li, Y. Cao, K.-N. Fan, Mesostructured Ni-doped ceria as an efficient catalyst for styrene synthesis by oxidative dehydrogenation of ethylbenzene, Appl Catal A Gen. 405 (2011) 142–148. https://doi.org/10.1016/j.apcata.2011.08.001.

[88]   R.O. Fuentes, L.M. Acuña, C.A. Albornoz, A.G. Leyva, N. Sousa, F.M. Figueiredo, Structural, physical and chemical properties of nanostructured nickel-substituted ceria oxides under reducing and oxidizing conditions, RSC Adv. 6 (2016) 64861–64870. https://doi.org/10.1039/c6ra14853k.

[89]   J.R. McBride, C.K. Hass, B.D. Poindexter, W.H. Weber, Raman and xray studies of Ce1 − xRExO2 − y, where RE = La , Pr , Nd , Eu , Gd , and Tb, J Appl Phys. 76 (1994) 2435–2441.

[90]   L. Katta, P. Sudarsanam, B. Mallesham, B.M. Reddy, Preparation of silica supported ceria–lanthana solid solutions useful for synthesis of 4-methylpent-1-ene and dehydroacetic acid, Catal Sci Technol. 2 (2012) 995–1004. https://doi.org/10.1039/c2cy00551d.

[91]   T. Taniguchi, T. Watanabe, N. Sugiyama, A.K. Subramani, H. Wagata, N. Matsushita, M. Yoshimura, Identifying Defects in Ceria-Based Nanocrystals by UV Resonance Raman Spectroscopy, (n.d.). https://doi.org/10.1021/jp9049457.

[92]   M. Xu, J.P. Larentzos, M. Roshdy, L.J. Criscenti, H.C. Allen, Aqueous divalent metal-nitrate interactions: Hydration versus ion pairing, Physical Chemistry Chemical Physics. 10 (2008) 4793–4801. https://doi.org/10.1039/b807090n.

[93]   W. Brockner, C. Ehrhardt, M. Gjikaj, Thermal decomposition of nickel nitrate hexahydrate, Ni(NO3)2·6H2O, in comparison to Co(NO3)2·6H2O and Ca(NO3)2·4H2O, Thermochim Acta. 456 (2007) 64–68. https://doi.org/10.1016/J.TCA.2007.01.031.

[94]   S. Fu, Q. Fang, A. Li, Z. Li, J. Han, X. Dang, W. Han, Accurate characterization of full pore size distribution of tight sandstones by low-temperature

nitrogen gas adsorption and high-pressure mercury intrusion combination method, Energy Sci Eng. 9 (2021) 80–100. https://doi.org/10.1002/ese3.817.

[95]   W. Liu, W. Wang, K. Tang, J. Guo, Y. Ren, S. Wang, L. Feng, Y. Yang, The promoting influence of nickel species in the controllable synthesis and catalytic properties of nickel-ceria catalysts, Catal Sci Technol. 6 (2016) 2427–2434. https://doi.org/10.1039/c5cy01241d.

[96]   Y. Xu, F. Wang, X. Liu, Y. Liu, M. Luo, B. Teng, M. Fan, X. Liu, Resolving a Decade-Long Question of Oxygen Defects in Raman Spectra of Ceria-Based Catalysts at Atomic Level, (n.d.). https://doi.org/10.1021/acs.jpcc.9b00633.

[97]   A.R. Puigdollers, P. Schlexer, S. Tosoni, G. Pacchioni, Increasing oxide reducibility: The role of metal/oxide interfaces in the formation of oxygen vacancies, ACS Catal. 7 (2017) 6493–6513. https://doi.org/10.1021/acscatal.7b01913.

[98]   E.I. Bîru, H. Iovu, Graphene Nanocomposites Studied by Raman Spectroscopy, InTech, 2018. https://doi.org/10.5772/intechopen.73487.

[99]   I. Childres, L.A. Jauregui, W. Park, H. Cao, Y.P. Chen, Raman Spectroscopy of Graphene and Related Materials, 2013.

[100]   J. Liu, Q. Li, Y. Zou, Q. Qian, Y. Jin, G. Li, K. Jiang, S. Fan, The dependence of graphene Raman D-band on carrier density, Nano Lett. 13 (2013) 6170–6175. https://doi.org/10.1021/nl4035048.

[101]   A. V Neimark, K.S.W. Sing, M. Thommes, Surface Area and Porosity, in: Handbook of Heterogeneous Catalysis, Wiley-VCH Verlag GmbH & Co. KGaA, 2008. https://doi.org/10.1002/9783527610044.hetcat0037.

[102]   W.Y. Hernández, O.H. Laguna, M.A. Centeno, J.A. Odriozola, Structural and catalytic properties of lanthanide (La, Eu, Gd) doped ceria, J Solid State Chem. 184 (2011) 3014–3020. https://doi.org/10.1016/j.jssc.2011.09.018.

[103] L. Evans Analytical Group, Inductively Coupled Plasma Spectroscopy, Printed in USA • 08/07 BR023. (2007).

[104] B. Ravel, M. Newville, ATHENA, ARTEMIS, HEPHAESTUS: data analysis for X-ray absorption spectroscopy using IFEFFIT, J Synchrotron Radiat. 12 (2005) 537–541. https://doi.org/10.1107/S0909049505012719.

[105] P. Nachimuthu, W.C. Shih, R.S. Liu, L.Y. Jang, J.M. Chen, The study of nanocrystalline cerium oxide by X-ray absorption spectroscopy, J Solid State Chem. 149 (2000) 408–413. https://doi.org/10.1006/JSSC.1999.8566.

[106] T.S. Wu, Y. Zhou, R.F. Sabirianov, W.N. Mei, Y.L. Soo, C.L. Cheung, X-ray absorption study of ceria nanorods promoting the disproportionation of hydrogen peroxide, Chemical Communications. 52 (2016) 5003–5006. https://doi.org/10.1039/c5cc10643e.

[107] W. Lee, S.Y. Chen, Y.S. Chen, C.L. Dong, H.J. Lin, C. Te Chen, A. Gloter, Defect Structure Guided Room Temperature Ferromagnetism of Y-Doped CeO2 Nanoparticles, Journal of Physical Chemistry C. 118 (2014) 26359–26367. https://doi.org/10.1021/jp507694d.

[108] E.E. Alp, S.M. Mini, M. Ramanathan, EXAFS and XANES - A Versatile Tool to Study the Atomic and Electronic Structure of Materials, X-Ray Absorption Spectroscopy. (1990) 25–36.

[109] K. Liu, S. Tan, J. Moon, C.J. Jafta, C. Li, T. Kobayashi, H. Lyu, C.A. Bridges, S. Men, W. Guo, Y. Sun, J. Zhang, M.P. Paranthaman, X.G. Sun, S. Dai, Insights into the Enhanced Cycle and Rate Performances of the F-Substituted P2-Type Oxide Cathodes for Sodium-Ion Batteries, Adv Energy Mater. 10 (2020) 1–11. https://doi.org/10.1002/aenm.202000135.

[110] U. Boesenberg, M.A. Marcus, A.K. Shukla, T. Yi, E. McDermott, P.F. Teh, M. Srinivasan, A. Moewes, J. Cabana, Asymmetric pathways in the electrochemical

conversion reaction of NiO as battery electrode with high storage capacity, Sci Rep. 4 (2014) 1–9. https://doi.org/10.1038/srep07133.

[111] L. Pastor-Pérez, R. Buitrago-Sierra, A. Sepúlveda-Escribano, CeO2-promoted Ni/activated carbon catalysts for the water-gas shift (WGS) reaction, Int J Hydrogen Energy. 39 (2014) 17589–17599. https://doi.org/10.1016/j.ijhydene.2014.08.089.

[112] M.L. Ang, U. Oemar, E.T. Saw, L. Mo, Y. Kathiraser, B.H. Chia, S. Kawi, Highly Active Ni/xNa/CeO 2 Catalyst for the Water−Gas Shift Reaction: Effect of Sodium on Methane Suppression, (2014). https://doi.org/10.1021/cs500915p.

[113] E.T. Saw, U. Oemar, X.R. Tan, Y. Du, A. Borgna, K. Hidajat, S. Kawi, Bimetallic Ni–Cu catalyst supported on CeO2 for high-temperature water–gas shift reaction: Methane suppression via enhanced CO adsorption, J Catal. 314 (2014) 32–46. https://doi.org/10.1016/J.JCAT.2014.03.015.

[114] M. Xu, S. He, H. Chen, G. Cui, L. Zheng, B. Wang, M. Wei, TiO 2−x-Modified Ni Nanocatalyst with Tunable Metal−Support Interaction for Water−Gas Shift Reaction, ACS Catal. 7 (2017) 7600–7609. https://doi.org/10.1021/acscatal.7b01951.

ANNEX I: SCIENTIFIC PUBLICATION

Alvarado-Gonzalez, V., Escobar-Barrios, V. A., Pereira-Almao, P., Vitale-Rojas, G., & Hassan, A. (2022). Thermal-structural characterization and H2 generation capability of novel CeO2/graphene catalyst. Journal of Environmental Chemical Engineering, 10(3), 107680.

Thermal-structural characterization and H_2 generation capability of novel CeO_2/graphene catalyst

Valeria Alvarado-González [a], Vladimir Alonso Escobar-Barrios [a,*], Pedro Pereira-Almao [b], Gerardo Vitale-Rojas [b], Azfar Hassan [b]

[a] División de Materiales Avanzados, Instituto Potosino de Investigación Científica y Tecnológica A.C., San Luis Potosí, San Luis Potosí 78216, Mexico
[b] Department of Chemical and Petroleum Engineering, University of Calgary, Calgary, Alberta T2N 1N4, Canada

ARTICLE INFO

ABSTRACT

This work focuses on the obtaining and studying a graphene-supported ceria catalyst by a simple, economic and reproducible method. The catalyst is intended for H_2 generation from water dissociation via water gas shift reaction (WGSR). Different characterization techniques were used to obtain the thermal-structural and elemental information of the catalysts synthesized by a microwave-initiated polyol method. The as-prepared catalyst (graphene-supported) exhibits excellent thermal resistance and lower temperature activation than a conventional catalyst supported on alumina. The catalytic performance of the material was evaluated by running the WGSR, in which the conversion of CO was twice in comparison with that obtained using the ceria supported in an alumina support and the methane selectivity was reduced, from 31% to 16.1% for alumina-supported and graphene-supported, respectively. Besides, the graphene-supported CeO_2/graphene catalyst exhibits higher selectivity towards H_2 generation than alumina-supported (43.1% vs 40.6%), as a consequence of synergism between ceria and graphene, which was evaluated using EELS technique, improving the catalytic activity of the material by the spillover effect. Finally, we suggest the use of this novel composite as support for metallic nanoparticles.

ANNEX II: N₂ ADSORPTION ISOTHERMS FITTING